



---

# **Prairie Island Nuclear Power Plant**

## **Qualification of Reactor Physics Methods for Application to Prairie Island**

**NSPNAD-8101  
Revision 2**

---

**December 1999**

**Northern States Power Company  
Nuclear Analysis & Design**

# PRAIRIE ISLAND NUCLEAR GENERATING PLANT

## QUALIFICATION OF REACTOR PHYSICS METHODS

FOR

### APPLICATION TO PRAIRIE ISLAND

NSPNAD-8101

Revision 2

December 1999

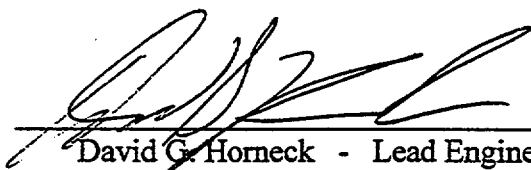
#### Principal Contributors

##### Revision 1


Clifford A. Bonneau  
William J. Lax  
Richard L. Streng

##### Revision 2

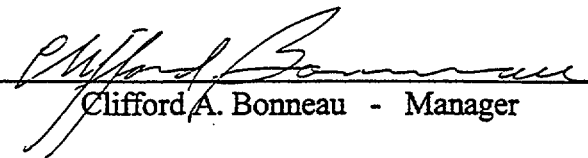
Jody I. Helland  
David G. Horneck  
William J. Lax  
Steve P. McSorely  
David J. Pribyl  
Ralph J. Rye  
Doug W. Shilts

Prepared by:   
David G. Horneck - Lead Engineer

Date: 12/16/99

Reviewed by:   
William J. Lax - Lead Engineer

Date: 12/16/99

Approved by:   
Clifford A. Bonneau - Manager

Date: 12/16/99

## ABSTRACT

This document is a Topical Report describing the Northern States Power Company (NSP) qualification of reactor physics methods for application to the Prairie Island Nuclear Generating Plant.

This document addresses the reactor model description, the qualification and quantification of reliability factors, and applications to operations and reload safety evaluations for the Prairie Island Nuclear Generating Plant.

## LEGAL NOTICE

This report was prepared by or on behalf of Northern States Power Company (NSP). It is intended for use by NSP personnel only. Use of any information, apparatus, method or process disclosed or contained in this report by non-authorized personnel shall be considered unauthorized use, unless said personnel have received prior, written permission from NSP to use the contents of this report. With respect to unauthorized use, neither NSP, nor any person acting on behalf of NSP:

- a. Makes any warranty or representation, express or implied, with respect to the accuracy, completeness, usefulness, or use of any information, apparatus, method or process disclosed or contained in this report, or that the use of any such information, apparatus, method, or process may not infringe privately owned rights; or
- b. Assumes any liabilities with respect to the use of, or for damages resulting from the use of, any information, apparatus, method, or process disclosed in the report.

## TABLE OF CONTENTS

	<u>PAGE</u>
1.0 INTRODUCTION	11
2.0 GENERAL CHARACTERISTICS OF THE NSP CALCULATIONAL MODELS	12
3.0 MODEL VERIFICATION & RELIABILITY FACTOR DETERMINATION	14
3.1 Rod Worth and Boron Worth Benchmarking	16
3.2 Temperature Coefficient Benchmarking	19
3.3 Doppler Coefficient	21
3.4 Isotopics	25
3.5 Power Distribution Reliability Factor Determination	26
3.5.1 Local Power Distribution - Reliability Factor on $F_Q^N$	27
3.5.2 Integrated Power Distribution - Reliability Factor on $F_{\Delta H}$	30
3.6 Model Application to Plant Transient Operation	80
3.7 Reliability Factors for Delayed Neutron Parameters	85
3.8 Effective Neutron Lifetime	87
4.0 MODEL APPLICATIONS TO REACTOR OPERATIONS	88
4.1 Power Distributions	88
4.2 Isotopic Inventory	88
4.3 Rod Swap Methodology	88
4.4 Transient Power Distribution Methodology	89
5.0 MODEL APPLICATIONS TO SAFETY EVALUATION CALCULATIONS	92
5.1 Nuclear Heat Flux Hot Channel Factor, $F_Q^N$	92
5.2 Nuclear Enthalpy Rise Hot Channel Factor, $F_{\Delta H}$	92
5.3 Rod Worths	93
5.4 Moderator Coefficient, $\alpha_m$	93
5.5 Fuel Temperature (Doppler) Coefficient, $\alpha_D$	93
5.6 Boron Concentration Coefficient, $\alpha_B$	94
5.7 Effective Delayed Neutron Fraction, $\beta_{eff}$	94
5.8 Prompt Neutron Generation Time, $\ell^*$	94
5.9 Shutdown Margin, SDM	94
5.10 Scram Worth Versus Time	95

TABLE OF CONTENTS (continued)

	<u>PAGE</u>
6.0 REFERENCES	97
APPENDIX A Statistical Methods for the Determination and Application of Uncertainties	99
A.1 Normal Distribution Statistics	100
A.2 Non-Normal Distribution Statistics	103
APPENDIX B Computer Code Summary Description	110

## LIST OF TABLES

	<u>PAGE</u>
3.0.1 Reliability Factors for Prairie Island	15
3.1.1 Measured versus Calculated Boron Endpoints	17
3.1.2 Measured versus Calculated Rod Bank Worths from Boron Endpoints	18
3.2.1 Measured versus Calculated Isothermal Temperature Coefficients	20
3.3.1 Measured versus Calculated Power Defect Comparisons	24
3.5.1 Full Power Statepoints	33
4.3.1 Measured versus Calculated Control Rod Bank Worths	90
A.1 Single-Sided Tolerance Factors	102

## LIST OF FIGURES

	<u>PAGE</u>	
2.0.1	Flowchart, PWR Methods, CASMO-4/SIMULATE-3 Model	13
3.3.1	Pincell Doppler Coefficients, MCNP-4A vs. CASMO-4	23
3.5.1	Measured versus Calculated Integrated Detector Response HFP, BOC, Cycle P217	36
3.5.2	Measured versus Calculated Detector Response HFP, BOC, Cycle P217, Thimble G-4	37
3.5.3	Measured versus Calculated Detector Response HFP, BOC, Cycle P217, Thimble C-9	38
3.5.4	Measured versus Calculated Integrated Detector Response HFP, MOC, Cycle P217	39
3.5.5	Measured versus Calculated Detector Response HFP, MOC, Cycle P217, Thimble G-4	40
3.5.6	Measured versus Calculated Detector Response HFP, MOC, Cycle P217, Thimble C-9	41
3.5.7	Measured versus Calculated Integrated Detector Response HFP, EOC, Cycle P217	42
3.5.8	Measured versus Calculated Detector Response HFP, EOC, Cycle P217, Thimble G-4	43
3.5.9	Measured versus Calculated Detector Response HFP, EOC, Cycle P217, Thimble C-9	44
3.5.10	Measured versus Calculated Integrated Detector Response HFP, BOC, Cycle P118	45
3.5.11	Measured versus Calculated Detector Response HFP, BOC, Cycle P118, Thimble G-2	46
3.5.12	Measured versus Calculated Detector Response HFP, BOC, Cycle P118, Thimble H-8	47



3.5.13	Measured versus Calculated Integrated Detector Response HFP, MOC, Cycle P118	48
3.5.14	Measured versus Calculated Detector Response HFP, MOC, Cycle P118, Thimble G-2	49
3.5.15	Measured versus Calculated Detector Response HFP, MOC, Cycle P118, Thimble H-8	50
3.5.16	Measured versus Calculated Integrated Detector Response HFP, EOC, Cycle P118	51
3.5.17	Measured versus Calculated Detector Response HFP, EOC, Cycle P118, Thimble G-2	52
3.5.18	Measured versus Calculated Detector Response HFP, EOC, Cycle P118, Thimble H-8	53
3.5.19	Measured versus Calculated Integrated Detector Response HFP, BOC, Cycle P218	54
3.5.20	Measured versus Calculated Detector Response HFP, BOC, Cycle P218, Thimble J-3	55
3.5.21	Measured versus Calculated Detector Response HFP, BOC, Cycle P218, Thimble H-10	56
3.5.22	Measured versus Calculated Integrated Detector Response HFP, MOC, Cycle P218	57
3.5.23	Measured versus Calculated Detector Response HFP, MOC, Cycle P218, Thimble J-3	58
3.5.24	Measured versus Calculated Detector Response HFP, MOC, Cycle P218, Thimble H-10	59
3.5.25	Measured versus Calculated Integrated Detector Response HFP, EOC, Cycle P218	60
3.5.26	Measured versus Calculated Detector Response HFP, EOC, Cycle P218, Thimble J-3	61
3.5.27	Measured versus Calculated Detector Response HFP, EOC, Cycle P218, Thimble H-10	62

3.5.28	Measured versus Calculated Integrated Detector Response HFP, BOC, Cycle P119	63
3.5.29	Measured versus Calculated Detector Response HFP, BOC, Cycle P119, Thimble E-2	64
3.5.30	Measured versus Calculated Detector Response HFP, BOC, Cycle P119, Thimble F-8	65
3.5.31	Measured versus Calculated Integrated Detector Response HFP, MOC, Cycle P119	66
3.5.32	Measured versus Calculated Detector Response HFP, MOC, Cycle P119, Thimble E-2	67
3.5.33	Measured versus Calculated Detector Response HFP, MOC, Cycle P119, Thimble F-8	68
3.5.34	Measured versus Calculated Integrated Detector Response HFP, EOC, Cycle P119	69
3.5.35	Measured versus Calculated Detector Response HFP, EOC, Cycle P119, Thimble E-2	70
3.5.36	Measured versus Calculated Detector Response HFP, EOC, Cycle P119, Thimble F-8	71
3.5.37	$F_Q$ Reliability Factor + Bias vs. Measured Reaction Rate	72
3.5.38	$F_Q$ Observed Differences Density Function	73
3.5.39	$F_Q$ Cumulative Distribution Function	74
3.5.40	Cumulative Distribution Function for $F_Q$ in the Region of the 95 <sup>th</sup> Percentile	75
3.5.41	$F_{\Delta H}$ Reliability Factor + Bias vs. Measured Reaction Rate	76
3.5.42	$F_{\Delta H}$ Observed Differences Density Function	77
3.5.43	$F_{\Delta H}$ Cumulative Distribution Function	78
3.5.44	Cumulative Distribution Function for $F_{\Delta H}$ in the Region of the 95 <sup>th</sup> Percentile	79
3.6.1	Prairie Island Unit 2 Cycle 17 Xenon Transient, Power and Boron vs. Date	81

3.6.2	Measured versus Calculated Integrated Detector Response 55% Power, D Bank at 184 Steps, Transient Xenon, Cycle P217	82
3.6.3	Measured versus Calculated Detector Response 55% Power, D Bank at 184 Steps, Transient Xenon, Cycle P217, Thimble G-4	83
3.6.4	Measured versus Calculated Detector Response 55% Power, D Bank at 184 Steps, Transient Xenon, Cycle P217, Thimble G-11	84
A.2.1	Differences for Nearby Positions	104

## 1.0 INTRODUCTION

This report addresses the reactor model description, qualification and quantification of reliability factors, and applications to operations and reload safety evaluations of the Prairie Island Nuclear Generating Plant (PI). This model, based on the Studsvik CMS system of codes, can be used as a substitute for the CASMO/PDQ/DP5 methods previously approved for use (reference 1). Approval of the methods described herein does not preclude the use of the previously approved CASMO/PDQ/DP5 methods.

A summary of the computer codes as they relate to implementation of the NSP model is given in Section 2. This report stresses the aspects of the implementation of the NSP model, not the development of the individual codes. Individual code documentation is referenced in Section 6. A brief summary description of each code is given in Appendix B.

Whenever possible, directly observable parameters, such as boron concentration and incore detector fission rates, are utilized. The Prairie Island data used in this evaluation spans Prairie Island Unit 1 cycles 17, 18 and 19, and Prairie Island Unit 2 cycles 16, 17 and 18. In order to be completely objective in the choice of data to be used for the comparisons, all PI measurements were reviewed and qualified prior to initiating the comparison calculations.

After the measured data to be used in the benchmark process had been defined, the model calculations were performed. Comparisons are presented in this report as part of the quantification of the NSP model calculational uncertainties and reliability factors. A statistical approach was used to derive the uncertainties. These uncertainties are consistent with the model application procedures and methodology.

The uncertainties are evaluated by direct comparison to experimental data.

In order to provide continuous verification of the conservatism of the reliability factors established within this report, comparisons are made each cycle using the statistical methods described in this report. A discussion of the reliability factors is provided in Section 3. The statistical approach is described in Appendix A.

The methods for use of the NSP model and the reliability factors relative to reactor operation and reload safety evaluations are described in Sections 4 and 5.

## 2.0 GENERAL CHARACTERISTICS OF THE NSP CALCULATIONAL MODELS

The Prairie Island (PI) calculational model, based on the Studsvik system of codes, is similar in many respects to the model previously approved for use for Prairie Island (see reference 1). A flow diagram of the Prairie Island model is shown in Figure 2.0.1. The code acronyms used in this figure are defined in Appendix B.

In general, the CASMO-4<sup>7,8</sup> program is used to generate the lattice physics parameters for input to SIMULATE-3<sup>9,10</sup>.

CASMO-4 produces fission product nuclide concentrations, depletion and fission product chain data, pin power distributions, microscopic and macroscopic cross sections, and other nuclear data that is input to TABLES-3<sup>11</sup>. CASMO-4 models gadolinia (Gd) containing fuel pins explicitly in its heterogeneous model.

TABLES-3 constructs tables of the nuclear data as functions of local state variables (e.g. water density, fuel temperature, etc.) for input to SIMULATE-3.

SIMULATE-3 is a three-dimensional, two-group steady state reactor neutronic and thermal hydraulic simulator. This simulator is used to generate eigenvalues, power distributions, and incore instrument predictions for use in reload safety evaluations, plant support calculations, reload design, fuel management, and benchmark comparisons.

ESCORE<sup>12,13,14,15</sup> is an EPRI computer code for steady state fuel performance analysis. The Prairie Island methodology uses ESCORE for fuel temperature predictions to be used as input to CASMO-4 and SIMULATE-3 for modeling fuel temperature related effects on the nuclear data (i.e. Doppler coefficient and power defect).

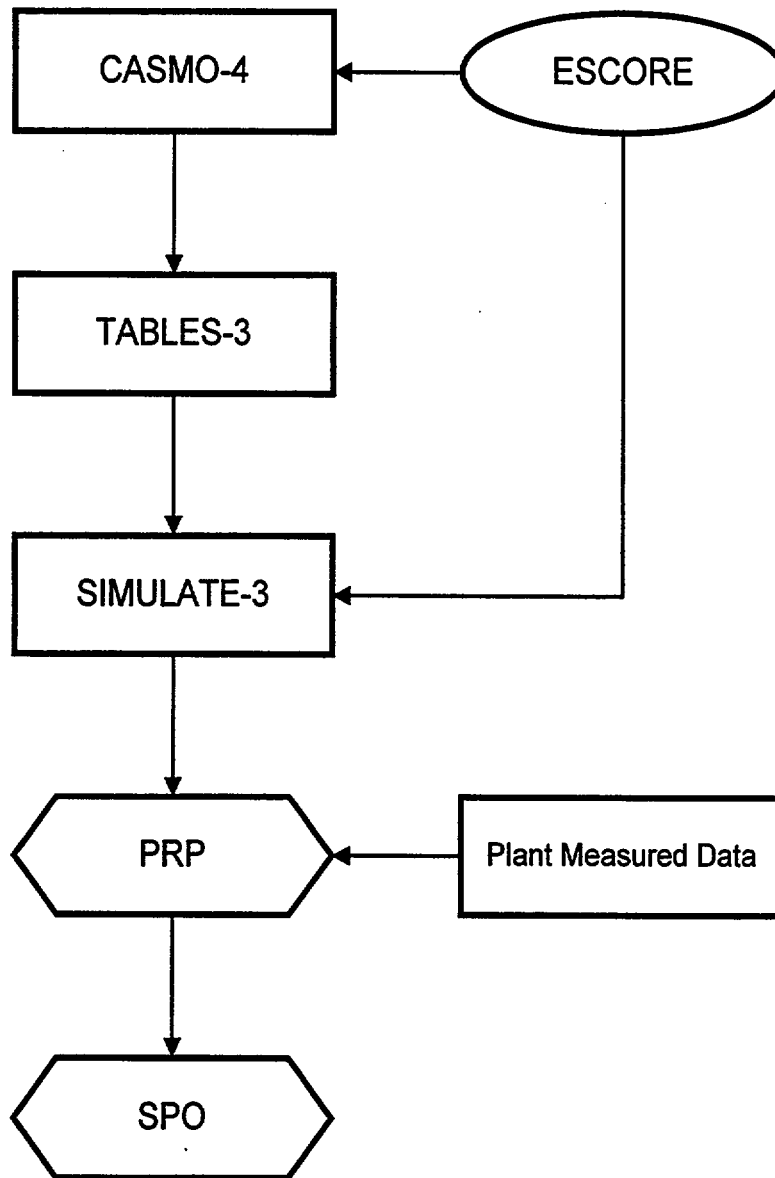
The PRP program, an NSP developed code, summarizes SIMULATE-3 predicted incore reaction rates and compares them to measured reaction rates.

SPO, an NSP developed code, then combines reaction rate comparisons for all the statepoints to calculate overall uncertainties.

The computer code descriptions are summarized in Appendix B.

FIGURE 2.0.1

PWR METHODS  
CASMO-4/SIMULATE-3 MODEL



### 3.0 MODEL VERIFICATION & RELIABILITY FACTOR DETERMINATION

The NSP models have been benchmarked against measurements made for PI 1 cycles 17, 18 and 19, and PI 2 cycles 16, 17 and 18 for the CASMO-4/SIMULATE-3 model to quantify the reliability factors to be used in safety related calculations. The approach used was to show that the reliability factors calculated for the CASMO-4/SIMULATE-3 model are less than those approved for the current CASMO/PDQ/DP5 methods of reference 1. Even though the reliability factors calculated for the CASMO-4/SIMULATE-3 model are less than those approved for the current CASMO/PDQ/DP5 methods, the reliability factors listed for the currently approved methods will continue to be used with the following exceptions. The temperature coefficient reliability factor will be changed to be consistent with the results of the CASMO-4/SIMULATE-3 model. The basis for this change is that the magnitude of the single sided tolerance factor,  $K_c$ , applied for the CASMO/PDQ/DP5 model is inconsistent with the size of the database that was benchmarked for the CASMO-4/SIMULATE-3 model. The Doppler defect reliability factor will be changed to be consistent with the Doppler coefficient reliability factor.

Table 3.0.1 summarizes the reliability factors and biases that will be used in safety related calculations. The reliability factors that were actually calculated from the CASMO-4/SIMULATE-3 model benchmarks are presented within the sub-sections of section 3.0. The remainder of this section is a detailed account of the derivation of these factors.

The term reliability factor (RF) is used to describe the allowances to be used in safety related calculations to assure conservatism. The uncertainty factor ( $1\sigma$ ) is used to describe the actual model accuracy. The reliability factor is always larger than the uncertainty factor.

The term bias is used to describe the statistical difference between an observed or measured distribution and the calculated value.

Appendix A describes the statistical methods used in the evaluation of the uncertainties in the following sections.

During each cycle, measured and calculated parameters will be compared in order to validate and update, if necessary, the reliability factors determined in this section. Results of the validation and any necessary updates for each parameter will be documented as part of the reload safety evaluation for the reload in which the updated values will be used. The updates to the reliability factors will be in accordance with the methods outlined in this section and in Appendix A. In general, if the comparisons for new cycles give higher reliability factors, the higher reliability factors will be used for reload safety evaluations going forward until comparisons indicate that the reliability factors of Table 3.0.1 are again adequate. Reliability factors lower than those listed in Table 3.0.1 will never be used for any reload safety evaluations even if comparisons indicate that they would be valid.

TABLE 3.0.1

Reliability Factors for Prairie Island

Parameter	CASMO-4/SIMULATE-3	
	Reliability Factor	Bias
$F_Q^N$	$RF_{F_Q^N} = 0.062$	0.015
$F_{\Delta H}$	$RF_{F_{\Delta H}} = 0.044$	0
Rod Worth	$RF_{Rods} = 0.10$	0
Temperature Coefficient (pcm/°F)	$RF_M = 1.5$	-1.0
Doppler Coefficient	$RF_D = 0.10$	0
Doppler Defect	$RF_{DD} = 0.10$	0
Boron Worth	$RF_B = 0.10$	0
Delayed Neutron Parameters	$RF_{\beta} = 0.04$	0
$\beta_{eff}$ and $\ell^*$	$RF_{\ell^*} = 0.04$	0



### 3.1 Rod Worth and Boron Worth Benchmarking

During startup physics testing, critical boron concentrations can be measured at various stages of rod insertion. The accuracy of the boron concentration measurements is limited only by the titration accuracy which is estimated to be better than 2%. The approach taken is to benchmark the NSP models to the directly observable parameter, boron.

The data used in the benchmarking represents the actual measured critical statepoints without corrections to bank endpoints. All measured statepoints were included. The results are shown in Table 3.1.1 for the CASMO-4/SIMULATE-3 model.

Table 3.1.1 shows that the standard deviation of the differences between measured and calculated boron end points is 0.6% for the CASMO-4/SIMULATE-3 model. For the 12 data points this gives a reliability factor of 1.6%, which is of the same order of magnitude as the measurement accuracy. Based on the excellent benchmark comparisons of Table 3.1.1, a 10% boron worth reliability factor ( $RF_B$ ) is reasonable and conservative.

Table 3.1.2 shows comparisons of rod worth for the reference bank in terms of boron. This is from comparisons of the unrodded and rodded measured versus calculated boron endpoints. All comparisons are quite good with the exception of P119. Although the percent difference appears large for P119, there is only a difference of 12 ppm between the measured and calculated rod worth. This is a small fraction of the potential error in the boron endpoint measurements due to the titration accuracy of the measurement ( $\sim \pm 35$  ppm for P119). Thus a large part of the rod worth difference for P119 could be attributable to the boron measurement error.

Furthermore, the sample size for the rod worth comparisons of Table 3.1.2 is too small to give meaningful statistics. It is reasonable to expect that as new cycles are benchmarked, and the sample size approaches the size of that available for Table 3.1.1, the statistics will become more consistent with those of Table 3.1.1. However, examination of the comparisons in Table 3.1.2, as well as examination of the measured versus calculated rod worth comparisons determined by boration/dilution and by the rod swap technique (see Table 4.3.1 in section 4), clearly indicates that a 10% rod worth reliability factor ( $RF_{Rods}$ ) is reasonable and conservative.

TABLE 3.1.1

Measured versus Calculated Boron EndpointsCASMO-4/SIMULATE-3 Model

Prairie Island		Rod Position <sup>1</sup>	Boron Endpoints (ppm)		% Difference <sup>2</sup>
Unit	Cycle		Measured	Calculated	
1	17	ARO	1867	1871	-0.2
		A bank in	1725	1728	-0.2
1	18	ARO	1961	1933	1.4
		A bank in	1819	1793	1.4
1	19	ARO	1797	1788	0.5
		A bank in	1680	1659	1.3
2	16	ARO	1812	1806	0.3
		A bank in	1676	1668	0.5
2	17	ARO	1944	1940	0.2
		A bank in	1802	1794	0.4
2	18	ARO	1899	1889	0.5
		A bank in	1755	1742	0.7
Bias = 0.6% $\sigma$ = 0.6%					

<sup>1</sup> Approximate rod bank position

$$^2 \text{ \% Difference} = \frac{(M - C)}{M} * 100\%$$

TABLE 3.1.2

Measured versus Calculated Rod Bank Worths from Boron Endpoints

CASMO-4/SIMULATE-3 Model

Prairie Island		Control Rod Bank	Bank Worth (ppm) <sup>1</sup>		% Difference <sup>2</sup>
Unit	Cycle		Measured	Calculated	
1	17	A Bank	142	143	-0.7
1	18	A Bank	142	140	1.4
1	19	A Bank	117	129	-10.3
2	16	A Bank	136	138	-1.5
2	17	A Bank	142	146	-2.8
2	18	A Bank	144	147	-2.1
Bias = -2.7%      σ = 4.0%					

<sup>1</sup> Bank Worth is determined as the difference between the unrodded and rodded boron endpoints as listed on Table 3.1.1.

<sup>2</sup> % Difference  $\equiv \frac{(M - C)}{M} * 100\%$

### 3.2 Temperature Coefficient Benchmarking

Measurements of the isothermal temperature coefficient (ITC) at HZP are adequately made with a reactivity computer as there usually is no rod motion. When there is rod motion, there is usually sufficient time to allow the flux to stabilize.

The comparisons of the measured ITC to the NSP models are summarized in Table 3.2.1. For the CASMO-4/SIMULATE-3 model the constant bias is -1.0 pcm/°F with a  $1\sigma$  standard deviation of 0.53 pcm/°F.

The temperature coefficient reliability factor is defined as 1.5 pcm/°F for the CASMO-4/SIMULATE-3 model. This assures that the measured ITC will be bounded by the prediction including bias at a 95%/95% level of confidence (assuming a normal distribution). The calculation is shown below (see Appendix A.1).

The bias and reliability factor defined for the temperature coefficient represent a change from the values defined in reference 1. The basis for this change is that the magnitude of the single sided tolerance factor,  $K_c$ , applied for the CASMO/PDQ/DP5 model of reference 1 is inconsistent with the sample size that was benchmarked for the CASMO-4/SIMULATE-3 model for this topical report. It should be noted that the standard deviation calculated for the CASMO-4/SIMULATE-3 model is consistent with that calculated for the CASMO/PDQ/DP5 model in reference 1. Thus it is reasonable to reduce the reliability factor to reflect the greater degrees of freedom of the larger sample of data benchmarked for this topical report.

The bias and RF defined in this section will be applied to both calculations of isothermal temperature coefficients (ITC) and moderator temperature coefficients (MTC) for safety related calculations.

$$\text{CASMO-4/SIMULATE-3: } RF = K_c(N) * \sigma = 2.74(0.53) = 1.5 \text{ pcm/°F}$$

$$\text{Bias} = -1.0 \text{ pcm/°F}$$

TABLE 3.2.1

Measured versus Calculated Isothermal Temperature Coefficients

BOC, HZP

CASMO-4/SIMULATE-3 Model

Prairie Island		Rod Position <sup>1</sup>	ITC (pcm/°F)		Difference <sup>2</sup> (pcm/°F)
Unit	Cycle		Measured	Calculated	
1	17	ARO	0.70	1.91	-1.21
		A bank in	0.20	0.81	-0.61
1	18	ARO	0.60	1.94	-1.34
		A bank in	-0.40	1.14	-1.54
1	19	ARO	-0.75	0.47	-1.22
		A bank in	-1.75	-0.59	-1.16
2	16	ARO	1.86	1.55	0.31
		A bank in	-0.12	0.61	-0.73
2	17	ARO	1.20	1.93	-0.73
		A bank in	-0.60	0.72	-1.32
2	18	ARO	0.44	1.53	-1.09
		A bank in	-1.35	0.28	-1.63
Bias = -1.0 pcm/°F $\sigma = 0.53$ pcm/°F					

<sup>1</sup> Approximate rod bank position

<sup>2</sup> Difference  $\equiv (M - C)$

### 3.3 Doppler Coefficient

Measurements can be made which are directed at determining the Doppler coefficient at various power levels. The uncertainty associated with such measurement (e.g., rod repositioning) and with the interpretation (e.g., reactivity inference by a reactivity computer) are such that results are not reliable for direct validation of the calculational model. Consequently, an indirect approach is taken.

The primary variable in the calculation of Doppler effects using the CASMO-4/SIMULATE-3 model is the fuel temperature. A change in fuel temperature associated with a power change results in a reactivity change due to the change in the resonance absorption.

The algorithm in SIMULATE-3 that determines the model change in reactivity due to the fuel temperature change uses data calculated by CASMO-4. The approach is to determine the accuracy of CASMO-4 in calculating the change in the resonance integral ( $\Delta RI$ ) due to a known fuel temperature increase, then use engineering judgement to bound this uncertainty to assure conservatism.

CASMO-3 has been previously benchmarked against Hellstrand's measured resonance integrals and Doppler coefficients (reference 2) and the results are within the measured uncertainty of 8%. Further, CASMO-3 and CASMO-4 calculated Doppler coefficients have been compared to Monte Carlo calculations done with MCNP-3A (reference 3). The CASMO-3 and CASMO-4 calculated Doppler Coefficients of reference 3 are identical indicating that there is good agreement between the CASMO-3 and CASMO-4 Doppler calculation. Thus, by inference, it is reasonable to conclude that CASMO-4 comparisons against Hellstrand's measured resonance integrals and Doppler coefficients would also be consistent with reference 2. The CASMO-4 comparisons to the MCNP-3A Monte Carlo calculations of reference 3 show agreement to within 6%. Based on these results, a 10% reliability factor on the Doppler coefficient is reasonable.

To further support the Doppler coefficient uncertainty, NSP has performed additional comparisons of CASMO-4 to Monte Carlo MCNP-4A calculations. Pincell calculations were performed for the PWR 17x17 lattice previously analyzed by Studsvik of America in reference 3. NSP's results are consistent with those reported by Studsvik indicating a consistent calculation process. Subsequently, pincell calculations were performed specifically for a Prairie Island 14x14 lattice. Figure 3.3.1 presents the results of the NSP comparisons for both pincell calculations. In general figure 3.3.1 shows that the CASMO-4 results are within the MCNP-4A uncertainty band. In view of this, a 10% reliability factor on the Doppler coefficient is reasonable.

In order to demonstrate that a 10% reliability factor on the Doppler defect is also conservative, comparisons were made between ARO, HZP boron endpoint data and the first, equilibrium ARO, HFP boron measurement for each benchmark cycle. The results

of the comparisons are presented in Table 3.3.1. The difference in the change in boron concentration between HZP and HFP is an approximate measure of the power defect, which includes reactivity effects due to the Doppler defect as well as flux redistribution, moderator temperature and fission product build up. Table 3.3.1 shows that the standard deviation of the differences between measured and calculated power defects is 1.5% for the CASMO-4/SIMULATE-3 model. For the six data points this gives a reliability factor of 5.6%, which is largely driven by the small number of data points. Thus, it is conservative to set the Doppler defect reliability factor to 10%.

Based on the preceding results and discussion, the Doppler coefficient reliability factor will be set to 10% and the Doppler defect reliability factor will also be set to 10%.

FIGURE 3.3.1

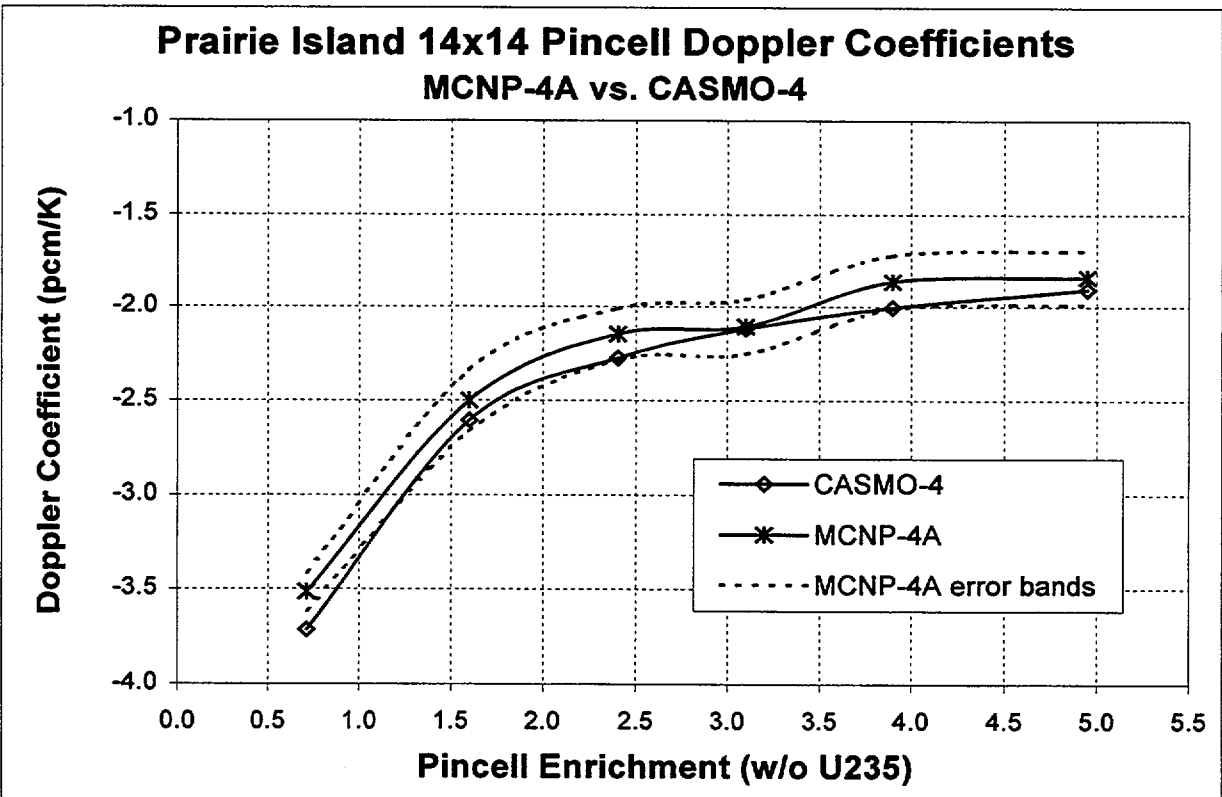
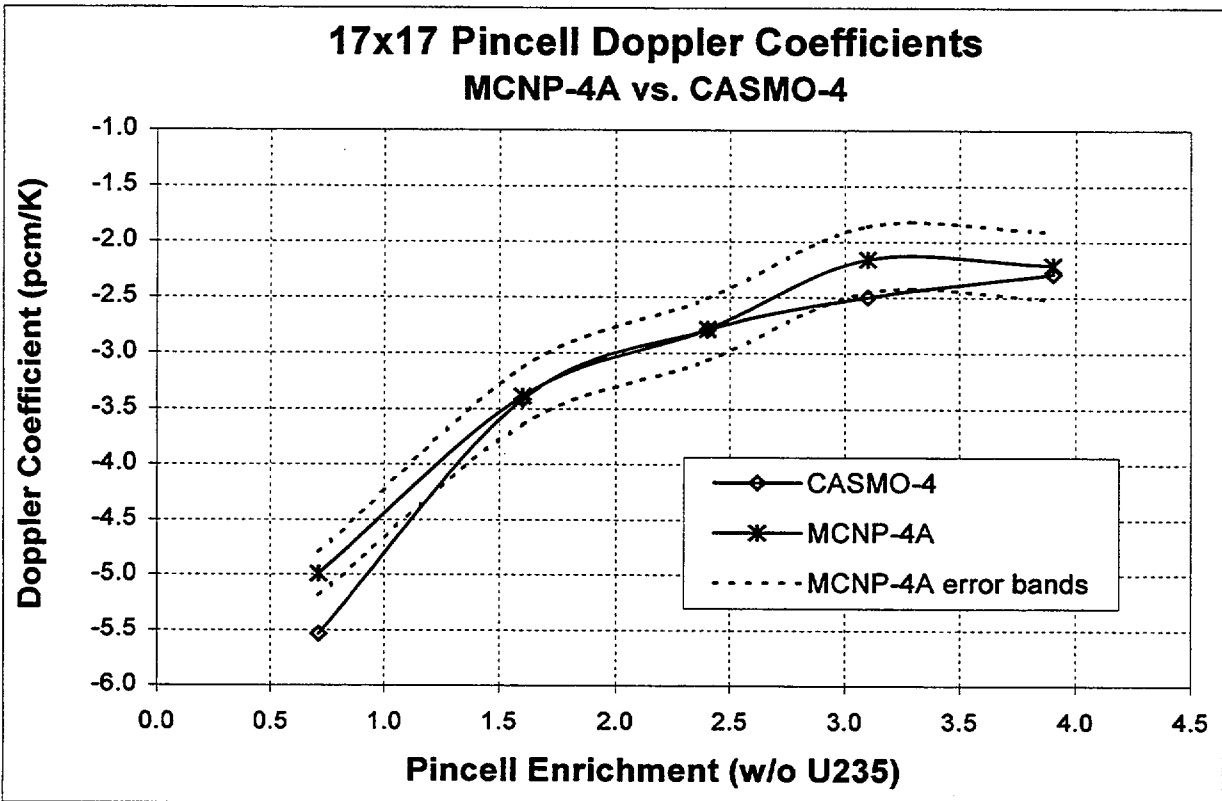




TABLE 3.3.1

Measured versus Calculated Power Defect ComparisonsCASMO-4/SIMULATE-3 Model

Prairie Island		Reactor Conditions	Exposure (GWd/MTU)	Boron Concentration		Power Defect (ppm) <sup>1</sup>		% Difference <sup>2</sup>
Unit	Cycle			Measured	Calculated	Measured	Calculated	
1	17	ARO, HZP	0	1867	1871	512	490	4.3
		ARO, HFP	0.261	1355	1381			
1	18	ARO, HZP	0	1961	1933	544	511	6.1
		ARO, HFP	0.178	1417	1422			
1	19	ARO, HZP	0	1797	1788	510	497	2.5
		ARO, HFP	0.151	1287	1291			
2	16	ARO, HZP	0	1812	1806	493	479	2.8
		ARO, HFP	0.197	1319	1327			
2	17	ARO, HZP	0	1944	1940	534	504	5.6
		ARO, HFP	0.171	1410	1436			
2	18	ARO, HZP	0	1899	1889	533	518	2.8
		ARO, HFP	0.237	1366	1371			
Bias = 4.0% $\sigma$ = 1.5%								

<sup>1</sup> Power defect is calculated as the difference between the HZP and HFP boron concentrations.

$$^2 \text{ \% Difference} \equiv \frac{(M - C)}{M} * 100\%$$

### 3.4 Isotopics

The benchmarking of CASMO-4 to Yankee Rowe Isotopic measurements is discussed in reference 4. The predictions trend well with the measurements. There are no uncertainties applied to the isotopics.

### 3.5 Power Distribution Reliability Factor Determination

The purpose of this section is to discuss the determination of the power distribution reliability factors. The local power distribution reliability factor for  $F_Q$  is discussed in section 3.5.1. The integrated power distribution reliability factor for  $F_{\Delta H}$  is discussed in section 3.5.2. The methodology used to derive the statistics presented in sections 3.5.1 and 3.5.2 are consistent with the methodology presented in reference 1.

The model reliability factor for calculating power distributions is based on comparisons of measured and calculated incore flux detector signals for normal operating core conditions.

The incore detector signals are corrected to account for such things as detector sensitivity, drift, and background. These corrected signals, or reaction rates, are compared to reaction rates calculated with the CASMO-4/SIMULATE-3 model in order to derive model reliability factors.

The simulated reaction rates are calculated in a manner which is consistent with the calculation of local power peaking factors for the purpose of reload safety evaluations and are obtained directly from SIMULATE-3 calculated two group fluxes and fission cross sections in the instrument locations. The reaction rates are calculated explicitly for each instrumented location for the same number of axial increments as exists for the measured data. This is a more rigorous technique than was used in reference 1 and eliminates the truncated Fourier sine expansion technique that was used and is discussed in reference 1.

The calculated and measured reaction rates are normalized to put the measured and calculated values on a common basis consistent with the definition of  $F_Q$  and  $F_{\Delta H}$ . The measurement uncertainty in core thermal power is accounted for in the transient and LOCA analyses.

A total of 81 core statepoints, or flux maps, were chosen for the purpose of comparing measured and simulated incore reaction rates for the CASMO-4/SIMULATE-3 model. These statepoints span operating cycles 18 and 19 for Prairie Island Unit 1 and cycles 17 and 18 for Prairie Island Unit 2. The specific core conditions for each of the statepoints are given in table 3.5.1.

Typical examples of the comparisons of measured and predicted reaction rates are provided in Figures 3.5.1 through 3.5.36. Results for three flux maps for the Prairie Island Unit 1 Cycles 18 and 19 and Unit 2 Cycles 17 and 18 benchmark cycles are presented. The flux maps correspond approximately to beginning of cycle, middle of cycle, and end of cycle (BOC, MOC, EOC) burnup. Three figures are presented for each flux map. The first figure represents the differences between the measured and predicted integrated reaction rates for all instrumented locations. The second and third figures represent axial comparisons in two specific instrumented core locations. The two core locations were chosen as typical of regions of high power density.

### 3.5.1 Local Power Distribution - Reliability Factor on $F_Q^N$

The reliability factor, RF, is defined as a single value of  $\Delta F_Q$  such that  $F_Q(i,j,k)$  calculated plus  $\Delta F_Q$  has a 95% probability at a 95% confidence level of being conservative with respect to the measured  $F_Q(i,j,k)$ . The subscripts c and m will be used to denote calculated and measured values.  $F_Q(i,j,k)$  is the local pin peak power determined for all i,j,k locations in the core. This value cannot be measured directly. What is measured by the detector system is the local reaction rate in the instrument thimble:

$$RR_m = \phi \Sigma_f \text{ (measured)}$$

The CASMO-4/SIMULATE-3 model has been used to calculate the reaction rate in the instrument thimbles:

$$RR_c = \phi \Sigma_f \text{ (calculated)}$$

The observed difference distribution (ODD) has then been calculated by taking the difference of these two values for all measured locations in the reactor core:

$$ODD = RR_m - RR_c$$

It is important to note that the ODD is not the difference between nodal powers but rather is the difference between local fission rate values. It is assumed that the observed difference is equal to  $\Delta F_Q$  between a measured and calculated local  $F_Q(i,j,k)$ . This is a valid assumption since the measured and calculated reaction rates are also local values and are proportional to  $F_Q$ . The uncertainty determined from the above comparisons for the instrument thimble is the same as the uncertainty that would be determined in a fuel pin, if that pin could be instrumented, except for a small self-shielding or flux depression in the pin which is not present in the fission chamber. The impact of this flux depression on the  $F_Q$  uncertainty is assumed to be negligible.

The observed difference distribution determined above includes the uncertainties in the calculational model as well as the uncertainties in the measurement instrumentation. The calculational model uncertainty includes uncertainty in the calculation of the nodal power and in the conversion factors from nodal powers to pin powers, which is assumed to be the same as the total uncertainty in the calculated reaction rates. Therefore, the total uncertainty in the local pin power can be written as follows:

$$RF_{FQ} = \sigma_{FQ,95}$$

where  $\sigma_{FQ,95}$  is determined from the ODD.

The distribution of observed differences between measured and calculated instrument signals for all 81 core state points was determined. For each trace, data at axial locations corresponding to the top and bottom of the reactor core as well as data at axial locations

corresponding to assembly grid locations were excluded from consideration. These are areas of steep flux gradients where small errors in instrument position may result in large differences in measured to calculated values. The reaction rates in these areas will be lower than those in adjacent areas due to the flux depression effects of the grids and the core axial boundaries. Since the peak power will never occur in one of these locations, it is reasonable to exclude these data points from the determination of the observed differences density function. For the 81 flux maps compared, the total number of observations used was 98,040. The total number of observations excluded was 59,340.

As is consistent with reference 1, and assuming a non-normal distribution, all subsequent statistical analysis were performed using the methods described in Appendix A.2. To ensure a conservative reliability factor at all power levels, the sample was divided into subintervals as a function of power (see Figure 3.5.37). Each subinterval contained approximately 16,340 observations. A reliability factor was calculated for each subinterval using the methods described in Appendix A.2. To remain consistent with reference 1, the most conservative subinterval, determined from the sum of the reliability factor and bias, will be used. The following statistics represent the most conservative subinterval. The distribution of observed differences for the most conservative subinterval is shown in Figure 3.5.38.

The first step using the methods of Appendix A.2 is to determine the mean ( $\mu_{mc}$ ) and standard deviation ( $\sigma_{mc}$ ) of the measured versus calculated values:

$$\mu_{mc} = \frac{\sum_{i=1}^n e_i}{n} = 0.008440$$

$$\sigma_{mc} = \sqrt{\frac{\sum_{i=1}^n (e_i - \mu_{mc})^2}{n - 1}} = 0.02945$$

where:  $e_i$  = i'th observed difference  
 $n$  = total number of observations

The second step is to transform  $e_i$  to standard measure using the following formula:

$$Z_i = \frac{e_i - \mu_{mc}}{\sigma_{mc}}$$

The resulting variates,  $Z_i$ , were then sorted into ascending order (see Figure 3.5.39). A value of  $Z_i$  was chosen as an estimate of the 95<sup>th</sup> percentile of the distribution:

$$Z_{15,523} = Q_{95} = 1.531$$

This implies that 95% of the errors are likely to be less than 1.531 standard deviations from the mean. It remains then to calculate a 95% confidence interval on  $Q_{95}$  using the following formula:

$$\text{Var}Q_{95} = \sigma_{Q_{95}}^2 = \frac{q(1-q)}{n \cdot f_1^2}$$

where:  $q$  = the quantile (.95)

$n$  = number of independent observations in sample

$f_1$  = ordinate of the density function of the distribution of observed differences at abscissa  $q$

Due to the dependence of the observed differences with axial height,  $n$  was reduced by a factor of three. This is consistent with reference 1. See Appendix A.2 for the determination of the reduction factor.

It is necessary to obtain an estimate of  $f_1(.95)$ . This was done by applying a linear regression analysis on a short interval of the cumulative distribution function (CDF) of  $Z$  in the region of the 95<sup>th</sup> percentile (see Figure 3.5.40). The estimated slope of the CDF (the straight line in Figure 3.5.40) is an estimate of the ordinate density function. The slope is calculated as 0.09826. This gives:

$$\text{Var}Q_{95} = \sigma_{Q_{95}}^2 = \frac{q(1-q)}{n \cdot f_1^2} = \frac{0.95(1-0.95)}{\left[\frac{16,340}{3}\right](0.09826)^2} = 0.0009033$$

and,

$$\sigma_{Q_{95}} = \sqrt{\text{Var}Q_{95}} = 0.03005$$

The estimate of the upper limit on  $Q_{95}$  is:

$$K_c \sigma_{Q_{95}} = 1.645 * 0.03005 = 0.04943$$

thus:

$$Q_{95} \leq 1.531 + 0.04943 = 1.580$$

The upper limit is then 1.580 which gives the following as the 95% confidence level that the calculated reaction rate,  $RR_c$ , will be conservative with respect to the measured reaction rate,  $RR_m$ :

$$RR_m = RR_c + 1.580 * \sigma_{mc} = RR_c + 1.580 * 0.02945 = RR_c + 0.047$$

therefore  $RF_{FQ} = \sigma_{FQ,95} = 0.047$

Note that this value includes measurement error which adds to the conservatism of the calculation.

For safety related calculations,  $RF_{FQ}$  and  $\mu_{mc}$  are applied to the calculated  $F_Q$  as additive factors as follows:

$$F_Q(\text{safety}) = F_Q(\text{calculated}) + \mu_{mc} + RF_{FQ}$$

For the CASMO-4/SIMULATE-3 model, as documented above,  $RF_{FQ} = 0.047$  and  $\mu_{mc} = 0.008$  for a total  $\mu_{mc} + RF_{FQ} = 0.055$ . This is less than the  $\mu_{mc} + RF_{FQ} = 0.077$  previously approved in reference 1 for the CASMO/PDQ/DP5 model. However, for conservatism, the uncertainty  $\mu_{mc} + RF_{FQ} = 0.077$  previously approved in reference 1 will continue to be used.

In addition, the measured versus calculated reaction rates will be reviewed on an ongoing basis to ensure that the reported uncertainty  $\mu_{mc} + RF_{FQ} = 0.077$  remains conservative. If a higher  $\mu_{mc} + RF_{FQ}$  is calculated it will be used until the statistics show the sum to be lower than 0.077 again. However, a total  $\mu_{mc} + RF_{FQ}$  less than 0.077 shall never be used.

### 3.5.2 Integrated Power Distribution - Reliability Factor on $F_{\Delta H}$

The reliability factor, RF, is defined as a single value of  $\Delta F_{\Delta H}$  such that  $F_{\Delta H}(i,j)$  calculated plus  $\Delta F_{\Delta H}$  has a 95% probability at a 95% confidence level of being conservative with respect to the measured  $F_{\Delta H}(i,j)$ . The subscripts c and m will be used to denote calculated and measured values.  $F_{\Delta H}(i,j)$  is the integrated pin power determined for all i,j locations in the core. This value cannot be measured directly. What is measured by the detector system is the local reaction rate in the instrument thimble which are then integrated over all axial locations:

$$IRR_m = \sum_{i=1}^n [\phi \Sigma_f]_n (\text{measured})$$

The CASMO-4/SIMULATE-3 models have been used to calculate the reaction rate in the instrument thimbles which are then integrated over all axial locations:

$$IRR_c = \sum_{i=1}^n [\phi \Sigma_f]_n (\text{calculated})$$

The observed difference distribution (ODD) has then been calculated by taking the difference of these two values for all measured locations in the reactor core:

$$ODD = IRR_m - IRR_c$$

The observed difference distribution determined above includes the uncertainties in the calculational model, the uncertainties in the measurement instrumentation and the uncertainties in conversion factors from nodal powers to instrument value. The calculational model uncertainty includes uncertainty in the calculation of the nodal powers as well as uncertainty in the local pin powers. Therefore the uncertainty in the local integrated pin power can be written as follows:

$$RF_{F\Delta H} = \sigma_{F\Delta H,95}$$

where  $\sigma_{F\Delta H,95}$  is determined from the ODD.

The distribution of observed differences between measured and calculated integrated instrument signals for all 81 statepoints was determined for the CASMO-4/SIMULATE-3 model and is shown in Figure 3.5.42. All valid axial values are used to calculate the integrated value. The total number of integrated observations used was 2,580.

As is consistent with reference 1, and assuming a non-normal distribution, all subsequent statistical analysis has been performed using the methods described in Appendix A.2. Consistent with section 3.5.1, the sample was divided into subintervals as a function of power (see Figure 3.5.41). Since there is no clear dependence with power, data for the entire sample may be used for the statistical analysis and resultant reliability factor and bias. This is consistent with reference 1. The cumulative distribution function (CDF) and the CDF in the region of the 95<sup>th</sup> percentile are given in Figures 3.5.43 and 3.5.44 respectively. The significant parameters calculated for this distribution are as follows:

$$\mu_{mc} = 0.000467$$

$$\sigma_{mc} = 0.01128$$

$$Q_{95} = 1.635$$

$$\sigma_{Q_{95}} = 0.06079$$

$$K_c \sigma_{Q_{95}} = 0.1000$$

$$IRR_m = IRR_c + 0.020$$

$$RF_{F\Delta H} = \sigma_{F\Delta H,95} = 0.020$$

where:  $IRR_m$  = measured integrated reaction rate  
 $IRR_c$  = calculated integrated reaction rate

No dependence of the observed difference with position was found. Therefore, n was not



reduced. This is consistent with reference 1.

For safety related calculations,  $RF_{F\Delta H}$  and  $\mu_{mc}$  are applied to the calculated  $F_{\Delta H}$  as additive factors as follows:

$$F_{\Delta H} (\text{safety}) = F_{\Delta H} (\text{calculated}) + \mu_{mc} + RF_{F\Delta H}$$

For the CASMO-4/SIMULATE-3 model, as documented above,  $RF_{F\Delta H} = 0.020$  and  $\mu_{mc} = 0.000467$  for a total  $\mu_{mc} + RF_{FQ} = 0.020$ . This is less than the  $\mu_{mc} + RF_{F\Delta H} = 0.044$  previously approved in reference 1 for the CASMO/PDQ/DP5 model. However, for conservatism, the uncertainty  $\mu_{mc} + RF_{F\Delta H} = 0.044$  previously approved in reference 1 will continue to be used.

In addition, the measured versus calculated integrated reaction rates will be reviewed on an ongoing basis to ensure that the reported uncertainty for the entire sample  $\mu_{mc} + RF_{F\Delta H} = 0.044$  remains conservative. If a higher  $\mu_{mc} + RF_{F\Delta H}$  is calculated it will be used until the statistics show the sum to be lower than 0.044 again. However, a total  $\mu_{mc} + RF_{F\Delta H}$  less than 0.044 shall never be used.

TABLE 3.5.1

Full Power Statepoints

Prairie Island		Map	Exposure (GWd/MTU)	% of Full Power	Rod Bank D Position (Steps)	Boron Concentration (ppm)
Unit	Cycle					
2	17	3	0.171	99.8	218	1410
		6	1.256	99.9	218	1338
		7	2.420	99.9	218	1280
		8	3.501	99.8	222	1218
		9	4.547	99.9	218	1155
		10	5.436	99.6	218	1104
		12	6.503	99.8	218	1034
		13	7.660	99.8	218	970
		14	8.710	99.9	218	917
		15	9.767	99.9	218	863
		16	10.732	99.9	218	807
		17	11.808	99.9	218	752
		18	12.892	99.9	218	689
		19	13.898	99.9	218	624
		22	14.858	99.9	218	543
		23	15.867	99.9	218	459
		24	17.028	99.9	218	364
		25	18.112	99.8	218	272
		26	19.193	99.8	218	178
		27	20.276	99.9	219	86
28	21.360	99.0	228	0		
29	21.587	94.4	228	0		
30	21.869	87.3	228	0		
1	18	4	0.178	99.9	218	1417
		7	1.303	99.8	218	1329
		8	2.425	99.9	218	1278
		9	3.039	99.9	218	1244
		10	4.169	99.9	218	1183
		11	5.089	99.9	218	1118
		12	6.134	99.9	218	1060
		13	7.247	99.9	218	1005
		14	8.303	99.9	218	956
		15	9.395	99.9	218	904
16	10.479	99.9	218	862		
		17	11.489	100.0	218	824

TABLE 3.5.1 (continued)

Full Power Statepoints

Prairie Island		Map	Exposure (GWd/MTU)	% of Full Power	Rod Bank D Position (Steps)	Boron Concentration (ppm)
Unit	Cycle					
1	18	18	12.333	99.9	218	767
		19	13.456	99.8	218	694
		20	14.540	99.9	218	611
		21	15.615	99.9	218	512
		23	16.624	99.8	218	408
		24	17.394	99.9	218	338
		25	18.475	99.8	218	232
		26	19.556	99.9	218	138
		27	20.601	99.8	221	49
		28	21.296	97.6	228	0
		29	21.627	89.9	228	0
2	18	5	0.237	99.8	218	1366
		8	1.287	99.9	218	1298
		9	2.105	99.9	218	1257
		10	3.154	99.8	222	1207
		11	4.285	99.8	218	1131
		12	5.360	99.9	218	1064
		13	6.412	99.9	218	1020
		14	7.495	99.8	218	961
		15	8.586	99.9	218	911
		16	9.597	99.9	218	870
		17	10.685	99.9	218	826
		18	10.959	99.8	218	815
		20	11.551	100.0	218	750
		21	12.679	99.9	218	698
		22	13.808	99.9	218	627
		23	14.936	99.9	218	543
		24	16.000	99.9	218	453
25	17.128	99.9	218	355		
26	18.334	99.9	218	251		
27	19.536	99.8	218	143		
1	19	3	0.151	99.9	218	1287
		6	1.223	99.9	218	1199
		7	2.345	99.8	218	1129

TABLE 3.5.1 (continued)

Full Power Statepoints

Prairie Island		Map	Exposure (GWd/MTU)	% of Full Power	Rod Bank D Position (Steps)	Boron Concentration (ppm)
Unit	Cycle					
1	19	8	3.466	99.9	218	1055
		10	5.676	99.8	219	910
		11	6.717	99.9	218	830
		12	7.840	99.9	218	760
		13	8.913	99.9	218	703
		14	9.997	99.9	218	648
		15	11.122	99.8	218	589
		16	11.732	99.8	218	545
		17	12.889	99.9	218	473
		18	13.785	99.9	218	406
		19	14.948	99.9	218	311
		20	15.990	99.9	218	225

FIGURE 3.5.1

# PI Unit 2 Cycle 17 Measured versus Calculated Integrated Detector Response Differences

Map 217-03, 0.171 GWd/MTU  
100% Power, ARO, EQ XENON (HFP Map)

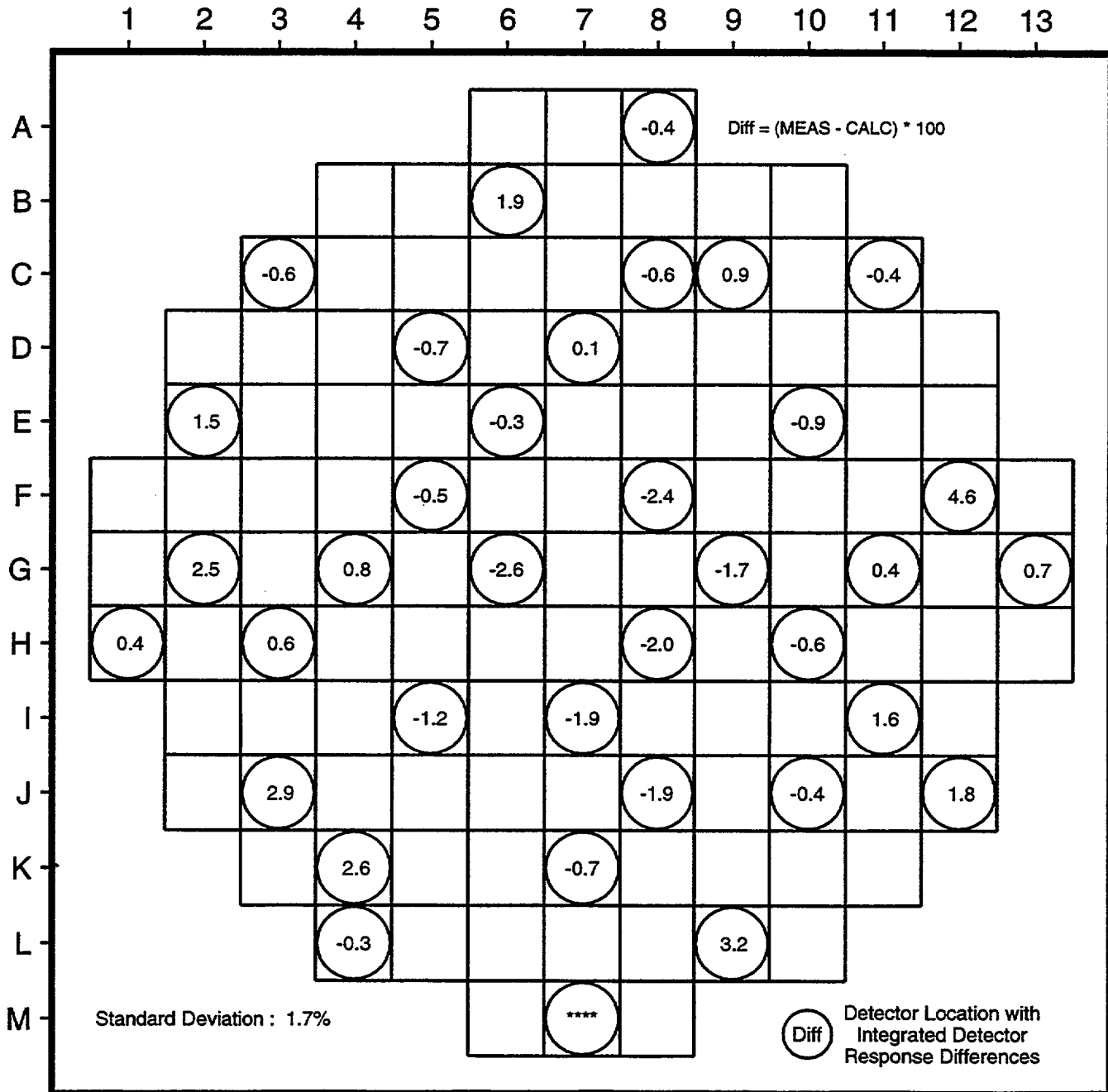


FIGURE 3.5.2

# PI Unit 2 Cycle 17 Measured versus Calculated Detector Response

Map 217-03, 0.171 GWd/MTU  
100% Power, ARO, EQ XENON (HFP Map)

THIMBLE G-4  
Fresh 4.95 w/o U235, 16 pin 8 w/o Gd

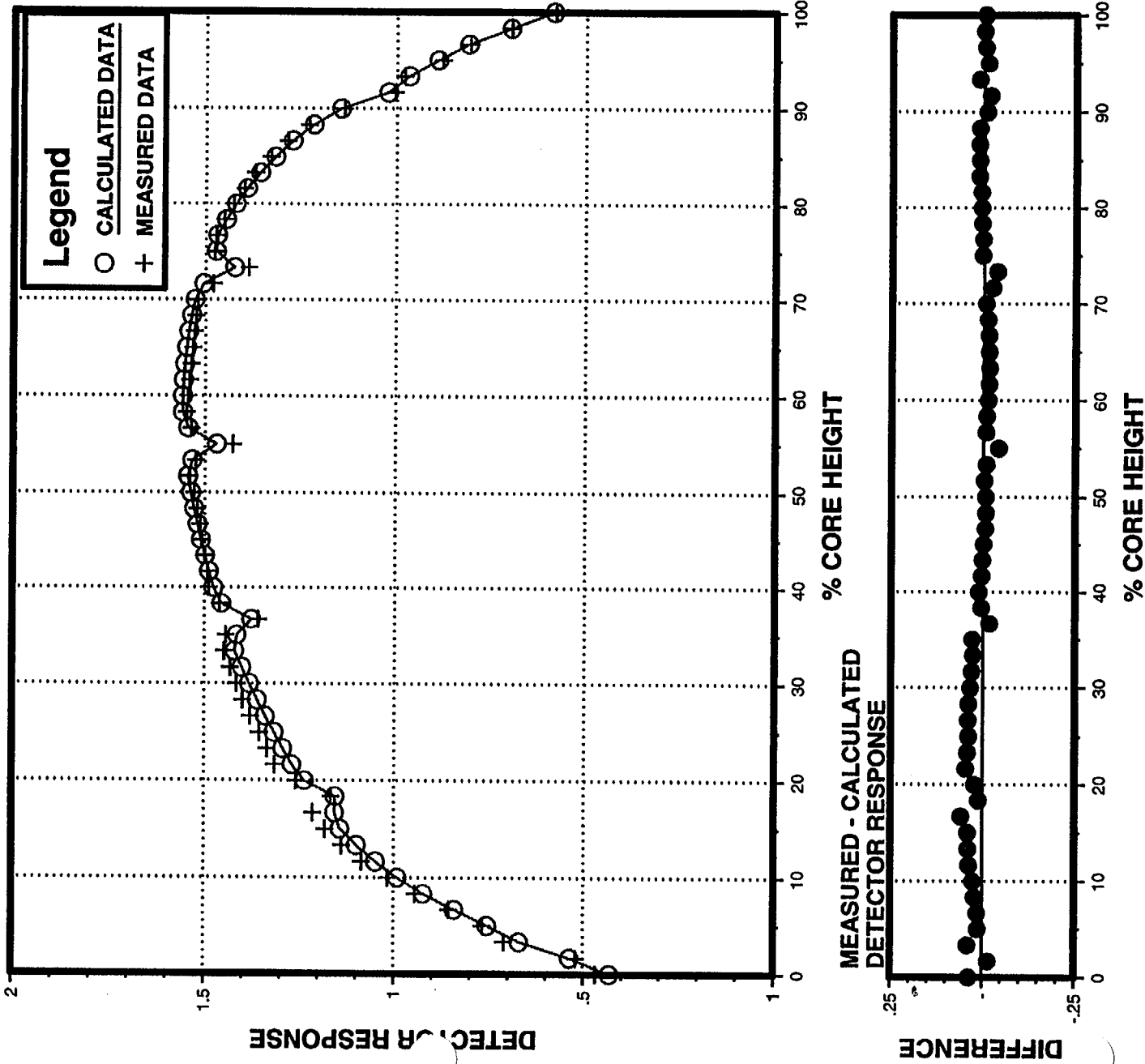


FIGURE 3.5.3

# PI Unit 2 Cycle 17 Measured versus Calculated Detector Response

Map 217-03, 0.171 GWd/MTU  
100% Power, ARO, EQ XENON (HFP Map)  
THIMBLE C-9  
Fresh 4.95 w/o U235, 20 pin 8 w/o Gd

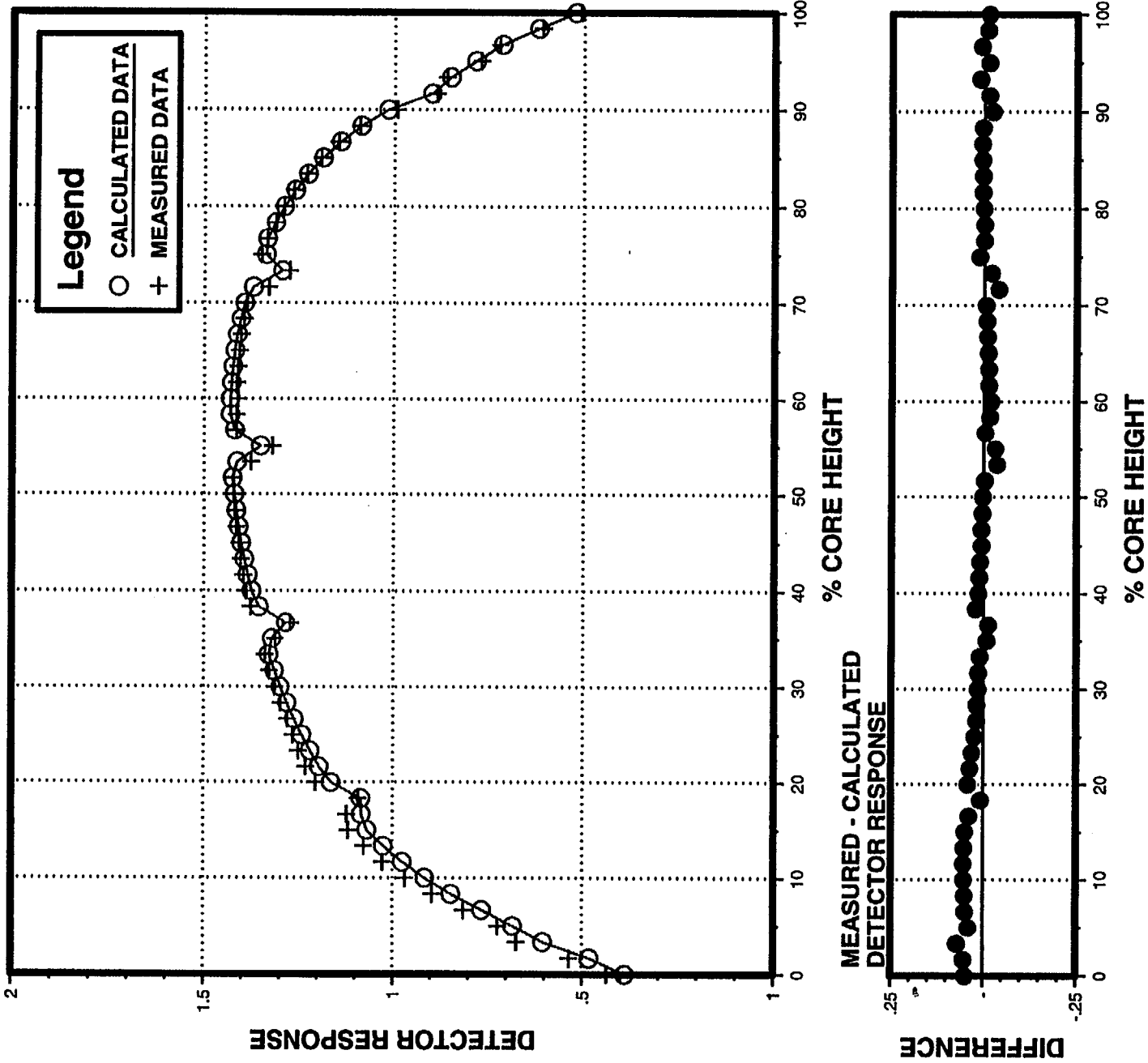


FIGURE 3.5.4

# PI Unit 2 Cycle 17 Measured versus Calculated Integrated Detector Response Differences

Map 217-17, 11.808 GWd/MTU  
100% Power, ARO, EQ XENON (HFP Map)

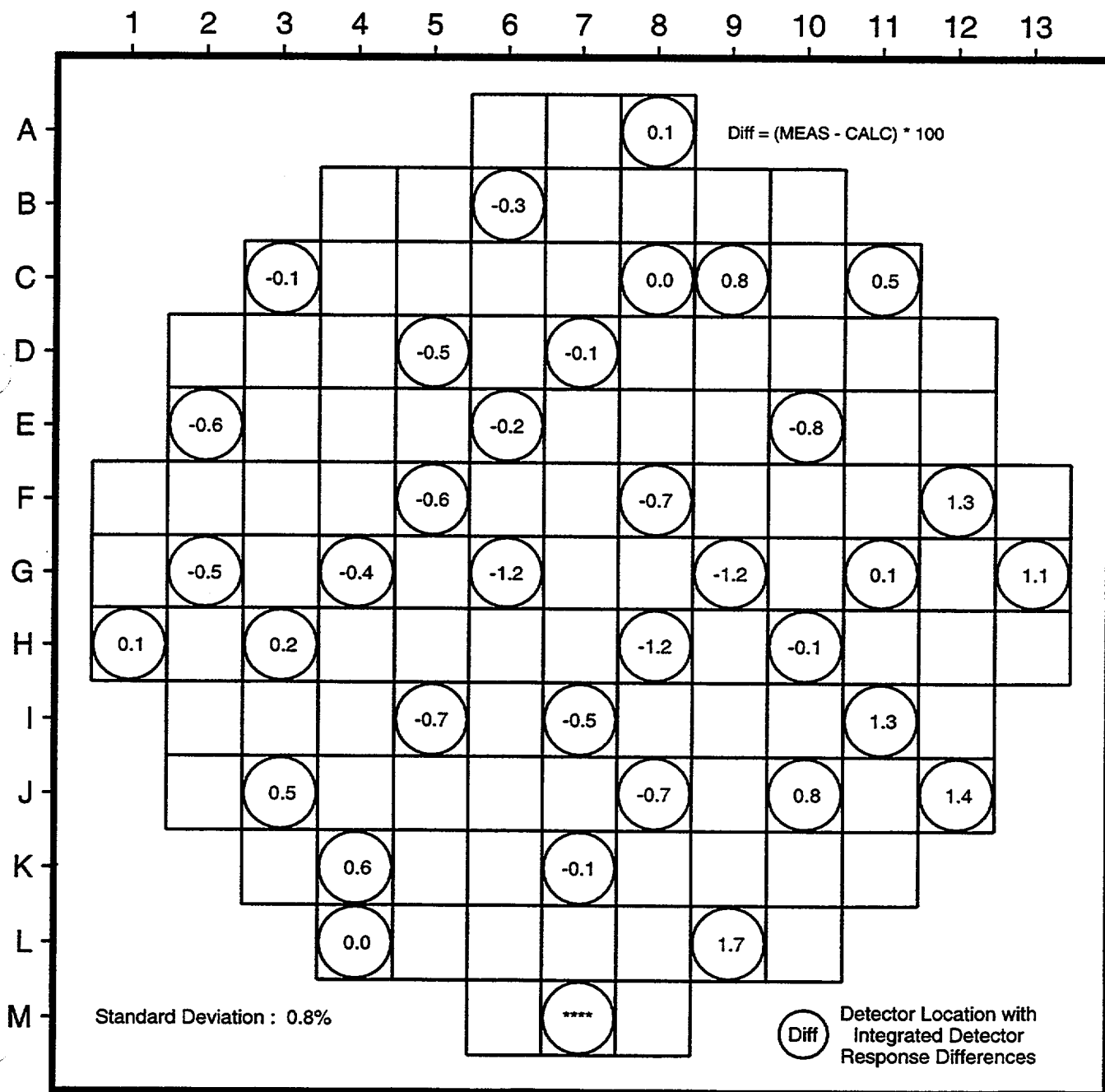




FIGURE 3.5.5

# PI Unit 2 Cycle 17 Measured versus Calculated Detector Response

Map 217-17, 11.808 GWd/MTU  
100% Power, ARO, EQ XENON (HFP Map)

THIMBLE G-4  
Fresh 4.95 w/o U235, 16 pin 8 w/o Gd

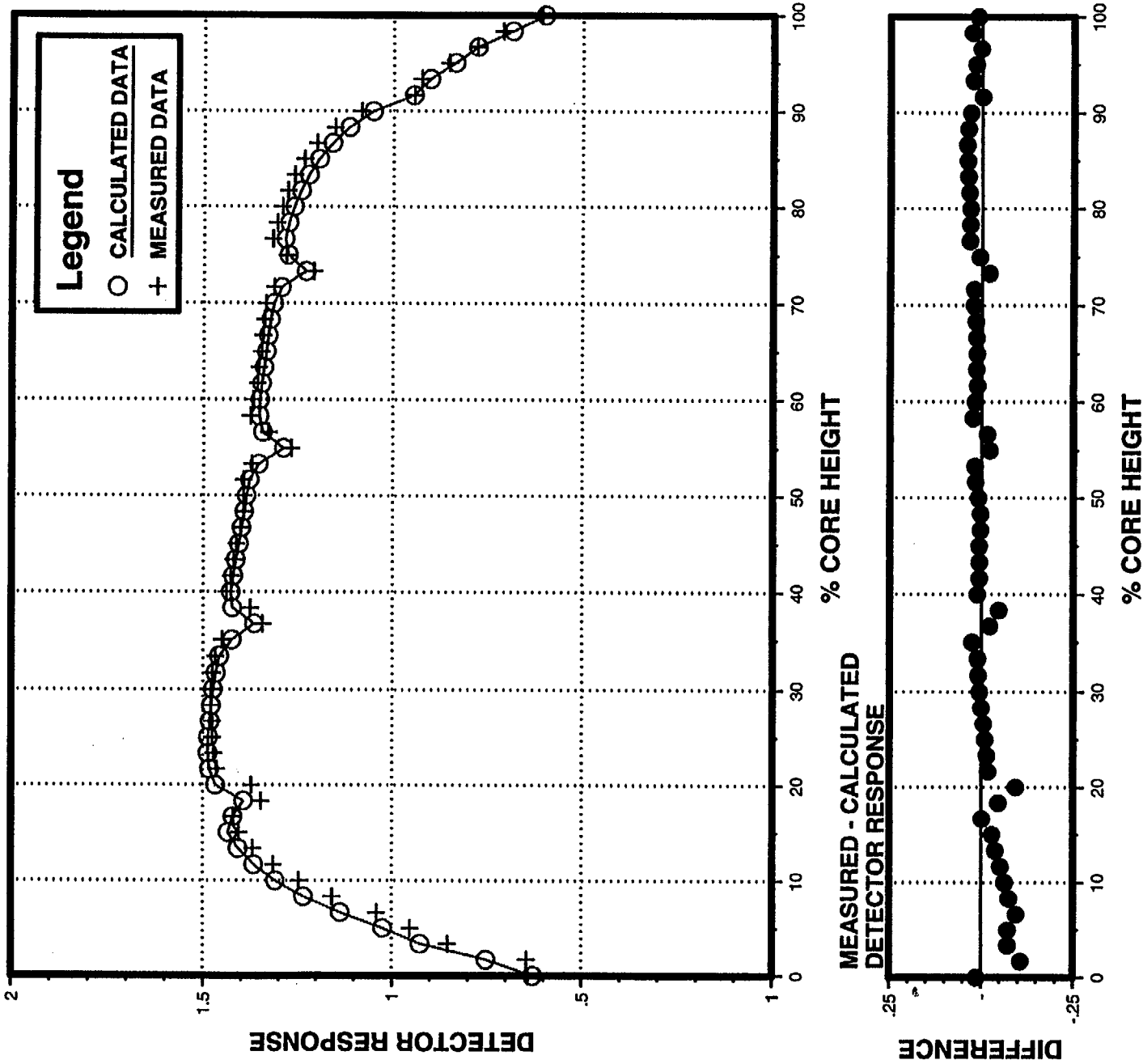


FIGURE 3.5.6

# PI Unit 2 Cycle 17 Measured versus Calculated Detector Response

Map 217-17, 11.808 Gwd/MTU  
100% Power, ARO, EQ XENON (HFP Map)

THIMBLE C-9  
Fresh 4.95 w/o U235, 20 pin 8 w/o Gd

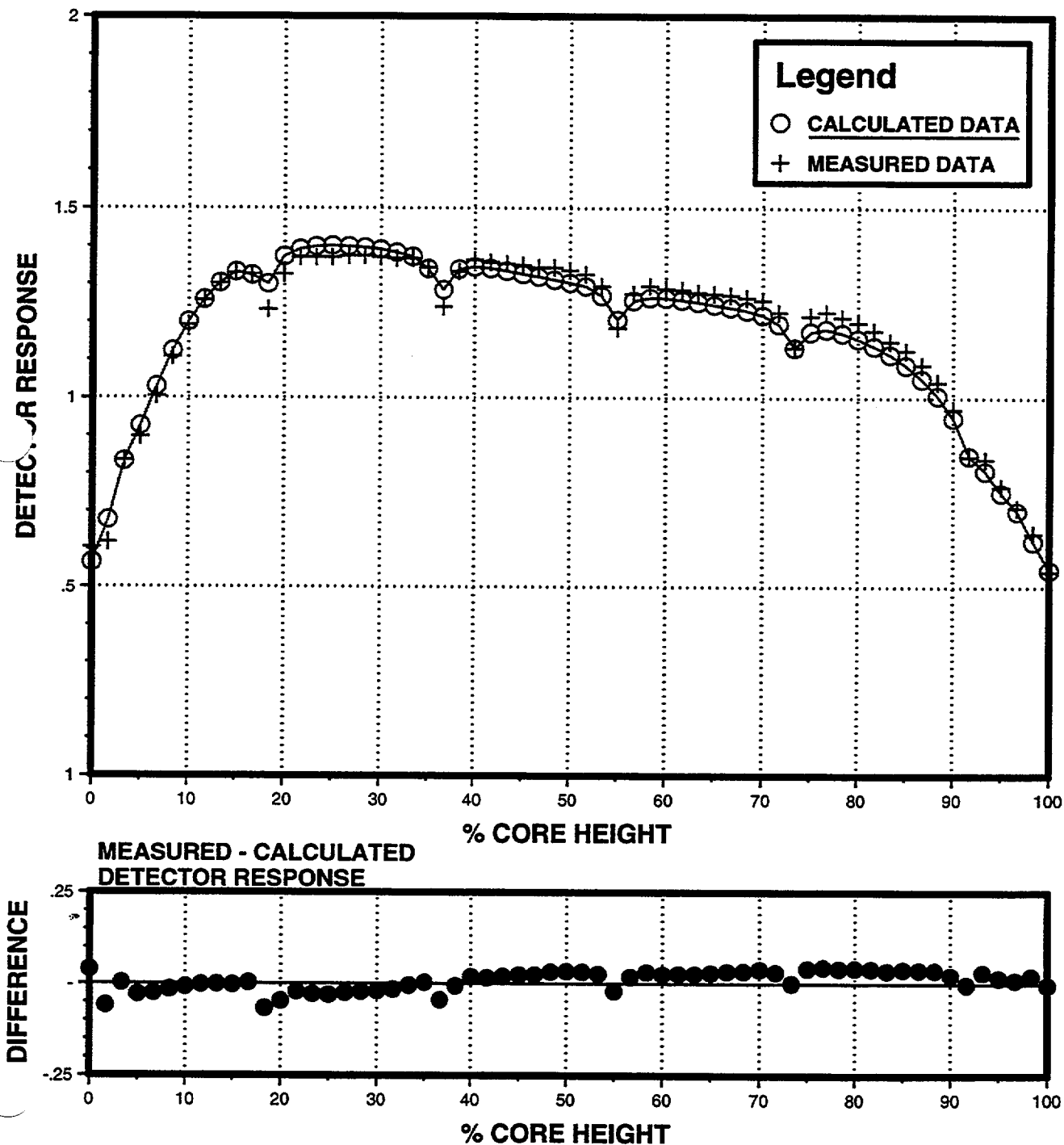


FIGURE 3.5.7

# PI Unit 2 Cycle 17 Measured versus Calculated Integrated Detector Response Differences

**Map 217-30, 21.869 GWd/MTU  
87% Power, ARO, EQ XENON (Coast Map)**

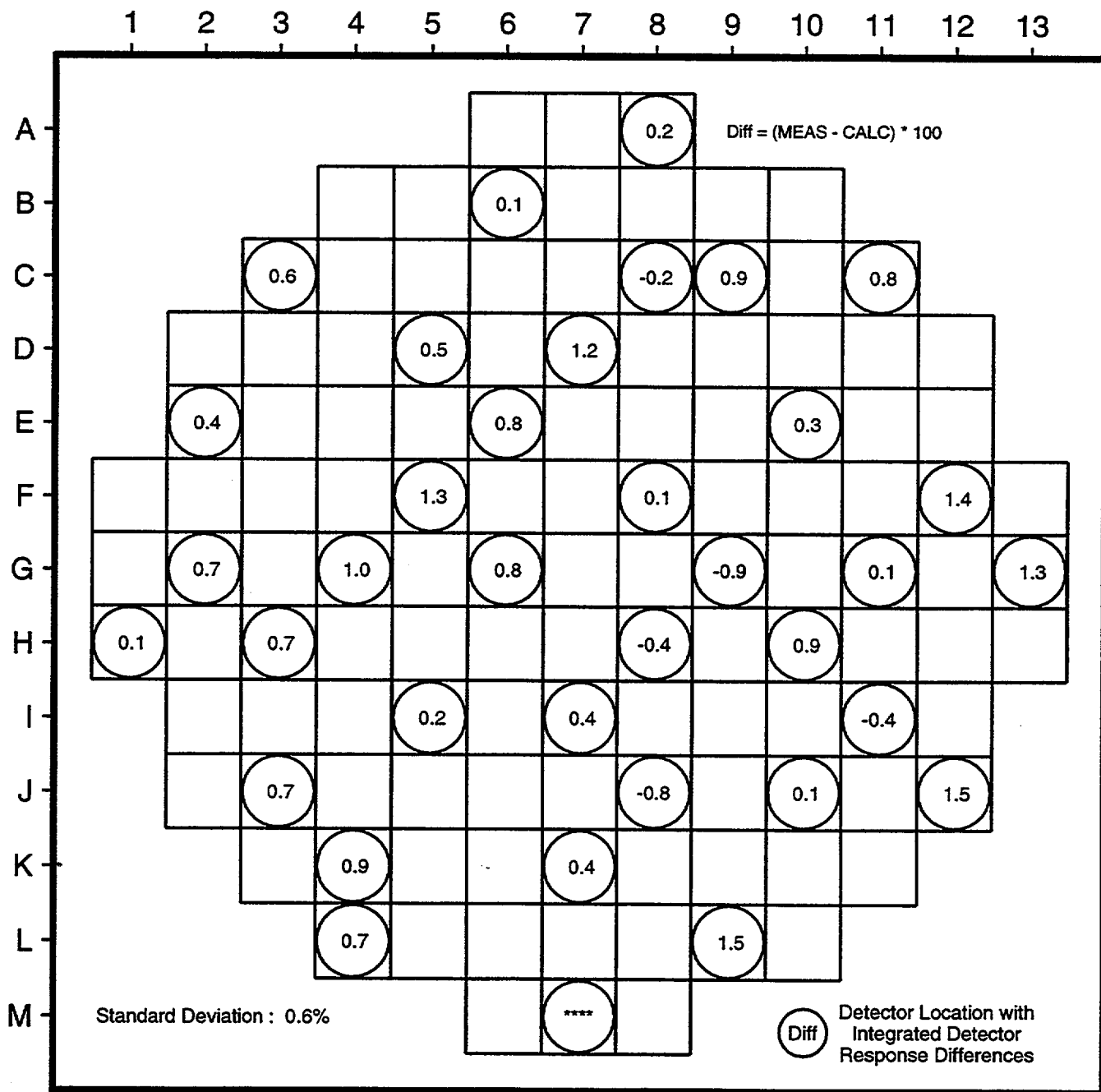


FIGURE 3.5.8

# PI Unit 2 Cycle 17 Measured versus Calculated Detector Response

Map 217-30, 21.869 GWd/MTU  
87% Power, ARO, EQ XENON (Coast Map)

THIMBLE G-4  
Fresh 4.95 w/o U235, 16 pin 8 w/o Gd

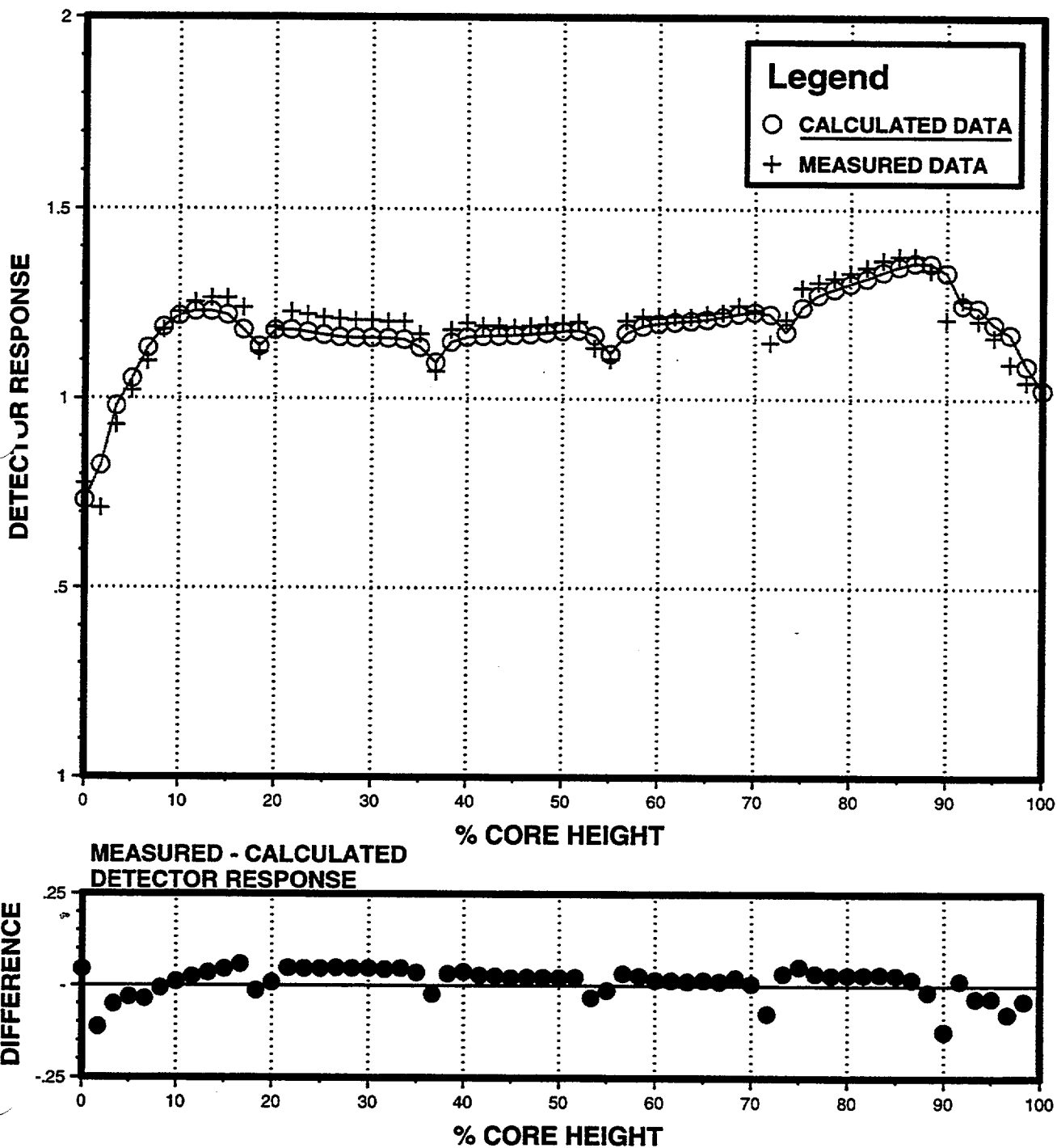


FIGURE 3.5.9

# PI Unit 2 Cycle 17 Measured versus Calculated Detector Response

Map 217-30, 21.869 GWd/MTU  
87% Power, ARO, EQ XENON (Coast Map)

THIMBLE C-9

Fresh 4.95 w/o U235, 20 pin 8 w/o Gd

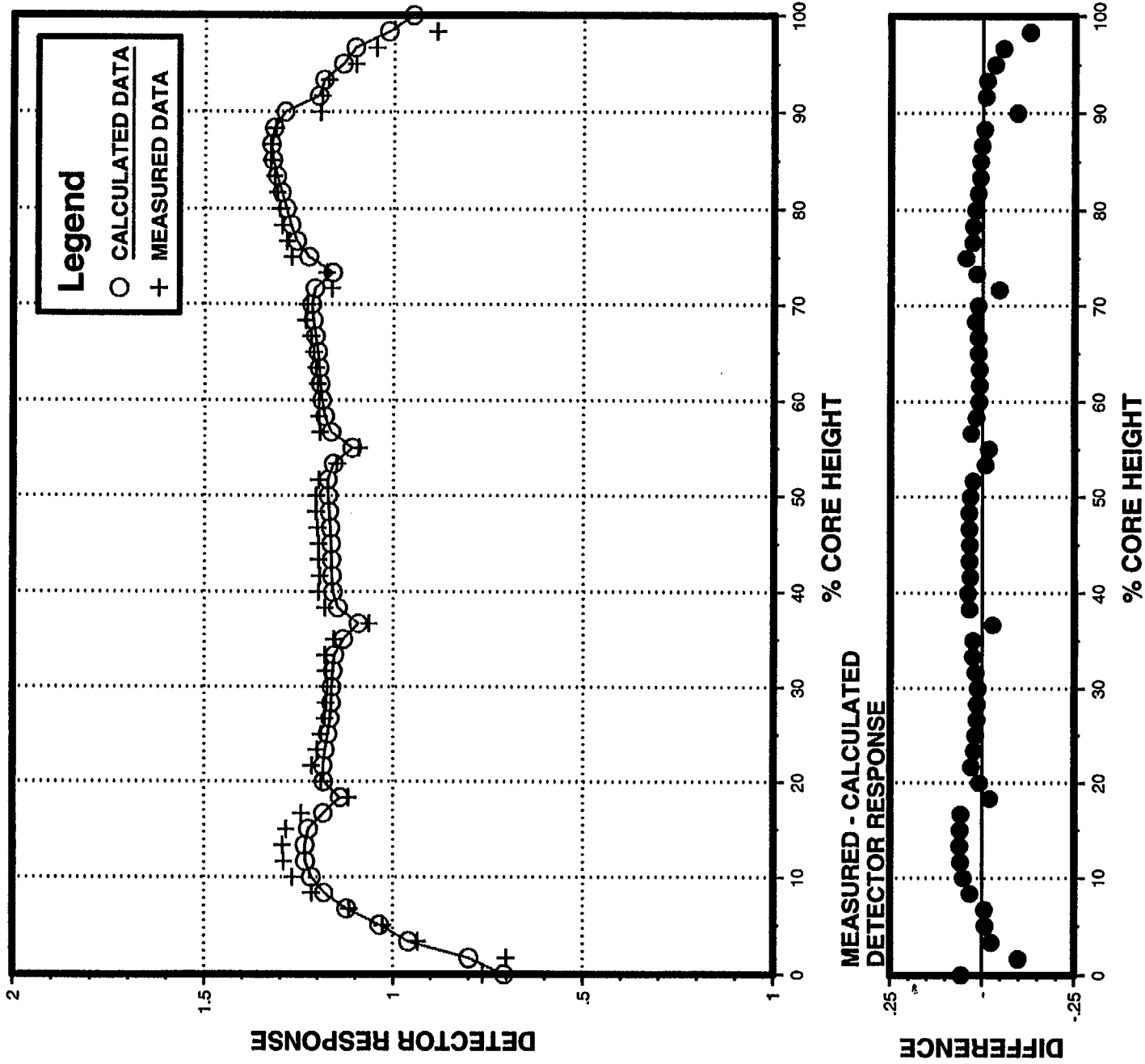


FIGURE 3.5.10

# PI Unit 1 Cycle 18 Measured versus Calculated Integrated Detector Response Differences

**Map 118-07, 1.303 GWd/MTU  
100% Power, ARO, EQ XENON (HFP Map)**

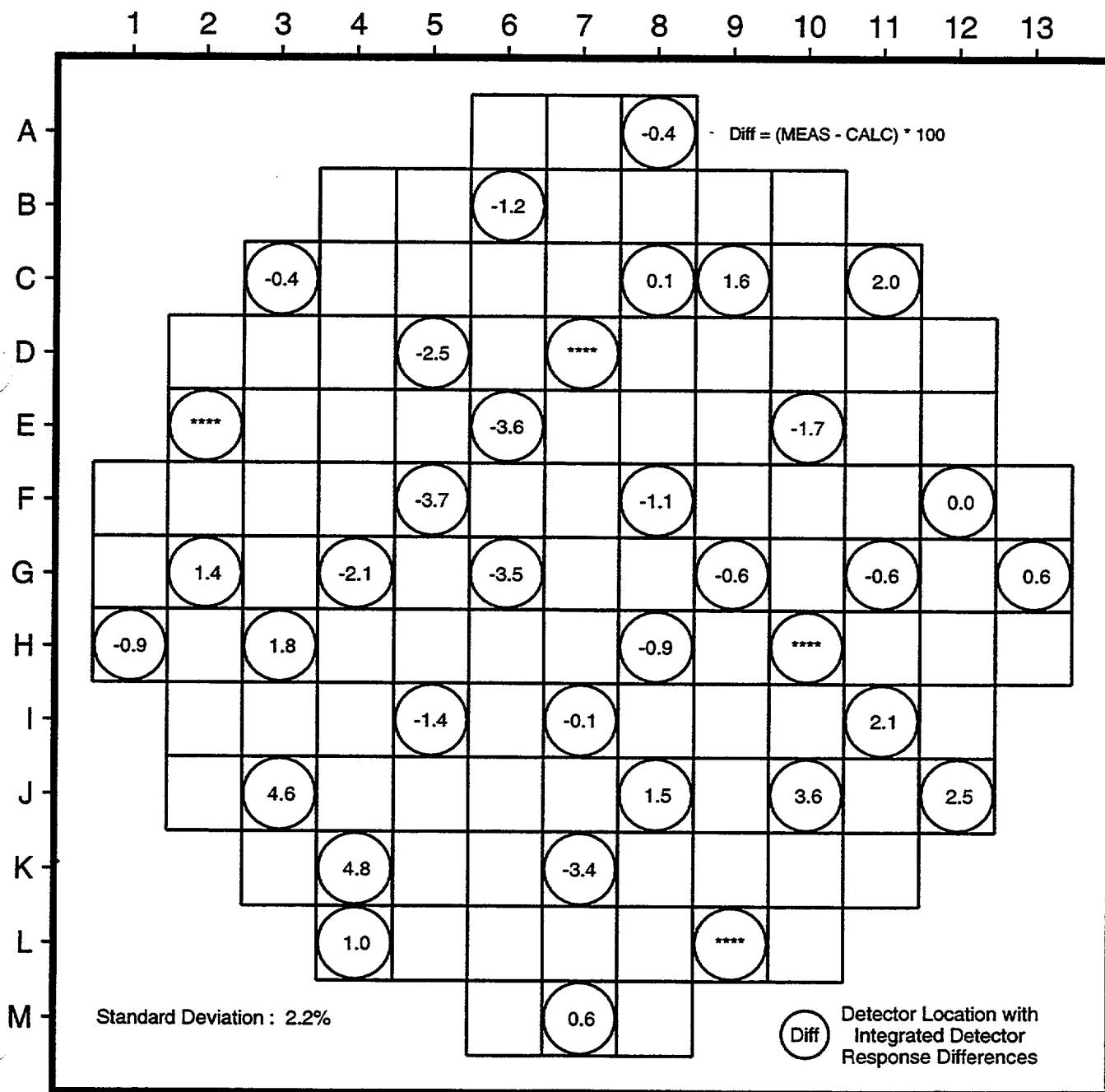


FIGURE 3.5.11

# PI Unit 1 Cycle 18 Measured versus Calculated Detector Response

Map 118-07, 1.303 GWD/MTU  
100% Power, ARO, EQ XENON (HFP Map)  
THIMBLE G-2  
Fresh 4.95 w/o U235, 8 pin 8 w/o Gd

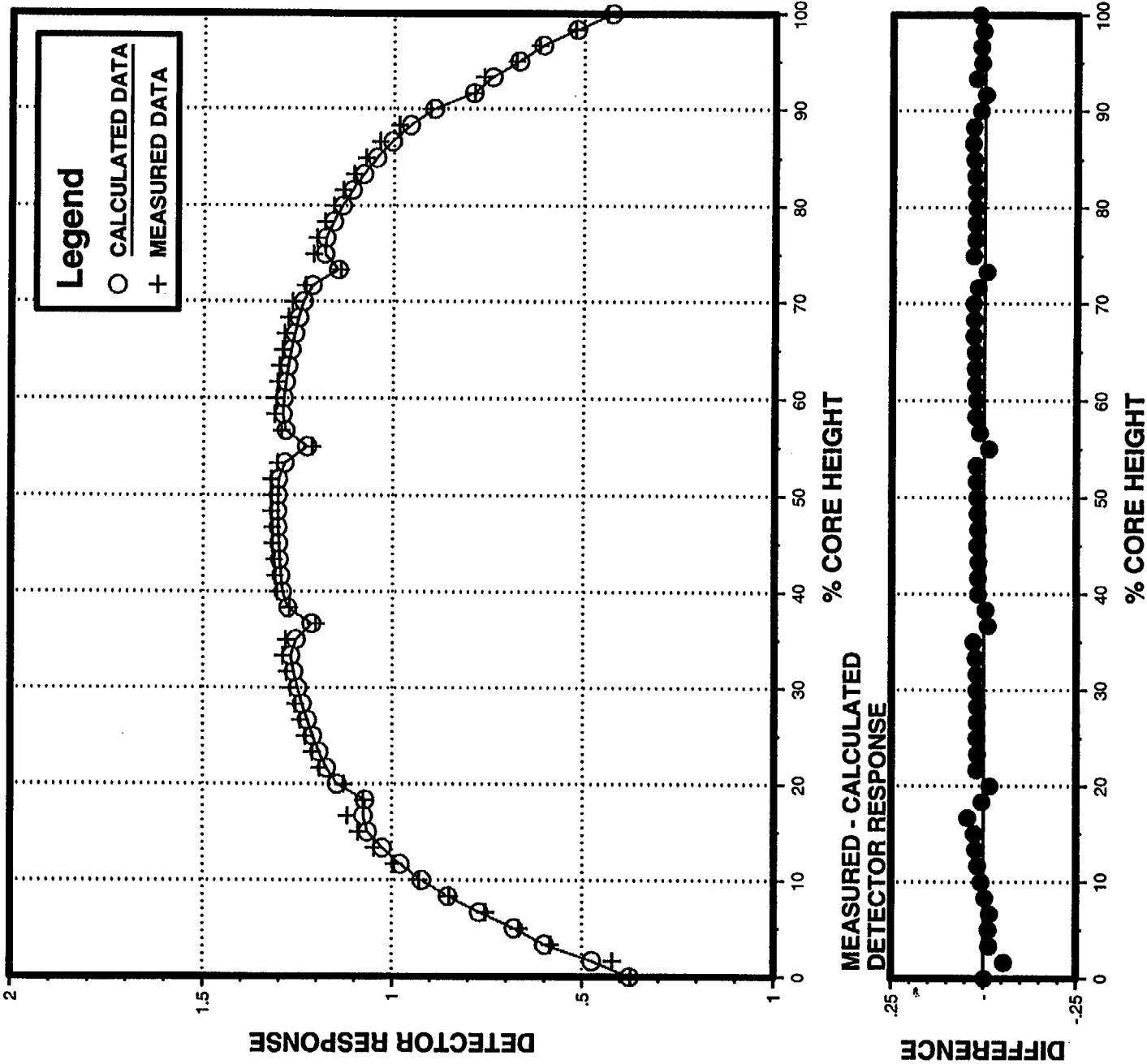


FIGURE 3.5.12

# PI Unit 1 Cycle 18 Measured versus Calculated Detector Response

Map 118-07, 1.303 GWD/MTU  
100% Power, ARO, EQ XENON (HFP Map)  
THIMBLE H-8  
Fresh 4.95 w/o U235, 12 pin 8 w/o Gd

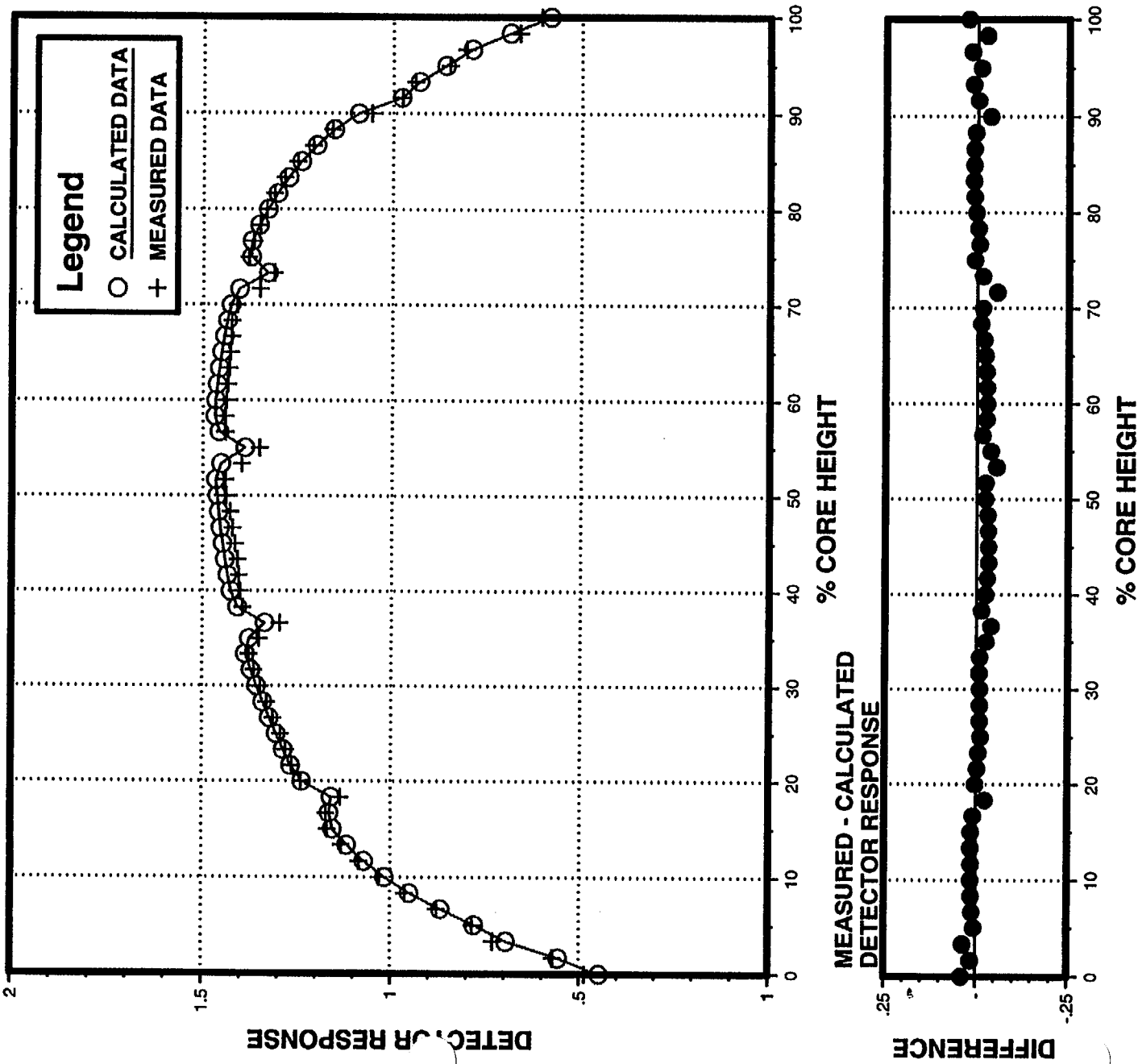




FIGURE 3.5.13

# PI Unit 1 Cycle 18 Measured versus Calculated Integrated Detector Response Differences

Map 118-16, 10.479 GWd/MTU  
100% Power, ARO, EQ XENON (HFP Map)

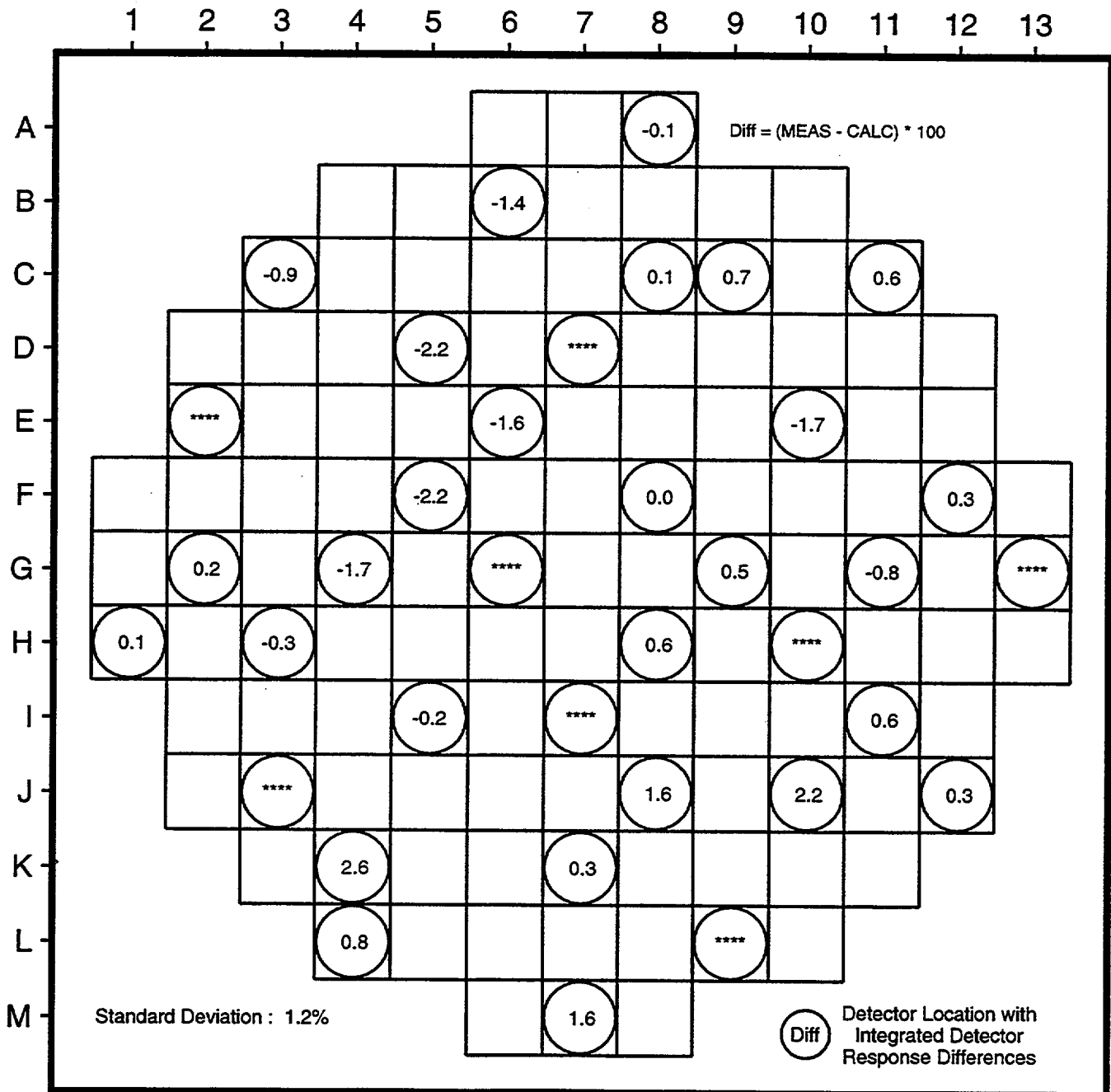


FIGURE 3.5.14

# PI Unit 1 Cycle 18 Measured versus Calculated Detector Response

Map 118-16, 10.479 GWd/MTU  
100% Power, ARO, EQ XENON (HFP Map)

THIMBLE G-2  
Fresh 4.95 w/o U235, 8 pin 8 w/o Gd

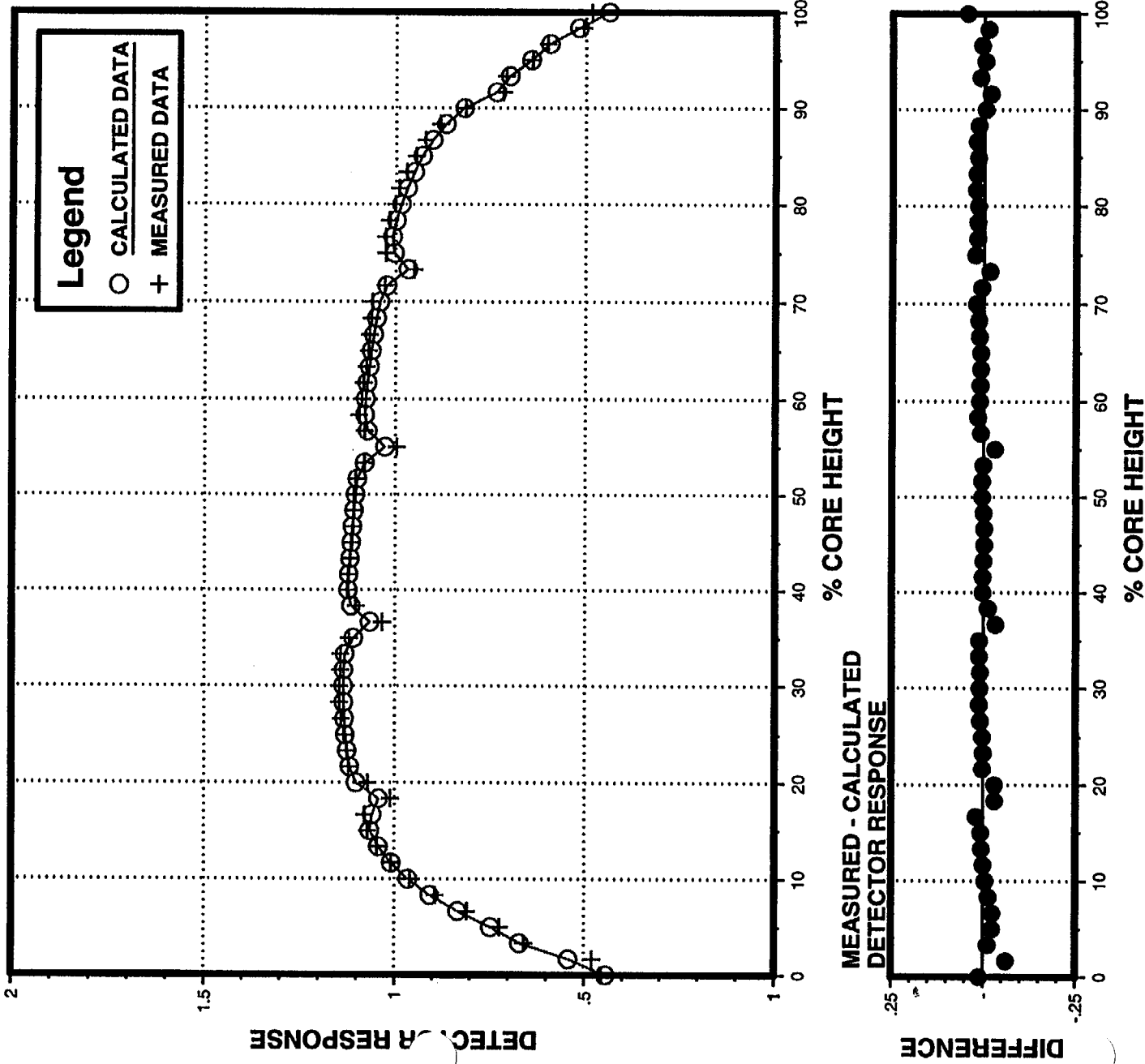


FIGURE 3.5.15

# PI Unit 1 Cycle 18 Measured versus Calculated Detector Response

Map 118-16, 10.479 GWd/MTU  
100% Power, ARO, EQ XENON (HFP Map)

THIMBLE H-8  
Fresh 4.95 w/o U235, 12 pin 8 w/o Gd

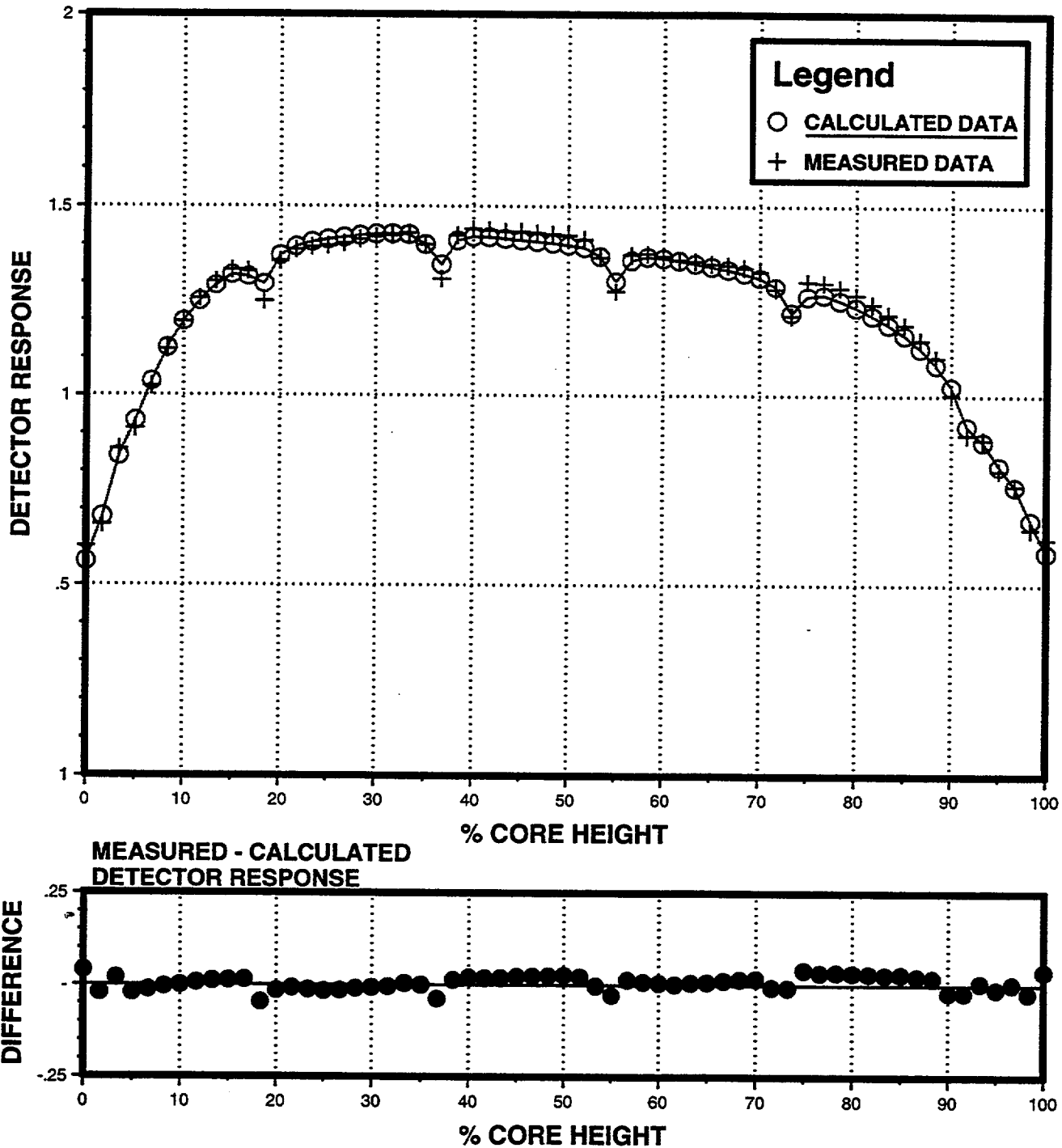


FIGURE 3.5.16

# PI Unit 1 Cycle 18 Measured versus Calculated Integrated Detector Response Differences

Map 118-29, 21.627 GWd/MTU  
90% Power, ARO, EQ XENON (Coast Map)

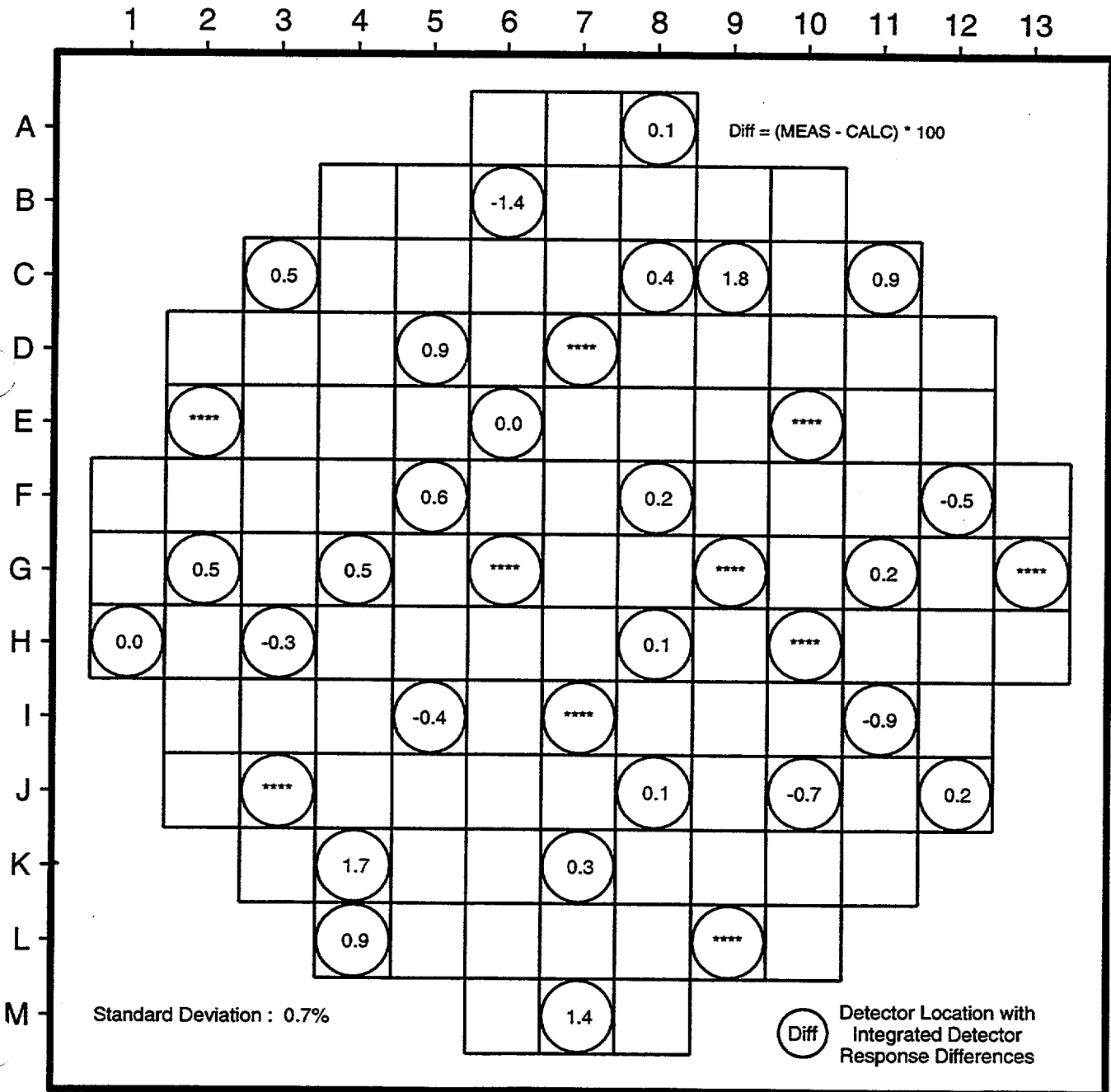


FIGURE 3.5.17

# PI Unit 1 Cycle 18 Measured versus Calculated Detector Response

Map 118-29, 21.627 GWd/MTU  
90% Power, ARO, EQ XENON (Coast Map)

THIMBLE G-2  
Fresh 4.95 w/o U235, 8 pin 8 w/o Gd

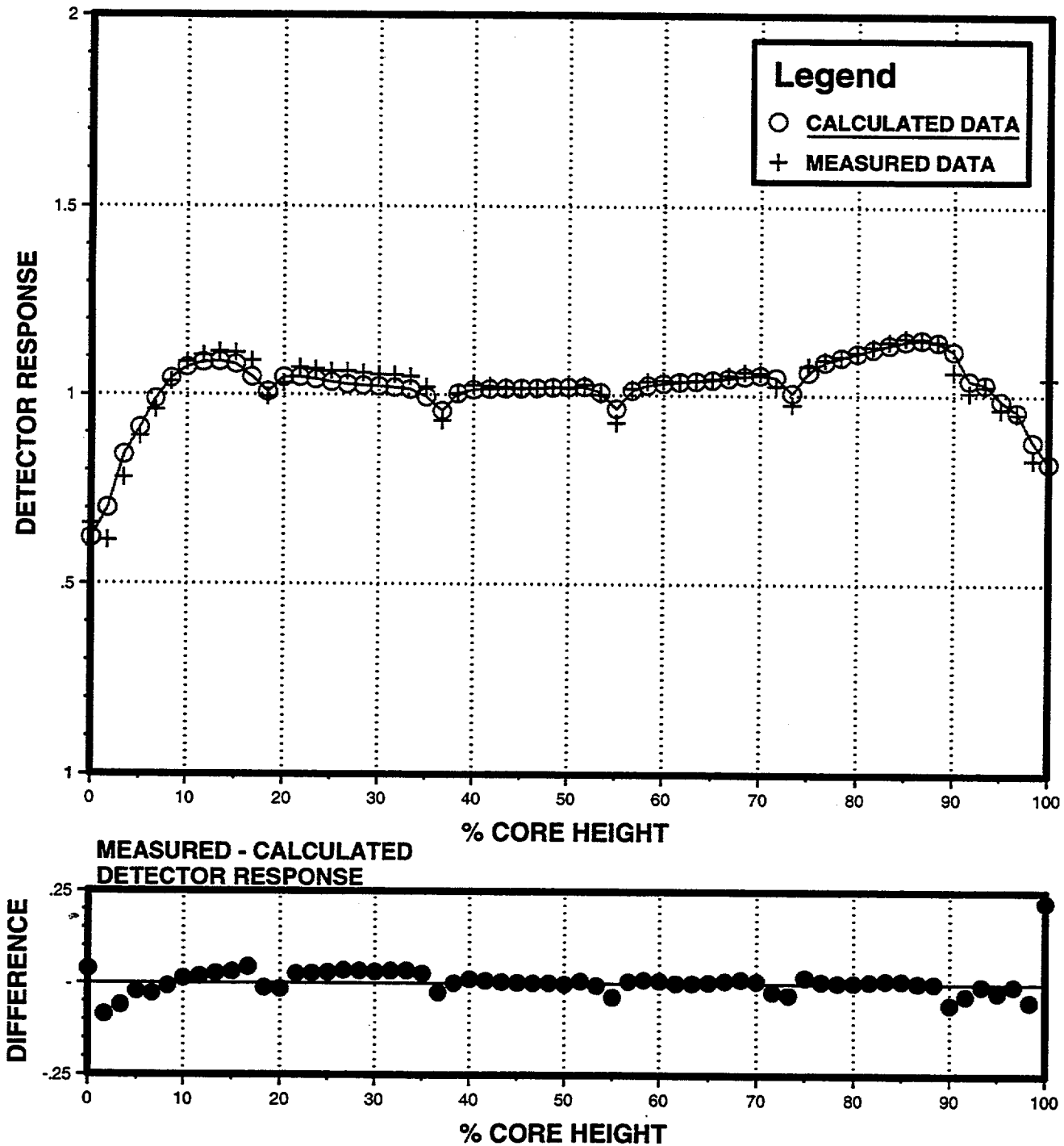


FIGURE 3.5.18

# PI Unit 1 Cycle 18 Measured versus Calculated Detector Response

Map 118-29, 21.627 GWd/MTU  
90% Power, ARO, EQ XENON (Coast Map)

THIMBLE H-8  
Fresh 4.95 w/o U235, 12 pin 8 w/o Gd

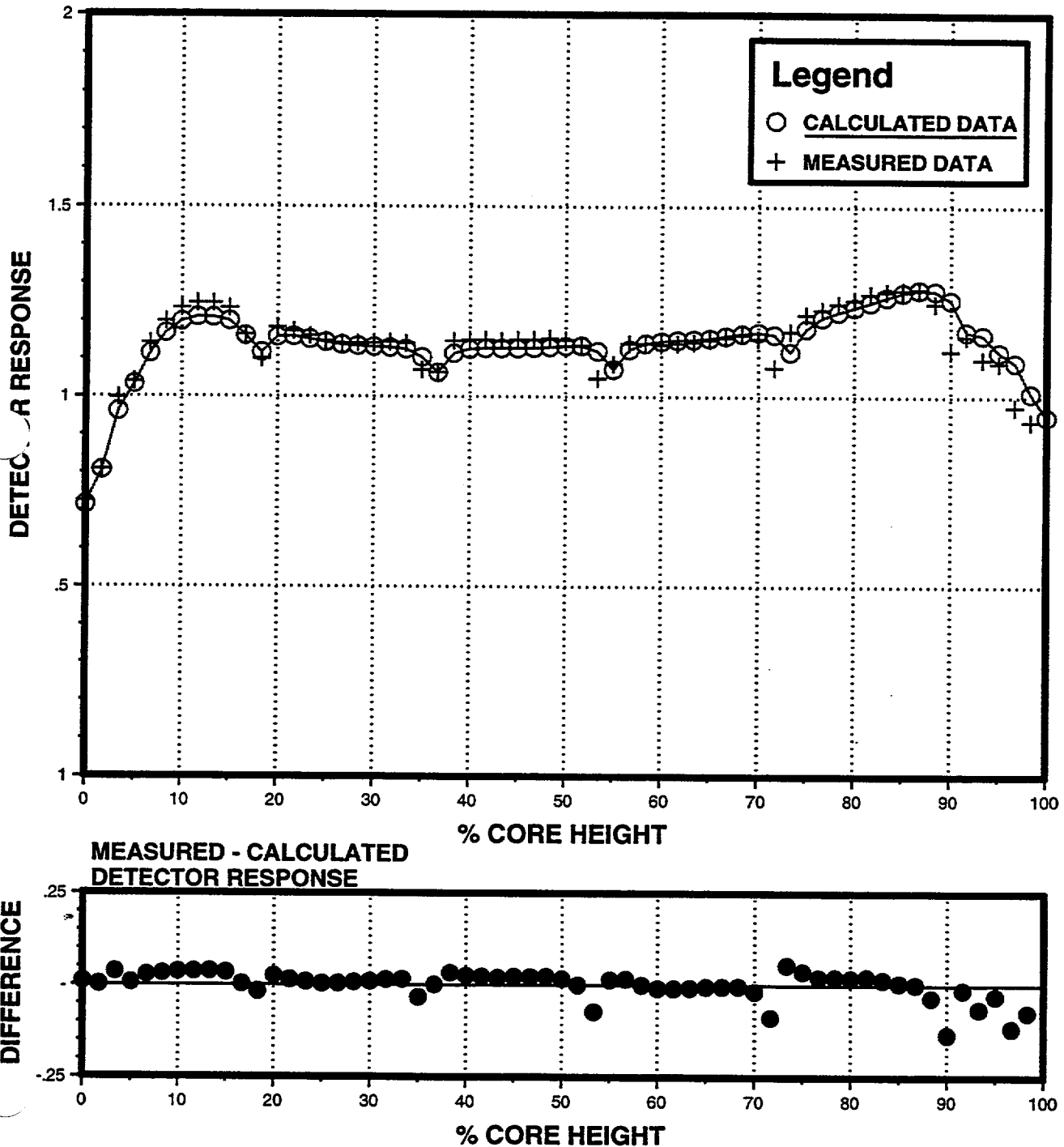


FIGURE 3.5.19

# PI Unit 2 Cycle 18 Measured versus Calculated Integrated Detector Response Differences

**Map 218-05, 0.237 GWd/MTU  
100% Power, ARO, EQ XENON (HFP Map)**

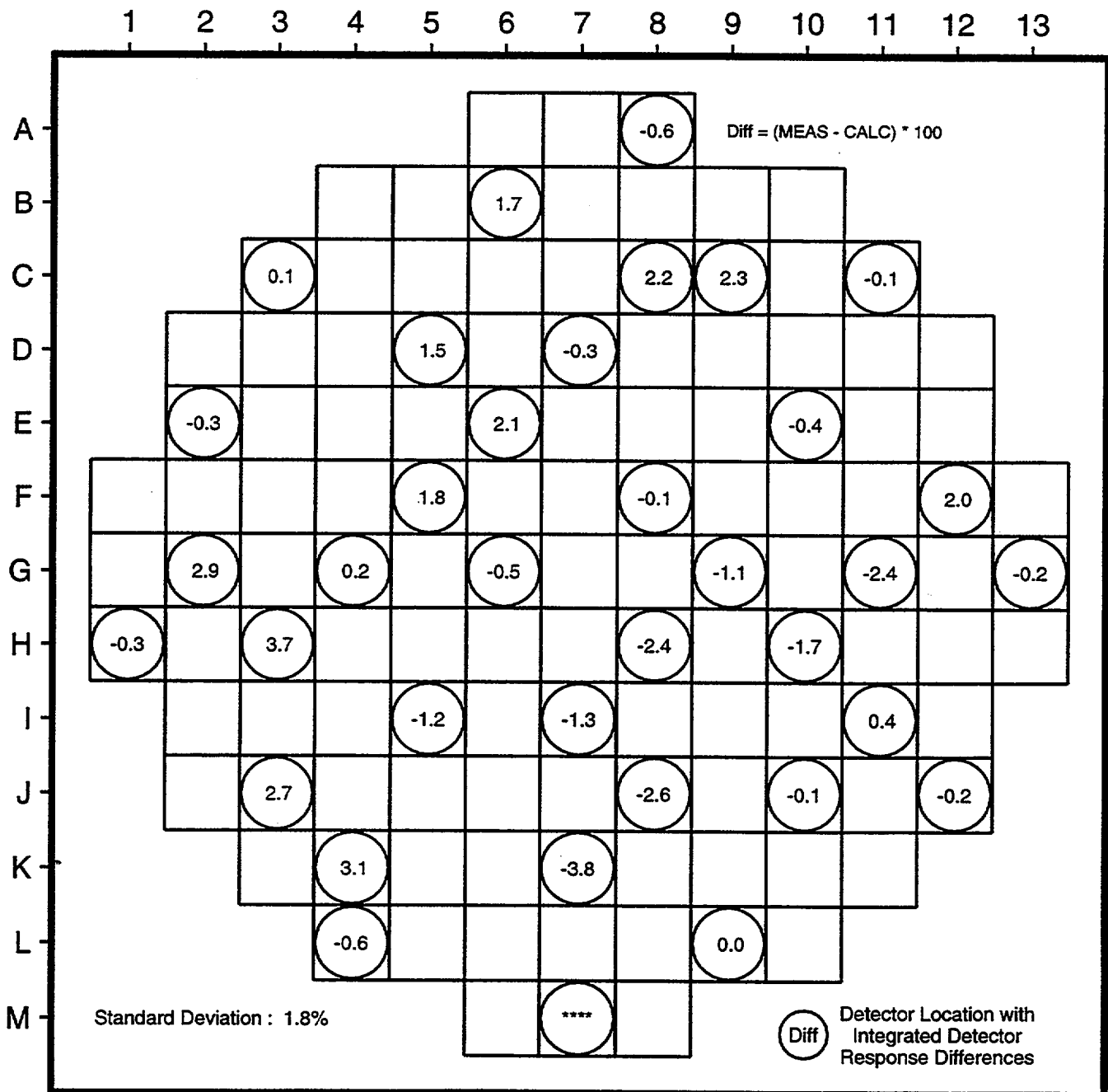


FIGURE 3.5.20

# PI Unit 2 Cycle 18 Measured versus Calculated Detector Response

Map 218-05, 0.237 GWd/MTU  
100% Power, ARO, EQ XENON (HFP Map)

THIMBLE J-3  
Fresh 4.95 w/o U235, 4 pin 8 w/o Gd

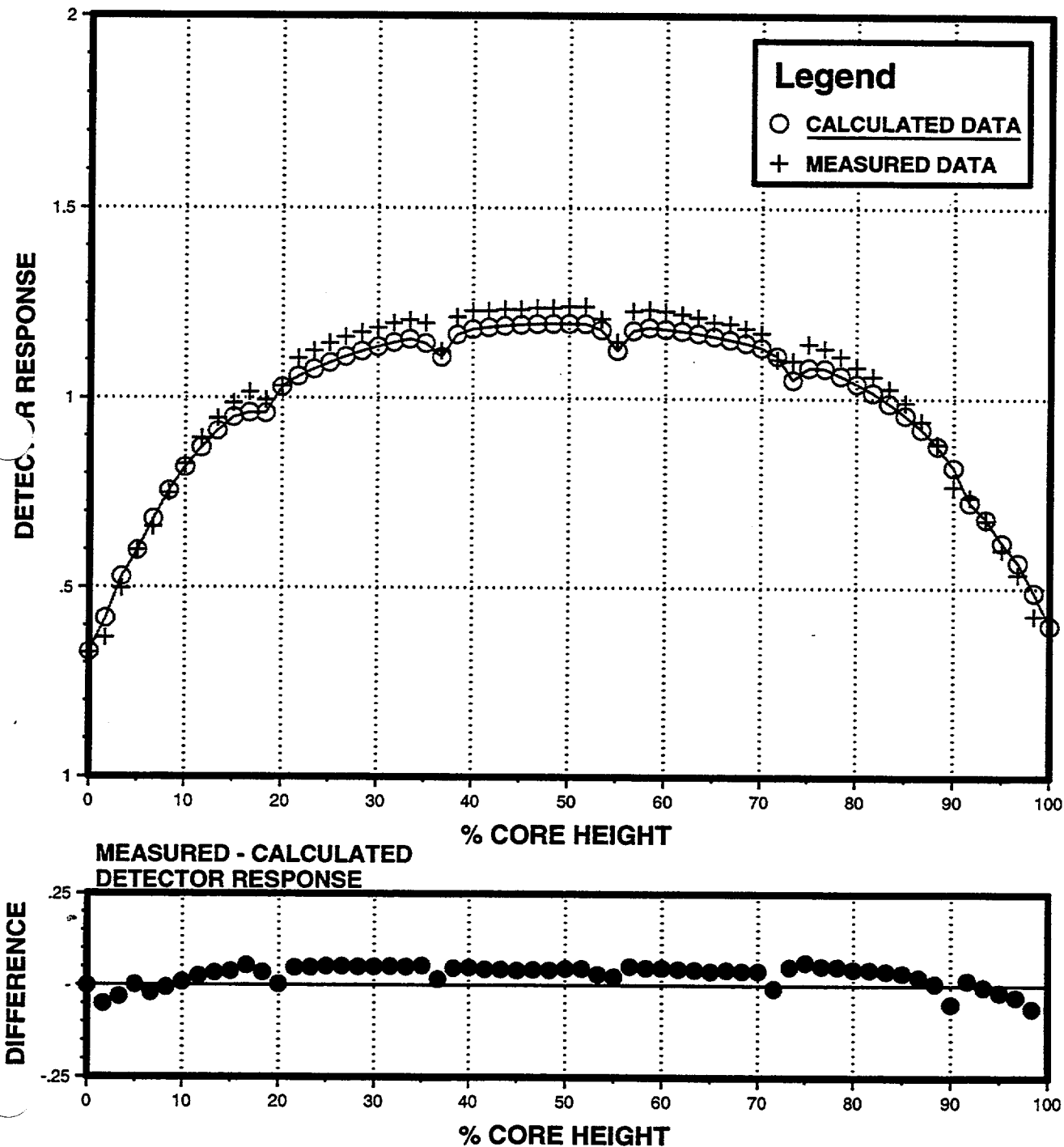




FIGURE 3.5.21

# PI Unit 2 Cycle 18 Measured versus Calculated Detector Response

Map 218-05, 0.237 GWd/MTU  
100% Power, ARO, EQ XENON (HFP Map)

THIMBLE H-10  
Fresh 4.95 w/o U235, 16 pin 8 w/o Gd

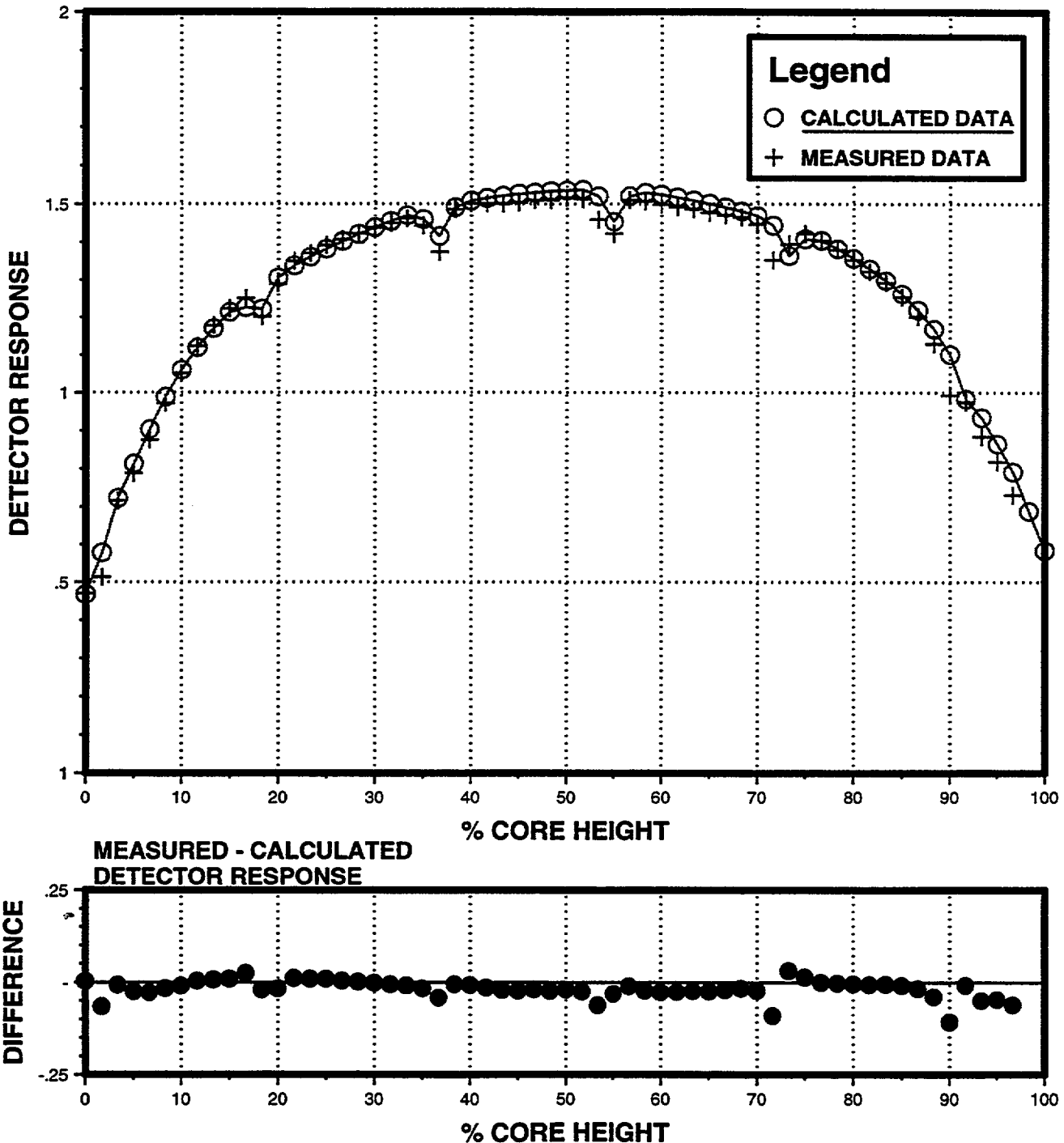


FIGURE 3.5.22

# PI Unit 2 Cycle 18 Measured versus Calculated Integrated Detector Response Differences

Map 218-18, 10.959 GWd/MTU  
100% Power, ARO, EQ XENON (HFP Map)

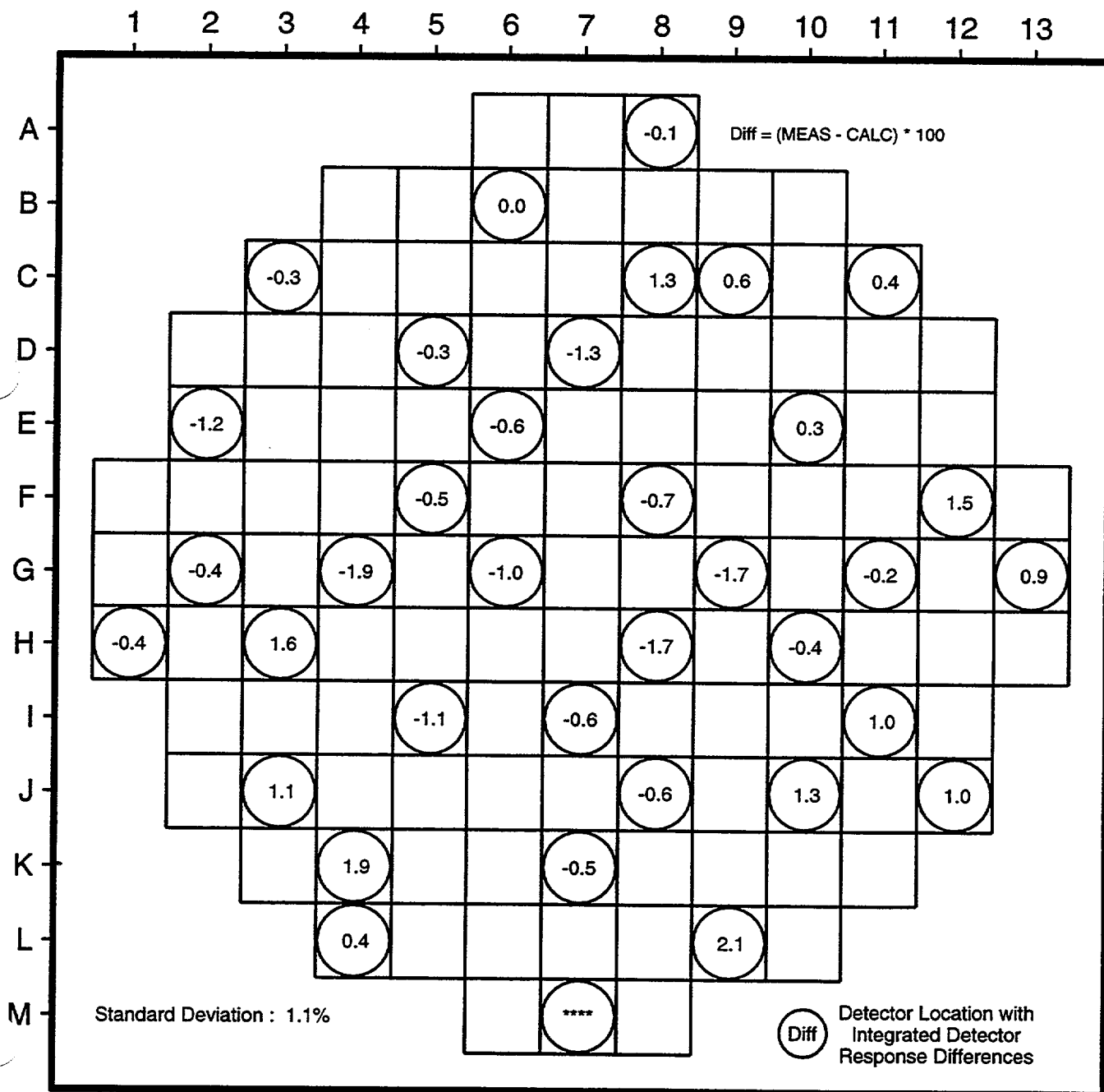


FIGURE 3.5.23

# PI Unit 2 Cycle 18 Measured versus Calculated Detector Response

Map 218-18, 10.959 GWd/MTU  
100% Power, ARO, EQ XENON (HFP Map)

THIMBLE J-3  
Fresh 4.95 w/o U235, 4 pin 8 w/o Gd

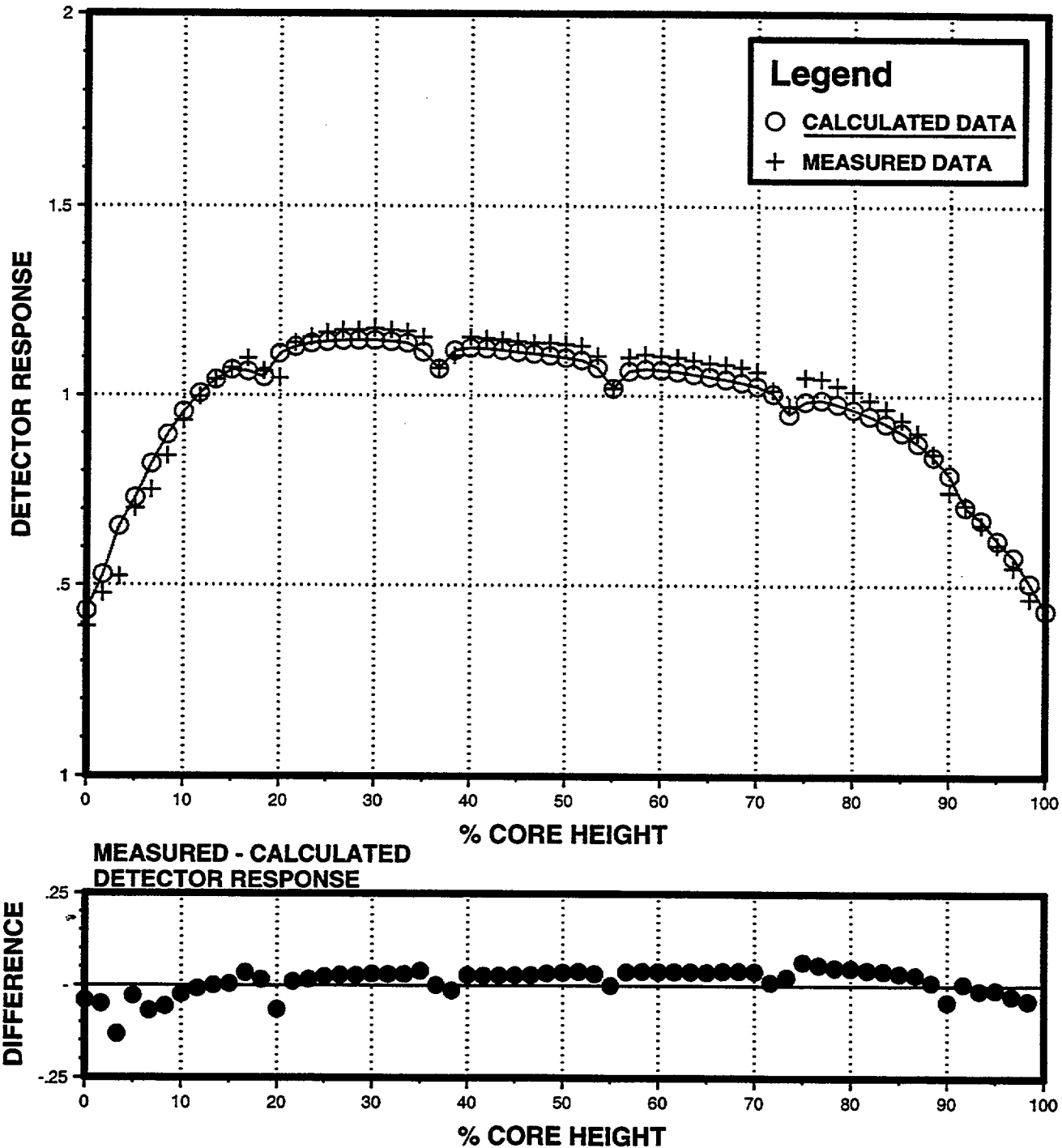


FIGURE 3.5.24

# PI Unit 2 Cycle 18 Measured versus Calculated Detector Response

Map 218-18, 10.959 GWd/MTU  
100% Power, ARO, EQ XENON (HFP Map)

THIMBLE H-10  
Fresh 4.95 w/o U235, 16 pin 8 w/o Gd

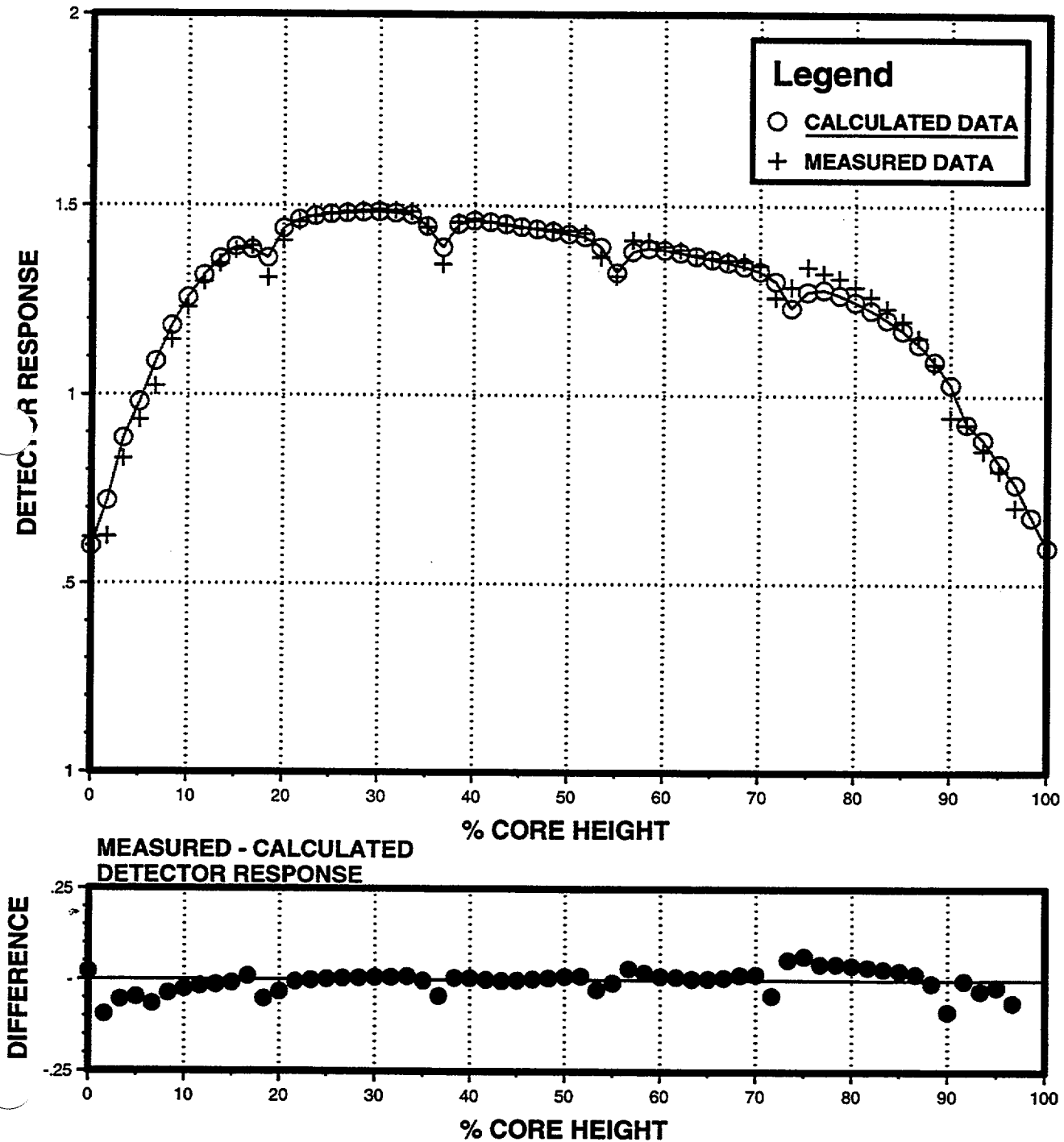


FIGURE 3.5.25

# PI Unit 2 Cycle 18 Measured versus Calculated Integrated Detector Response Differences

**Map 218-27, 19.536 GWd/MTU  
100% Power, ARO, EQ XENON (HFP Map)**

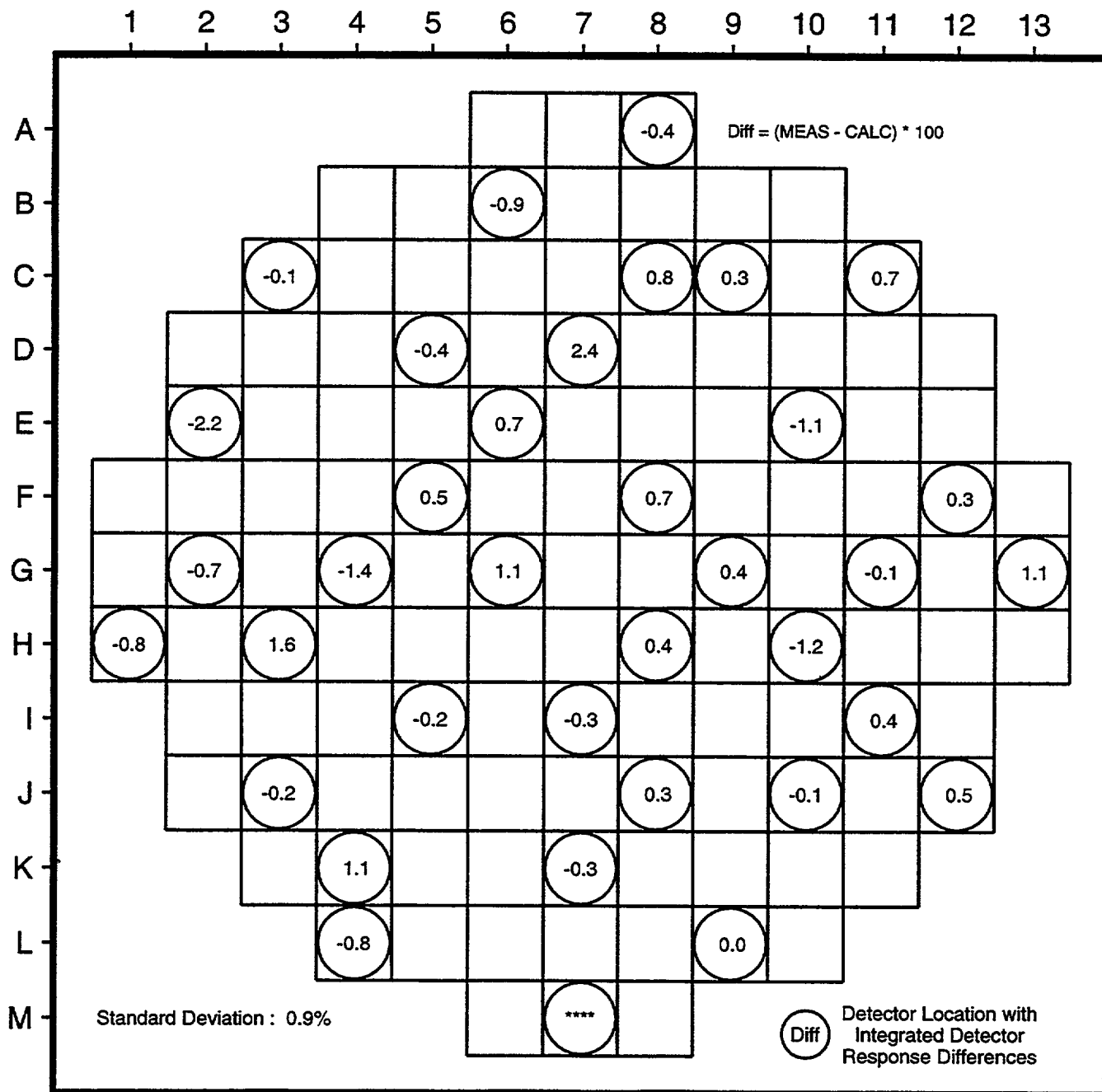


FIGURE 3.5.26

# PI Unit 2 Cycle 18 Measured versus Calculated Detector Response

Map 218-27, 19.536 GWd/MTU  
100% Power, ARO, EQ XENON (HFP Map)

THIMBLE J-3  
Fresh 4.95 w/o U235, 4 pin 8 w/o Gd

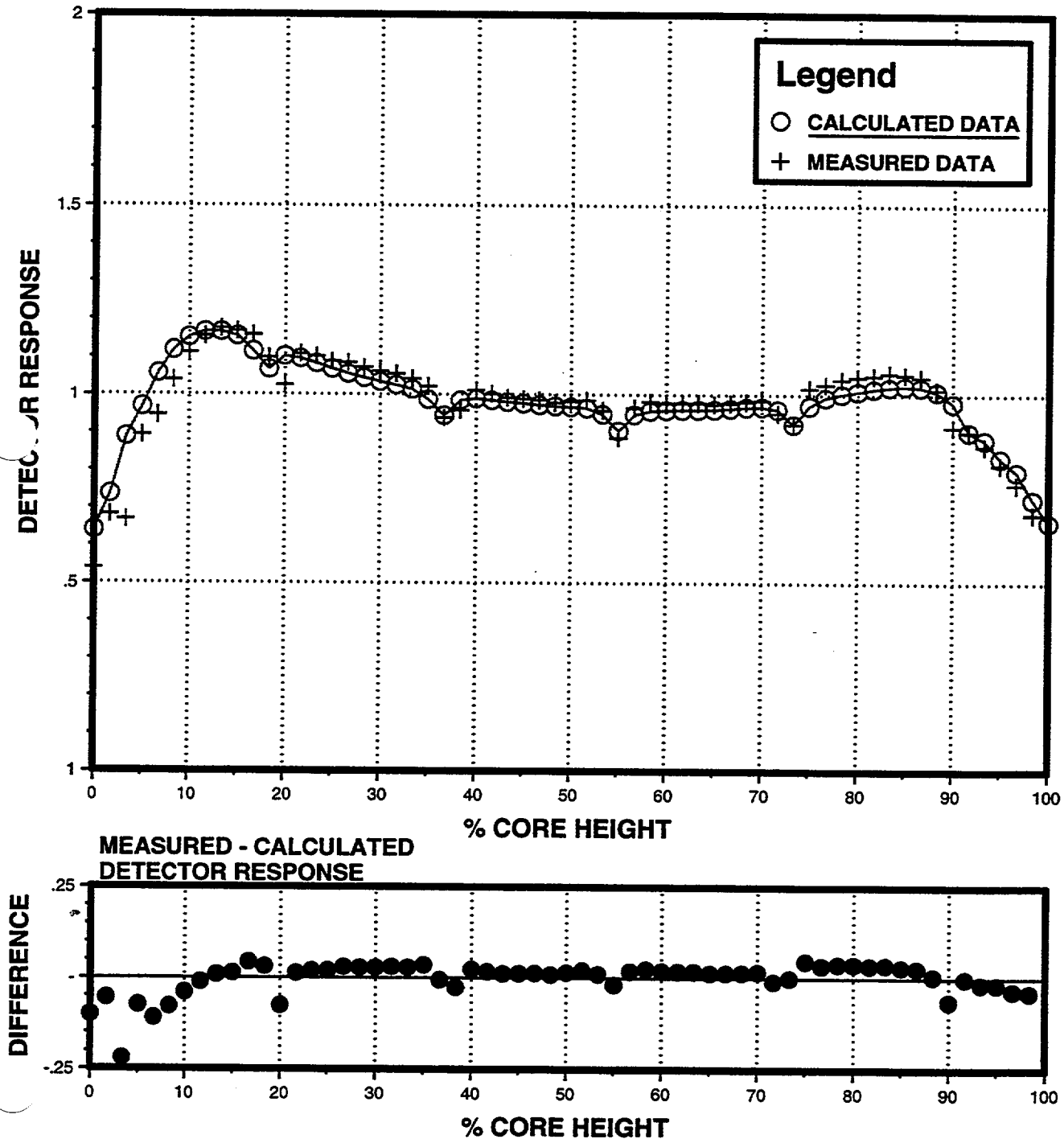


FIGURE 3.5.27

# PI Unit 2 Cycle 18 Measured versus Calculated Detector Response

Map 218-27, 19.536 GWd/MTU  
100% Power, ARO, EQ XENON (HFP Map)

THIMBLE H-10  
Fresh 4.95 w/o U235, 16 pin 8 w/o Gd

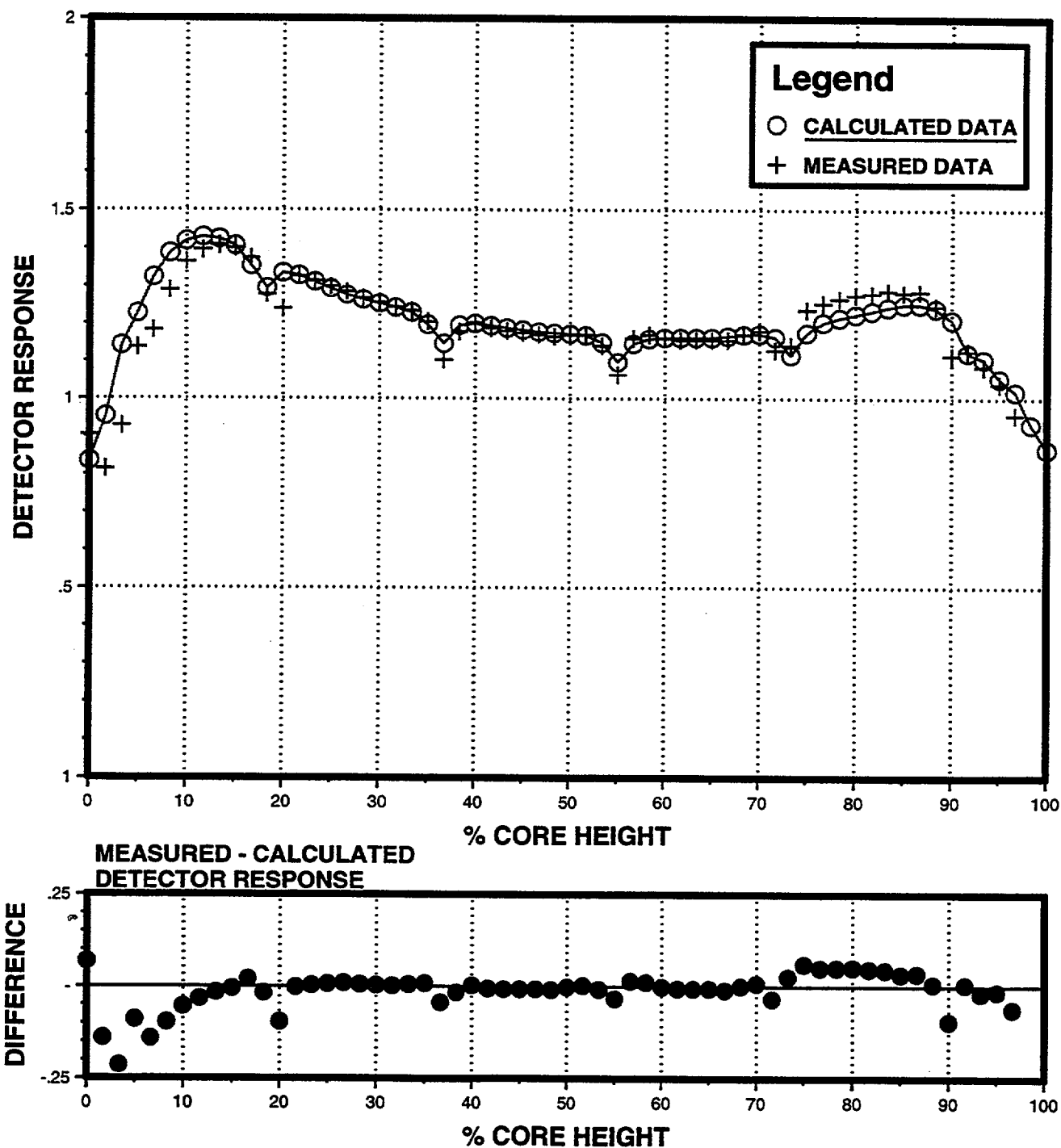


FIGURE 3.5.28

# PI Unit 1 Cycle 19 Measured versus Calculated Integrated Detector Response Differences

Map 119-06, 1.223 GWd/MTU  
100% Power, ARO, EQ XENON (HFP Map)

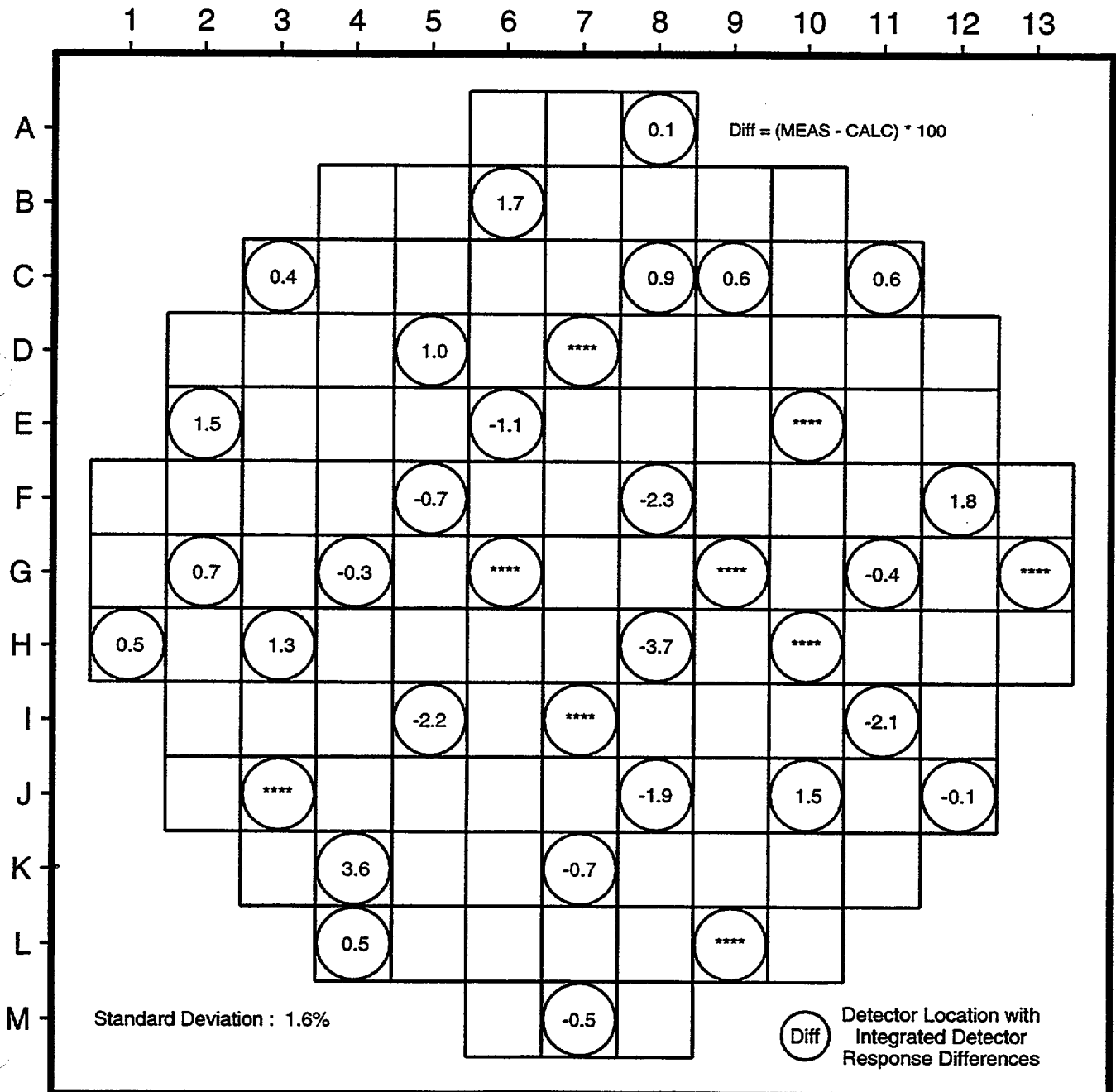




FIGURE 3.5.29

# PI Unit 1 Cycle 19 Measured versus Calculated Detector Response

Map 119-06, 1.223 GWd/MTU  
100% Power, ARO, EQ XENON (HFP Map)

THIMBLE E-2  
Fresh 4.95 w/o U235, No Gd

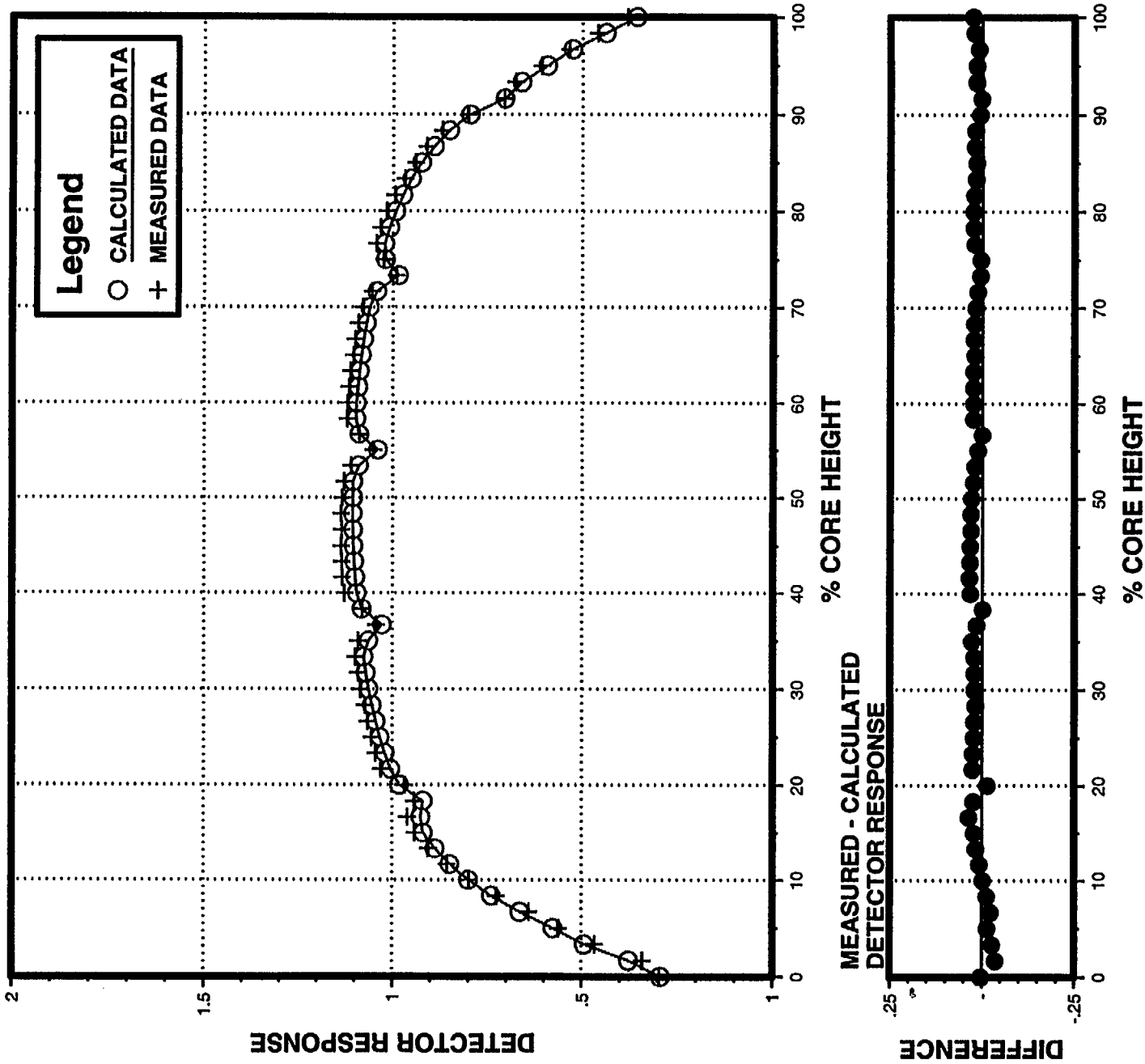


FIGURE 3.5.30

# PI Unit 1 Cycle 19 Measured versus Calculated Detector Response

Map 119-06, 1.223 GWd/MTU  
100% Power, ARO, EQ XENON (HFP Map)

THIMBLE F-8  
Fresh 4.95 w/o U235, 16 pin 8 w/o Gd

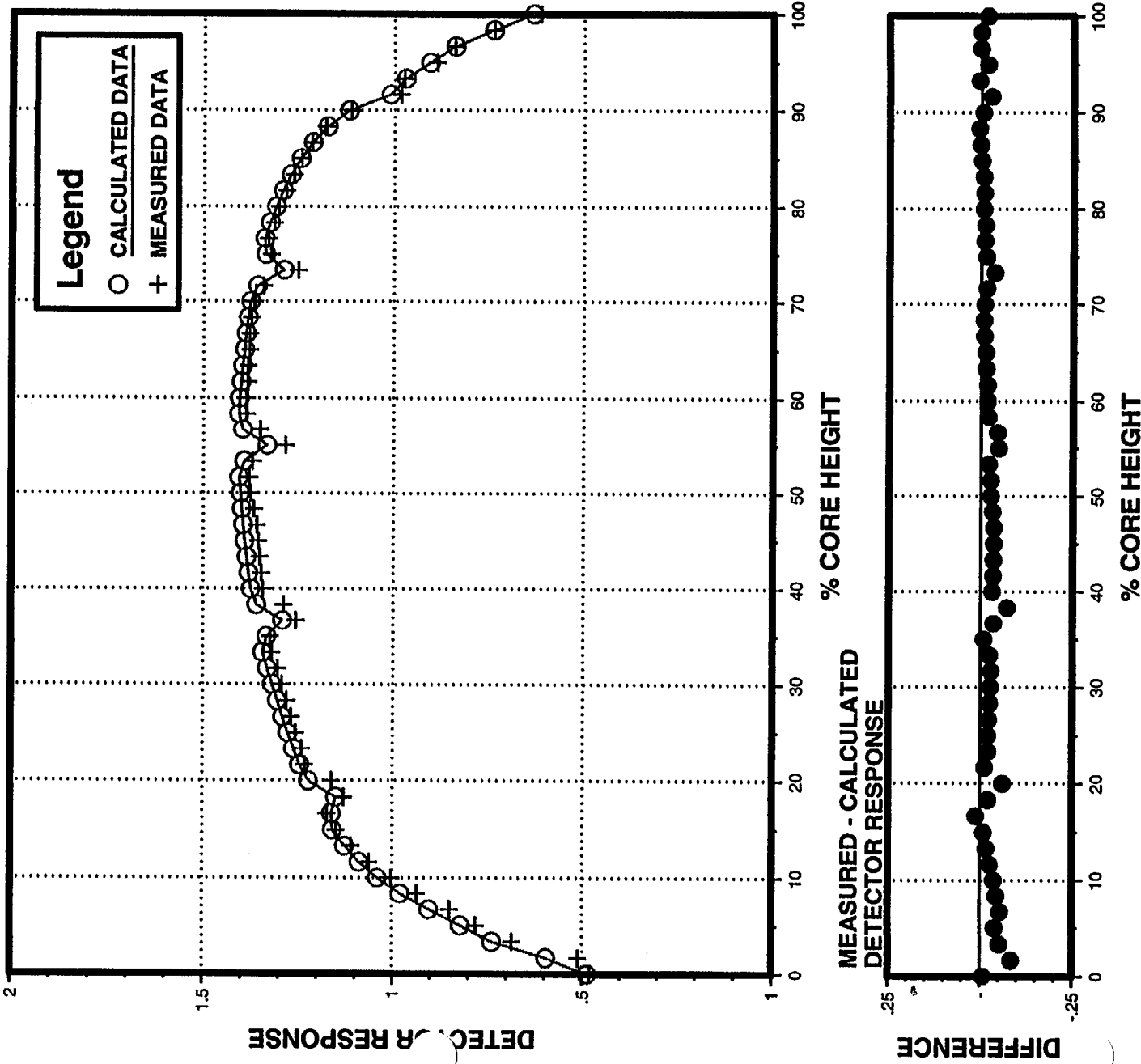


FIGURE 3.5.31

# PI Unit 1 Cycle 19 Measured versus Calculated Integrated Detector Response Differences

Map 119-15, 11.122 GWd/MTU  
100% Power, ARO, EQ XENON (HFP Map)

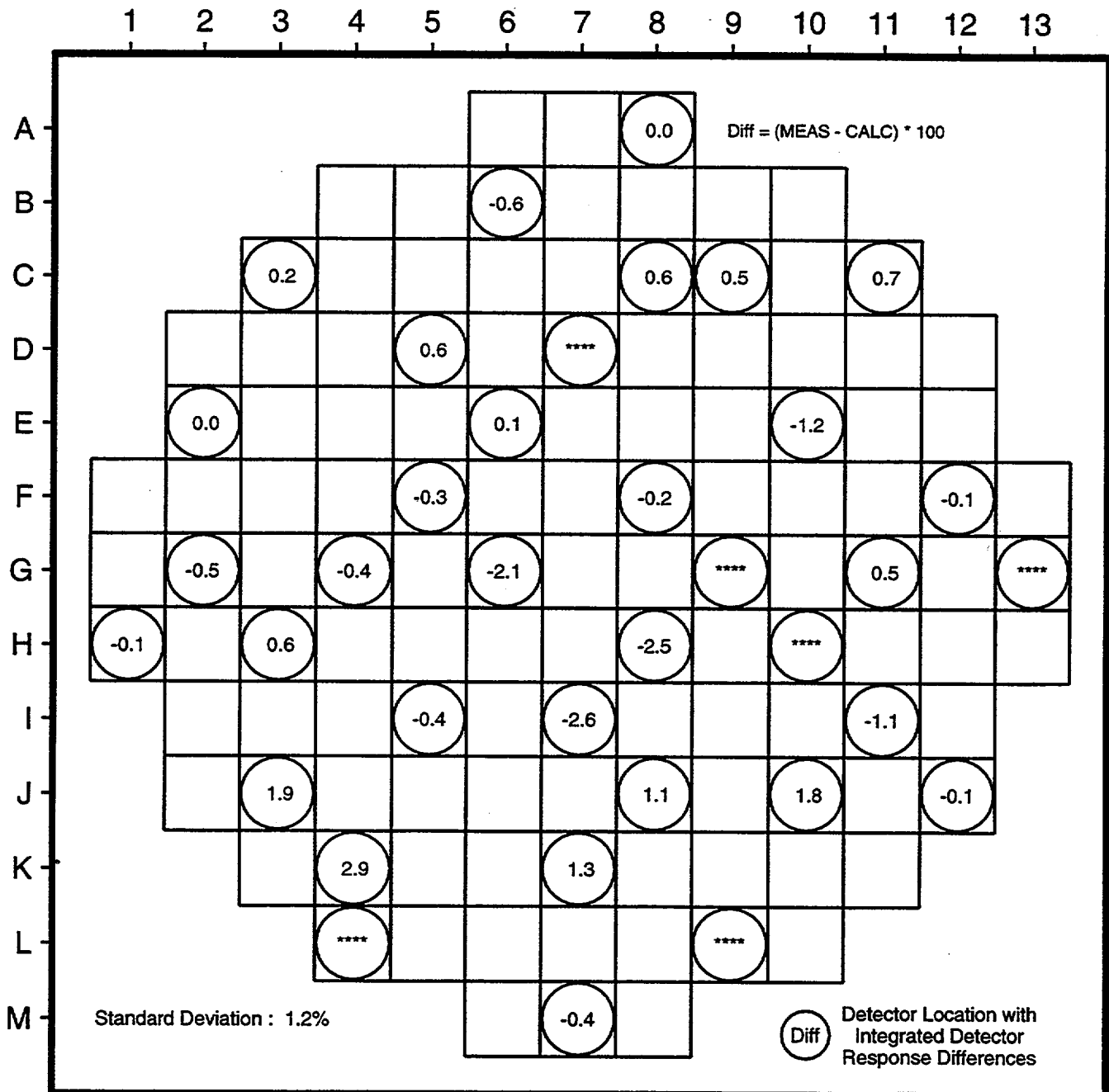


FIGURE 3.5.32

# PI Unit 1 Cycle 19 Measured versus Calculated Detector Response

Map 119-15, 11.122 GWd/MTU  
100% Power, ARO, EQ XENON (HFP Map)

THIMBLE E-2  
Fresh 4.95 w/o U235, No Gd

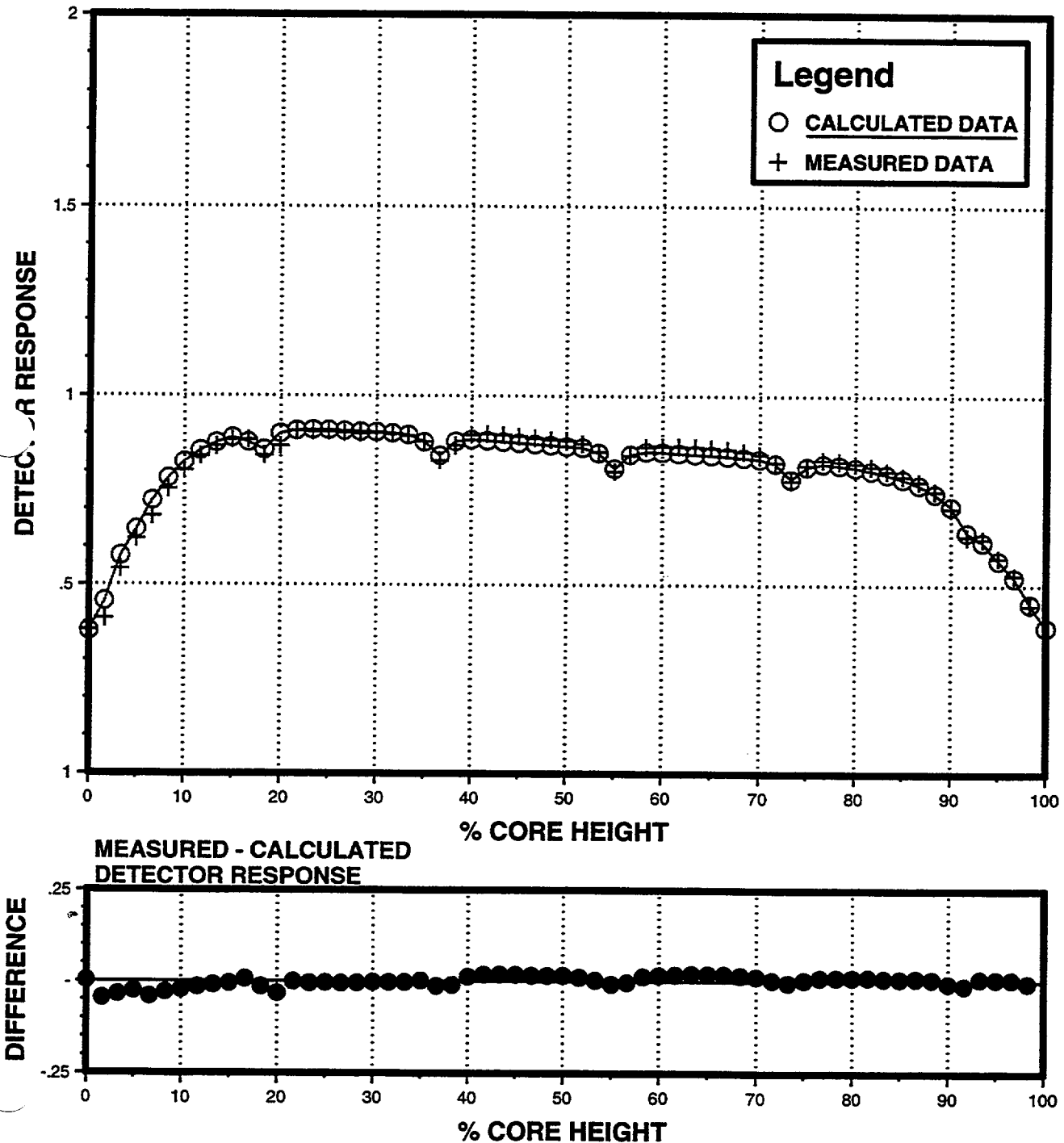


FIGURE 3.5.33

# PI Unit 1 Cycle 19 Measured versus Calculated Detector Response

Map 119-15, 11.122 GWd/MTU  
100% Power, ARO, EQ XENON (HFP Map)

THIMBLE F-8  
Fresh 4.95 w/o U235, 16 pin 8 w/o Gd

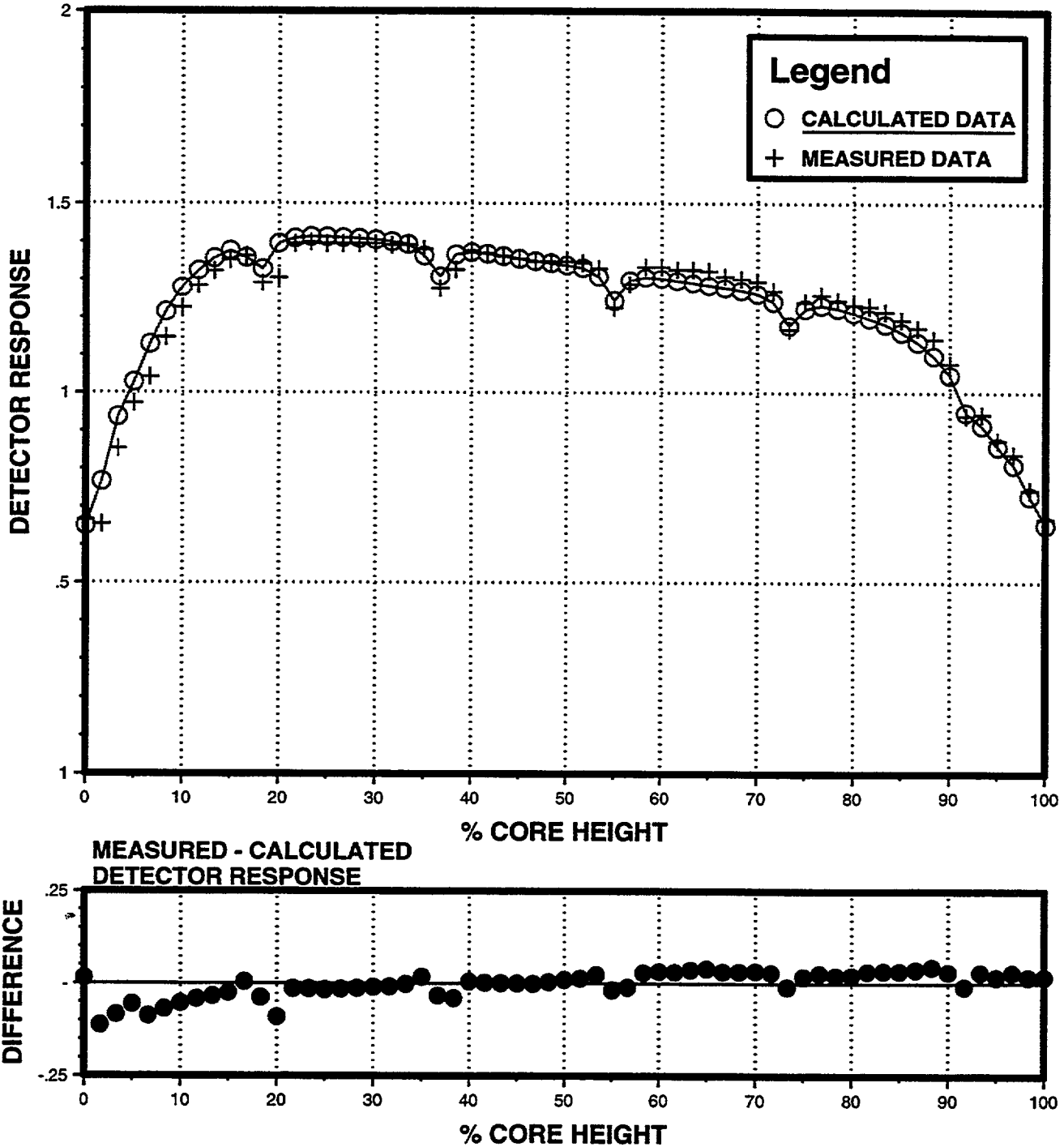


FIGURE 3.5.34

# PI Unit 1 Cycle 19 Measured versus Calculated Integrated Detector Response Differences

Map 119-20, 15.990 GWd/MTU  
100% Power, ARO, EQ XENON (HFP Map)

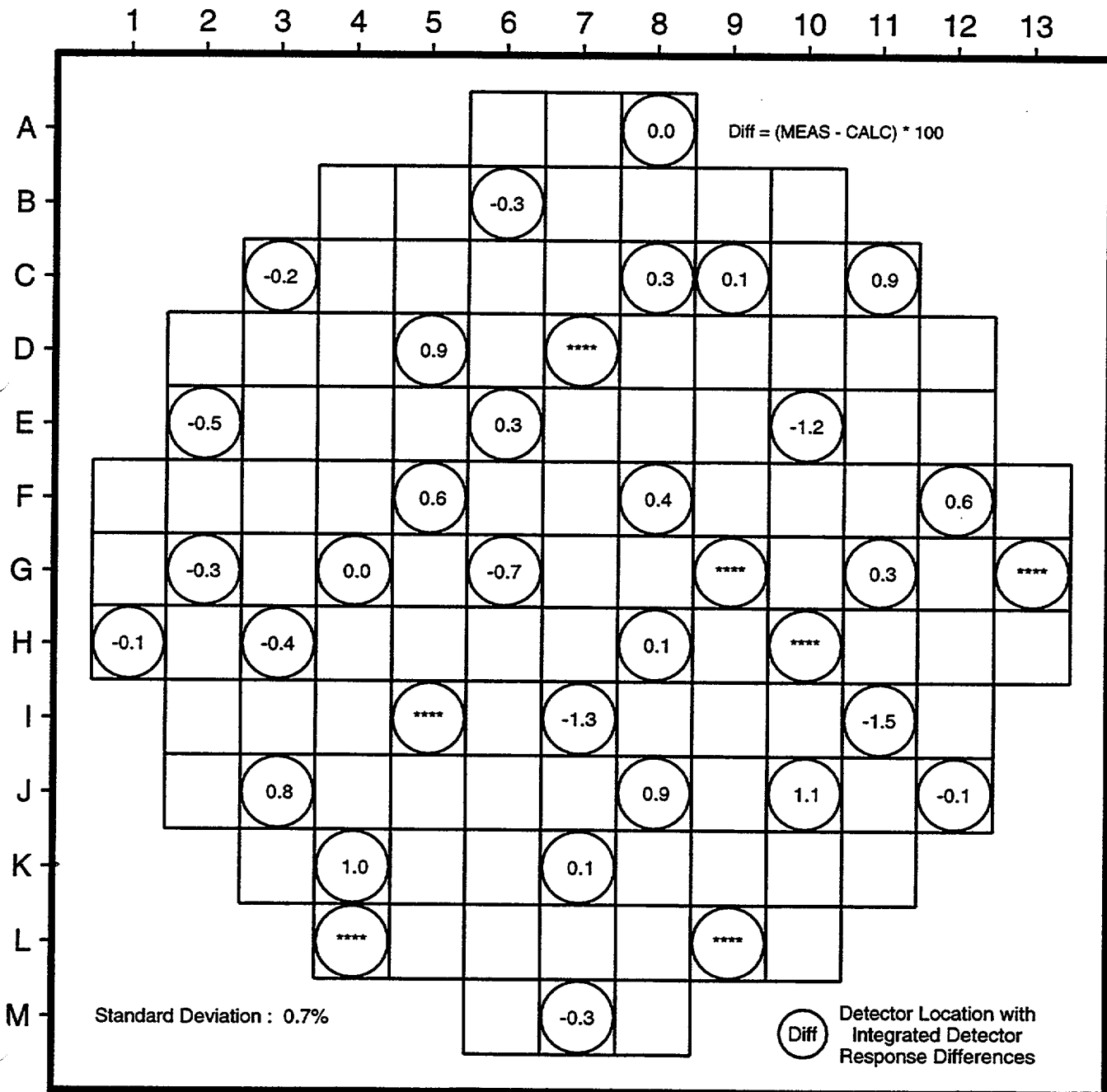


FIGURE 3.5.35

# PI Unit 1 Cycle 19 Measured versus Calculated Detector Response

Map 119-20, 15.990 GWd/MTU  
100% Power, ARO, EQ XENON (HFP Map)

THIMBLE E-2  
Fresh 4.95 w/o U235, No Gd

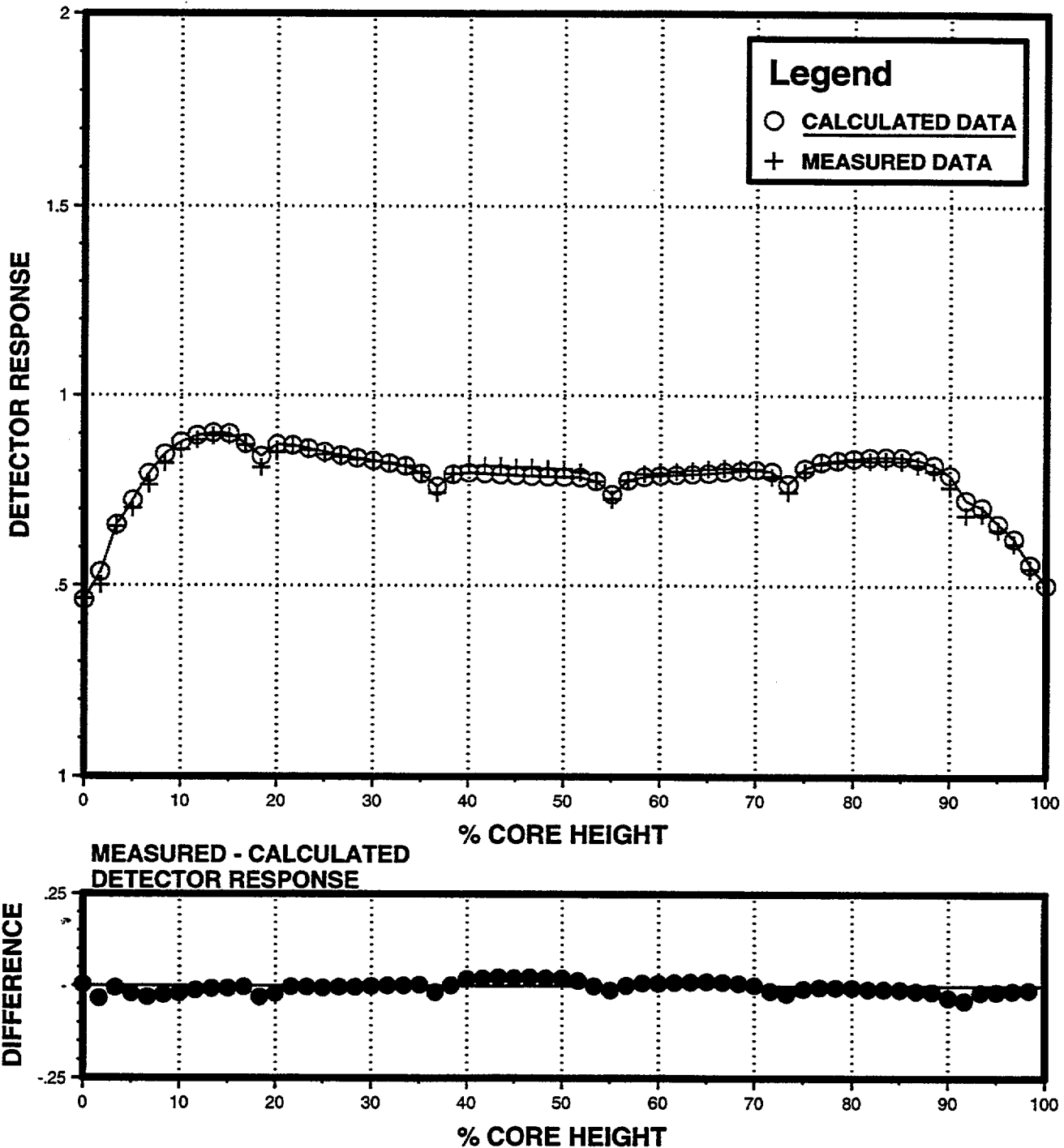


FIGURE 3.5.36

# PI Unit 1 Cycle 19 Measured versus Calculated Detector Response

Map 119-20, 15.990 GWd/MTU  
100% Power, ARO, EQ XENON (HFP Map)  
THIMBLE F-8  
Fresh 4.95 w/o U235, 16 pin 8 w/o Gd

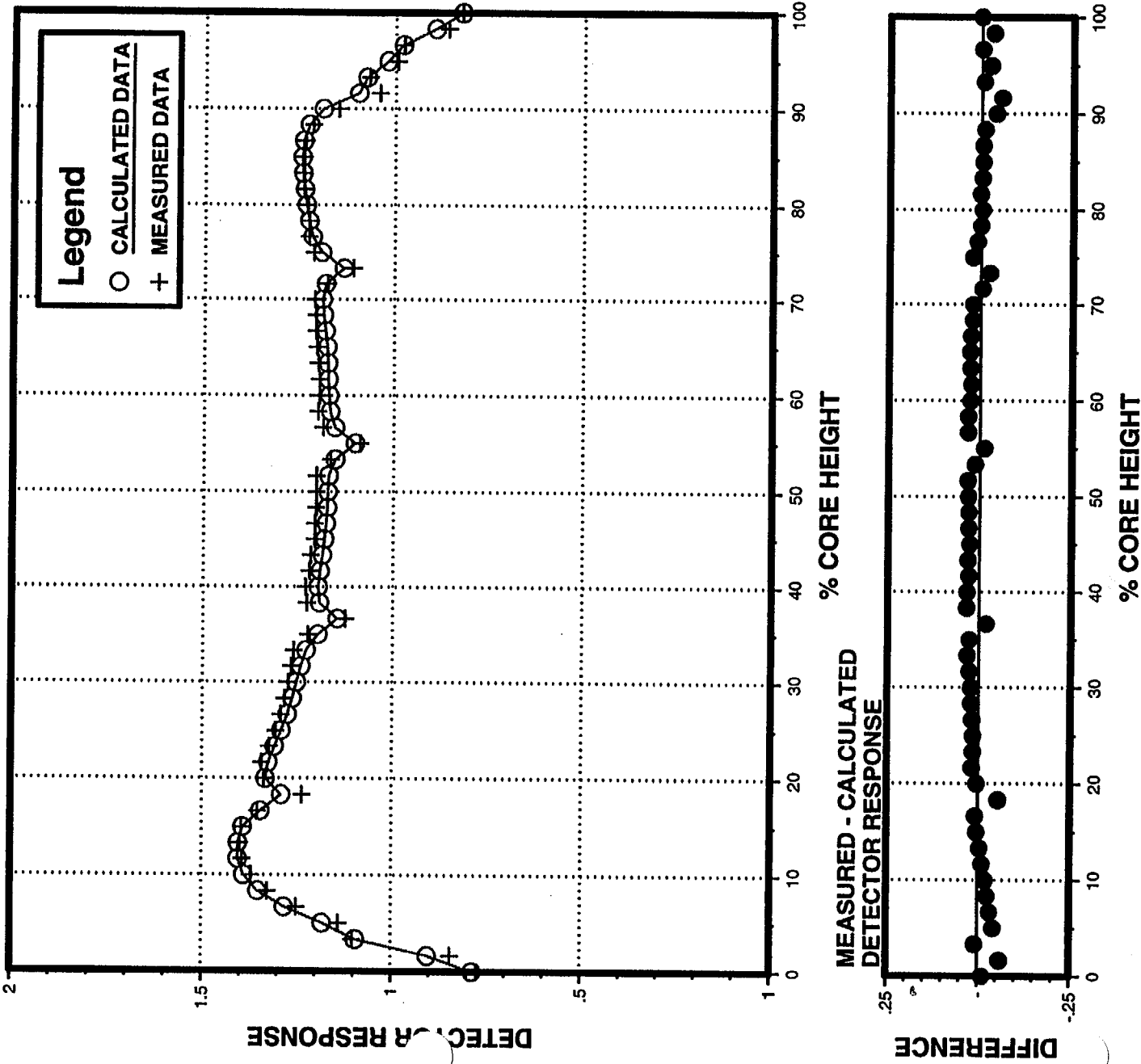




FIGURE 3.5.37

# PI Cycles - P217,P118,P218,P119

$F_Q$  Reliability Factor + Bias vs. Measured Reaction Rate

CASMO-4/SIMULATE-3 Model

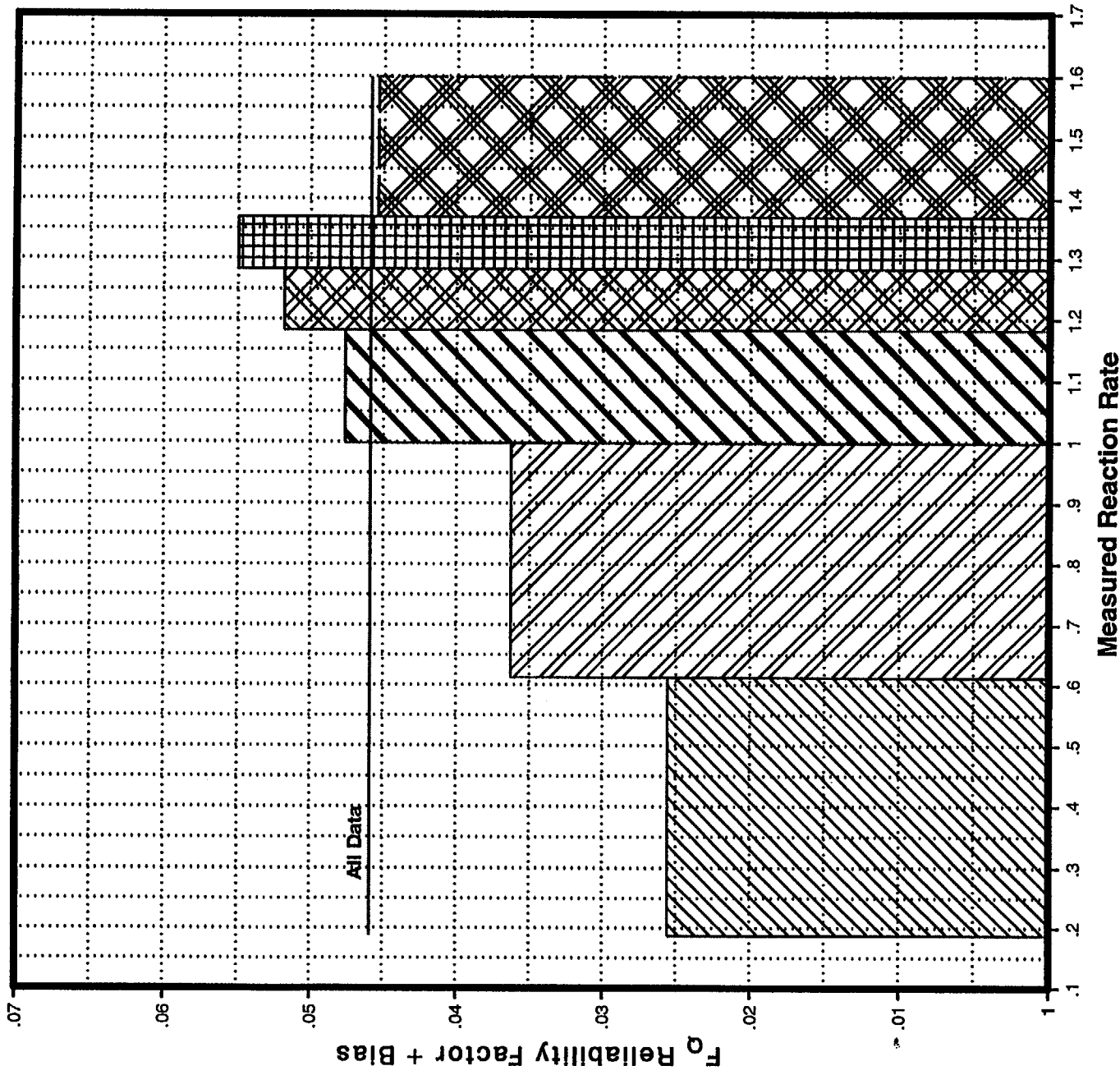


FIGURE 3.5.38

### $F_Q$ Observed Differences Density Function

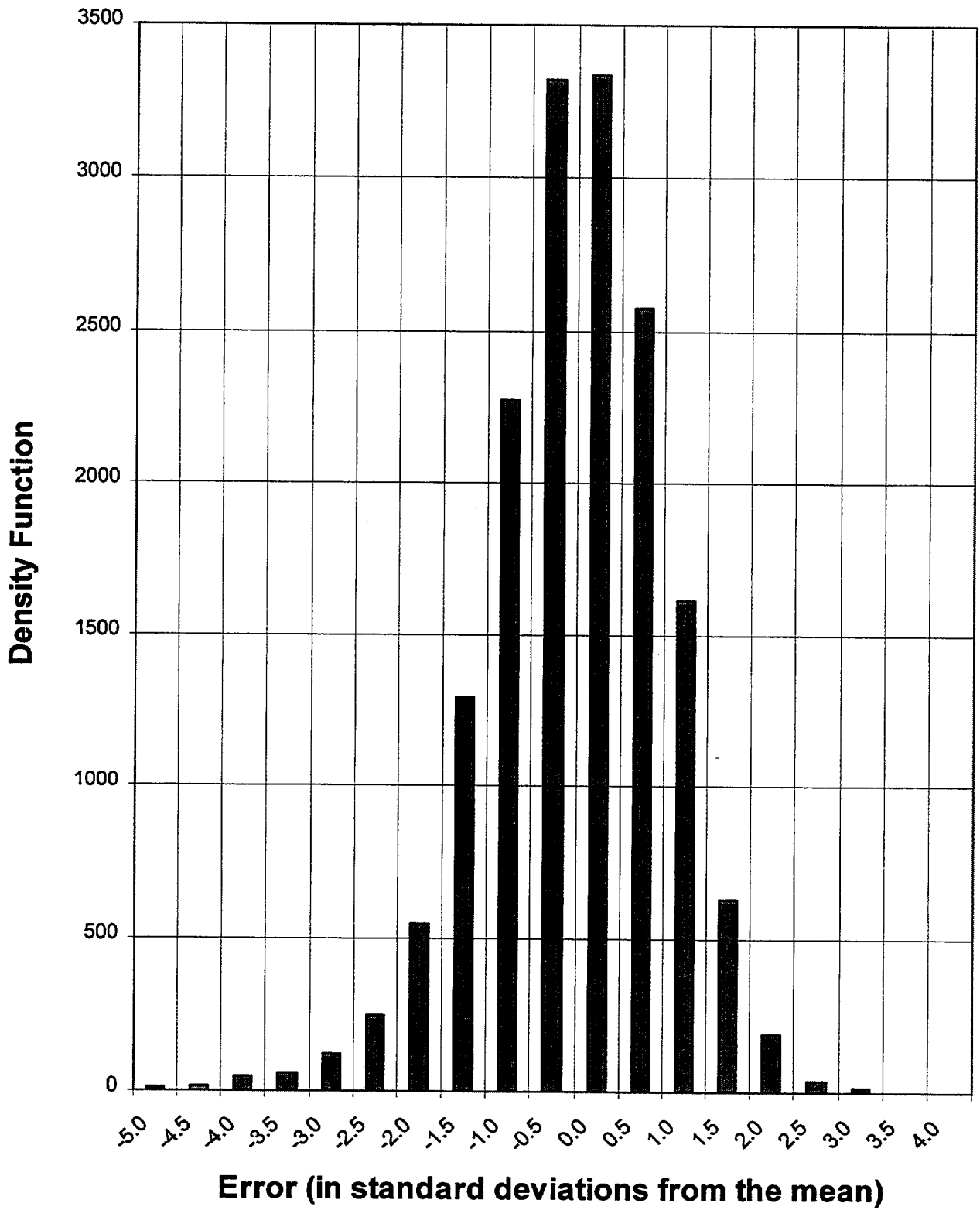


FIGURE 3.5.39

### $F_Q$ Cumulative Distribution Function

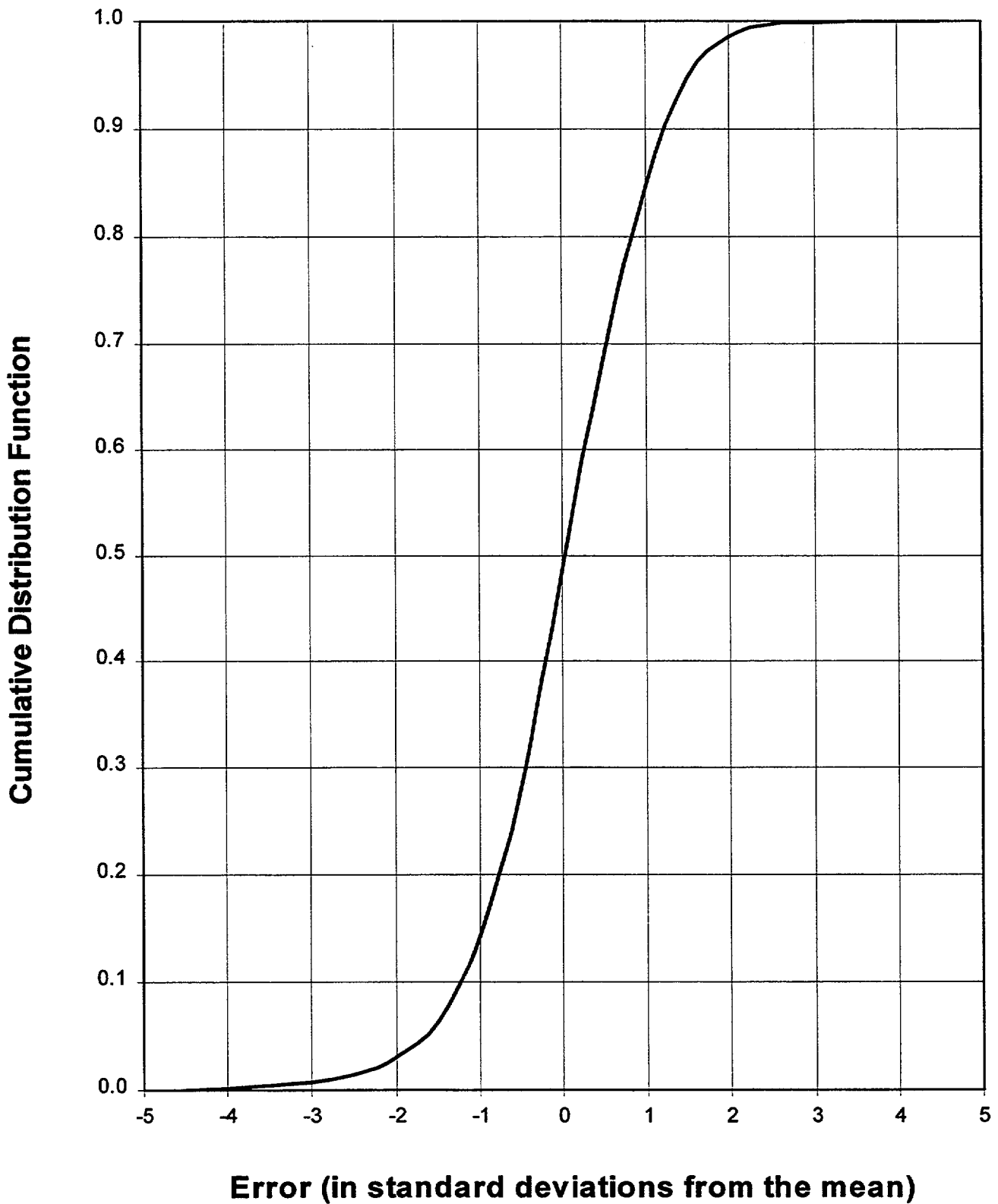


FIGURE 3.5.40

### Cumulative Distribution Function for $F_Q$ in the Region of the 95<sup>th</sup> Percentile

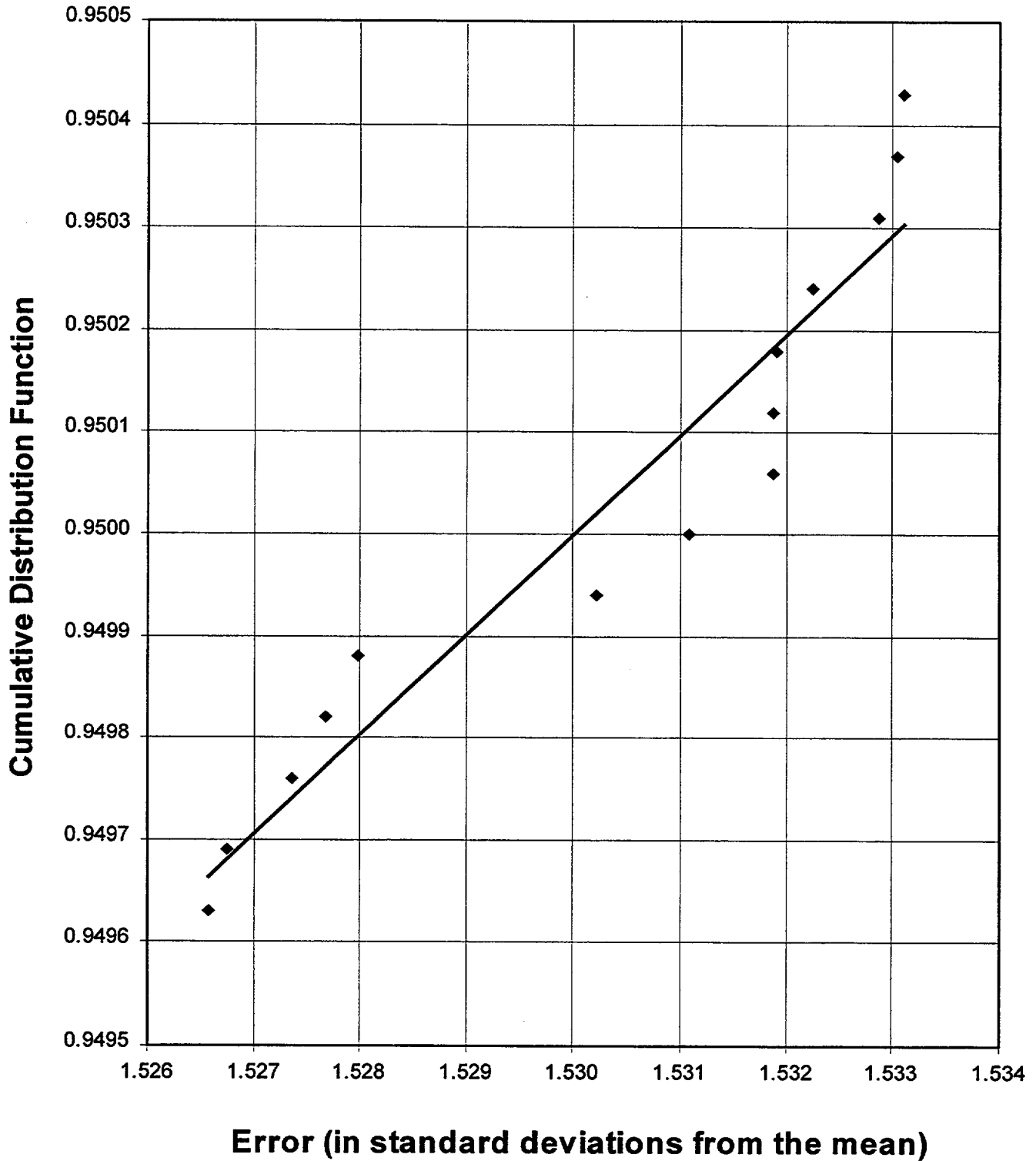


FIGURE 3.5.41

# PI Cycles - P217,P118,P218,P119

$F_{\Delta H}$  Reliability Factor + Bias vs. Measured Reaction Rate

CASMO-4/SIMULATE-3 Model

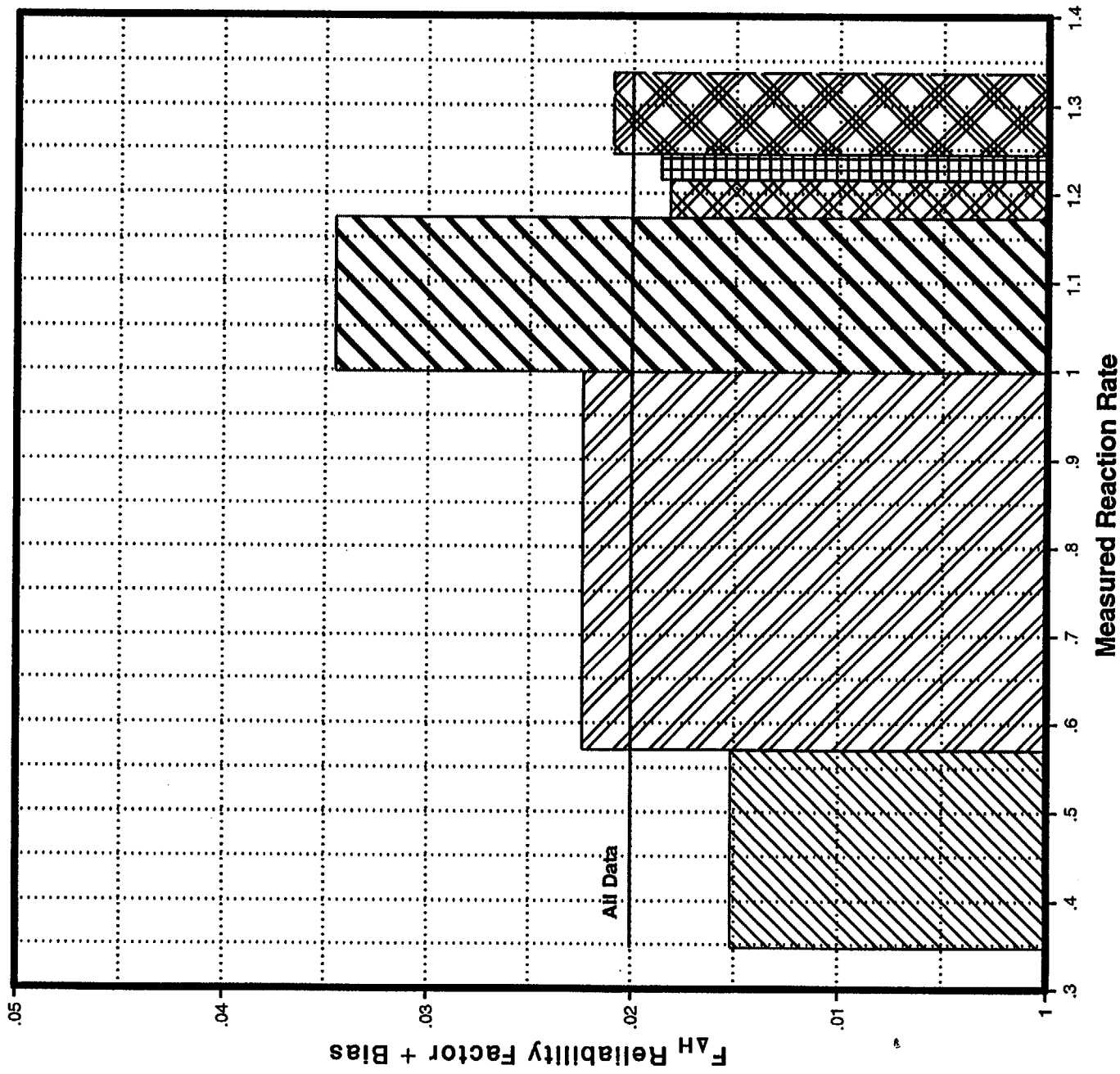


FIGURE 3.5.42

### $F_{\Delta H}$ Observed Differences Density Function

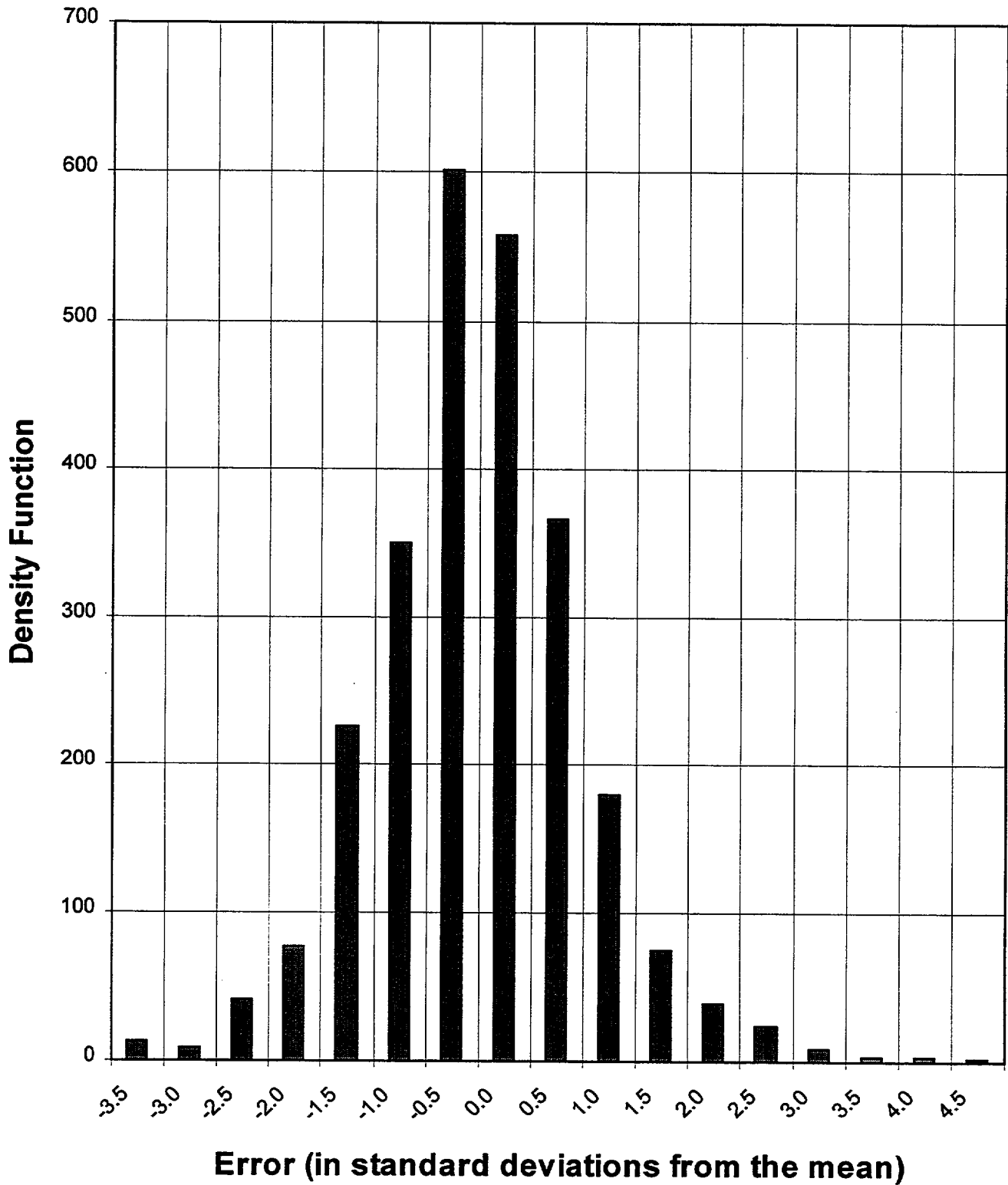


FIGURE 3.5.43

### $F_{\Delta H}$ Cumulative Distribution Function

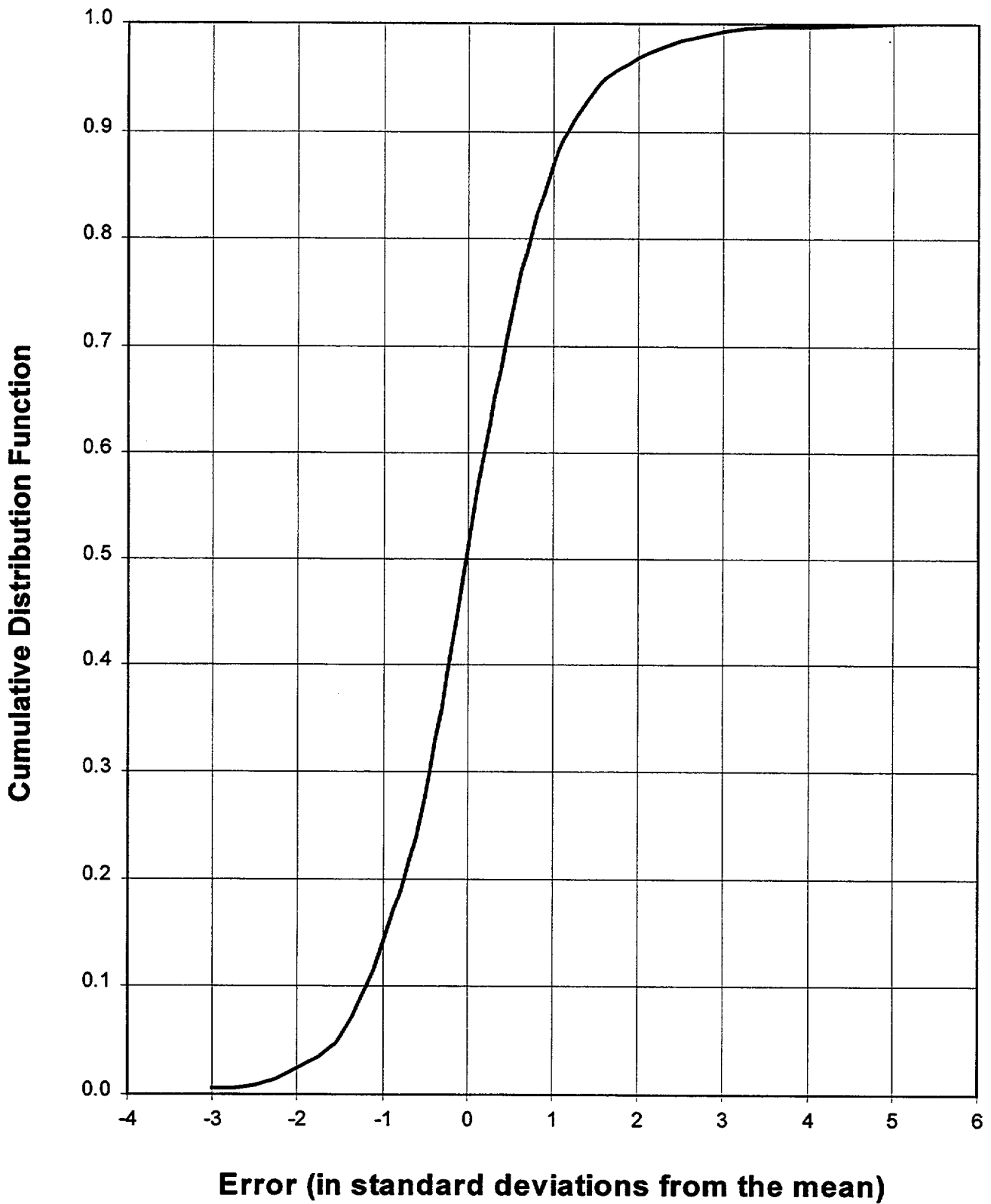
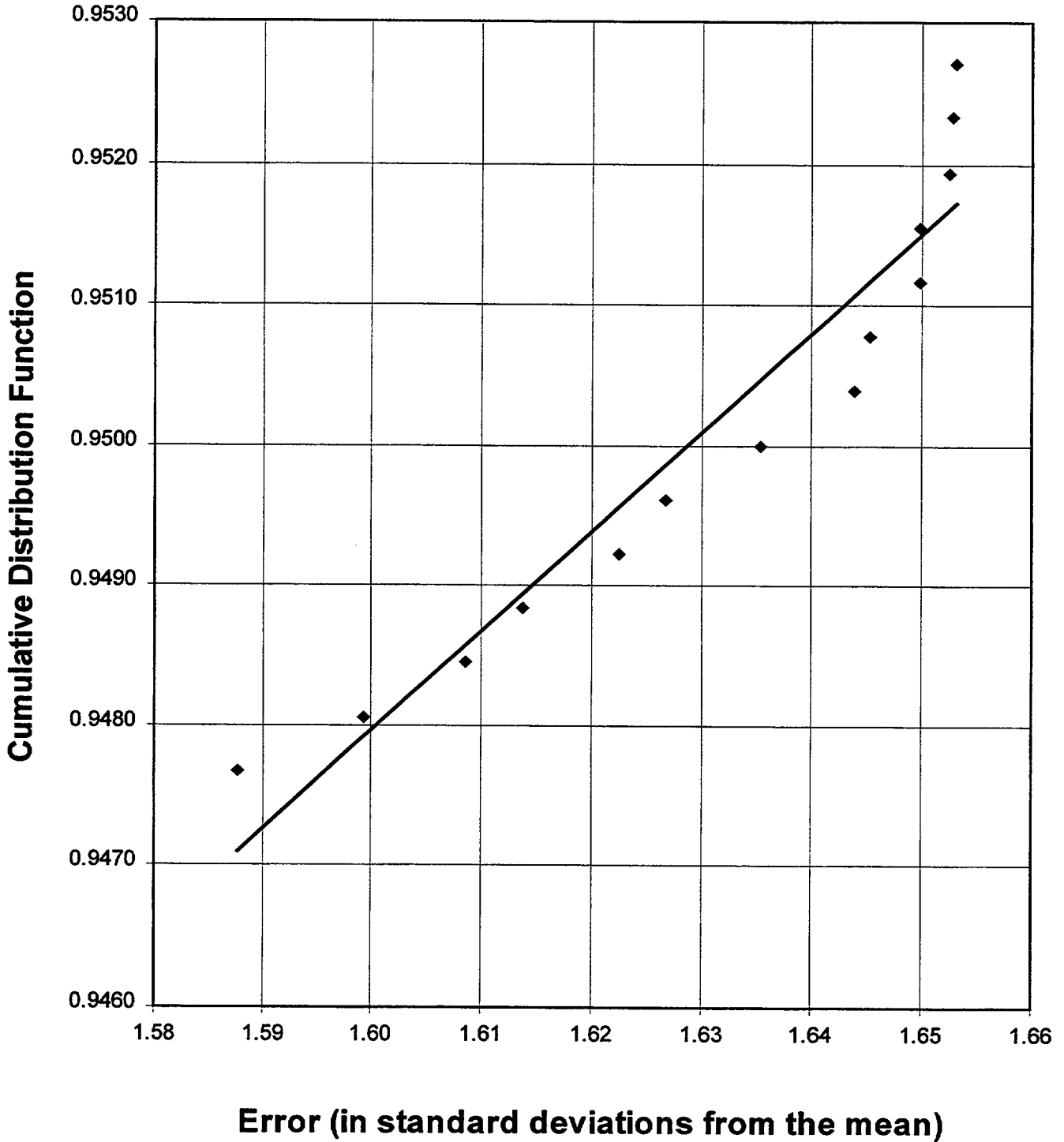


FIGURE 3.5.44

### Cumulative Distribution Function for $F_{\Delta H}$ in the Region of the 95<sup>th</sup> Percentile





### 3.6 Model Application to Plant Transient Operation

In reference 1, this section described model application to Prairie Island Unit 1 plant transient tests performed during cycles 1 and 2. The tests performed were the pseudo ejected rod, rod drop and two xenon transients. For this topical report, cycles 1 and 2 were not modeled so there are no corresponding results to present for the transient tests of reference 1.

In order to demonstrate the applicability of the CASMO-4/SIMULATE-3 model to plant transient operation, the benchmark cycles were reviewed for periods of transient operation. For Prairie Island Unit 2 cycle 17, a reduction to approximately 55% power occurred in late November 1995. During the reduction, the D bank rod control cluster assemblies (RCCA's) were inserted to approximately 183 steps from the nominal, hot full power operating position of 218 steps. The reduction lasted for approximately 26 hours during which time repairs were made to the feed pumps. In addition a flux map was taken shortly into the power reduction. This evolution provided a good set of data for which to benchmark the CASMO-4/SIMULATE-3 model for off-nominal operation.

The process was to model the power reduction maneuver with SIMULATE-3 and compare measured versus calculated soluble boron concentration as a function of time during the xenon transient. This comparison demonstrates the ability of the model to predict core reactivity during a xenon transient. In addition, the flux map was processed with the PRP code (the same code used in Section 3.5; see Appendix B for code description) to compare the measured versus calculated reaction rates. This comparison demonstrates the ability of the model to predict the core power distribution during a transient.

The results of the comparisons are documented in Figures 3.6.1-3.6.4. The upper graph in Figure 3.6.1 shows the power history for the maneuver. The lower graph shows the comparison of the measured and calculated RCS boron concentration in the time frame of the maneuver throughout the xenon transient. The comparisons are quite good, demonstrating that the CASMO-4/SIMULATE-3 model works well to predict the total core reactivity throughout the xenon transient.

The remaining figures represent the results of the power distribution comparisons. Figure 3.6.2 represents the differences between the measured and predicted integrated reaction rates for all instrumented locations. Figure 3.6.3 represents measured versus calculated axial reaction rate comparisons for a fresh assembly in a region of high power density. Figure 3.6.4 represents measured versus calculated axial reaction rate comparisons for an assembly with a partially inserted D bank RCCA. The results presented on these plots demonstrate that the CASMO-4/SIMULATE-3 model is also adequate for predicting the power distribution during off-nominal periods of reactor operation.

FIGURE 3.6.1

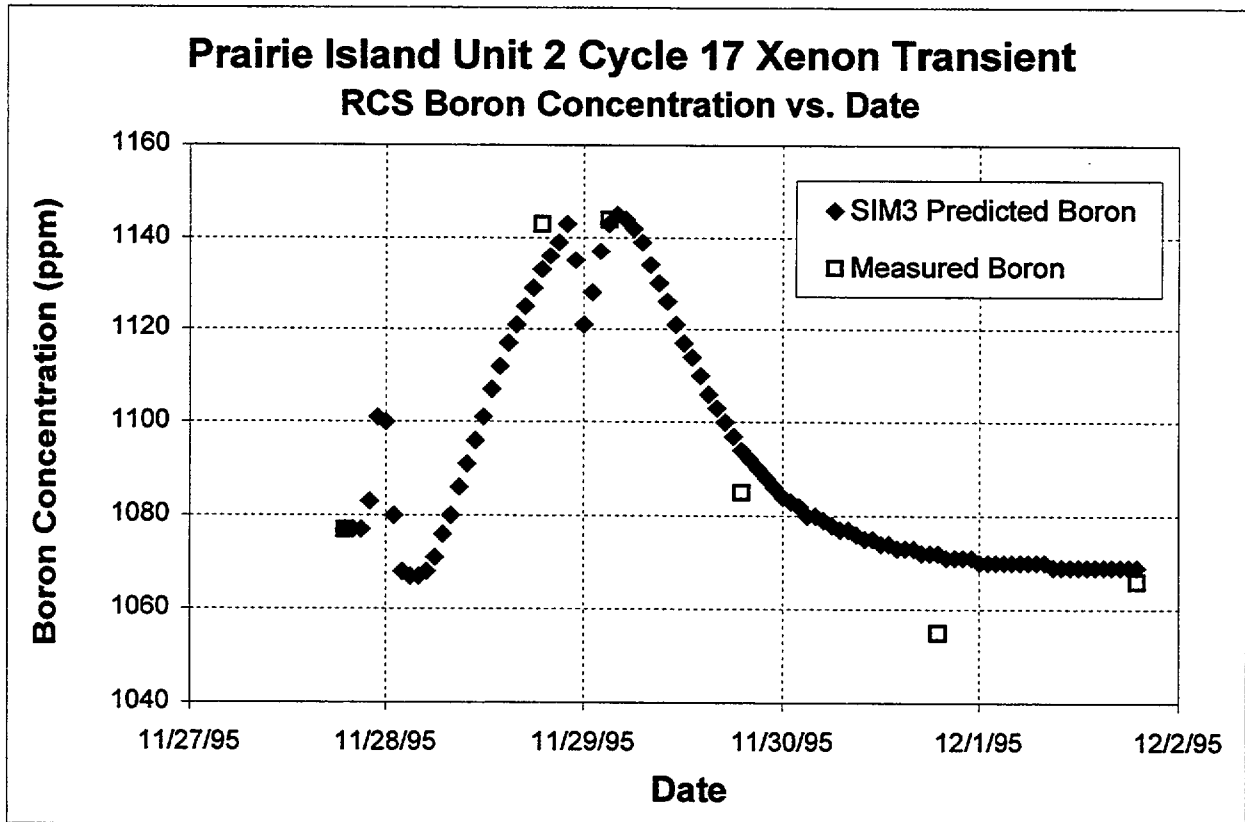
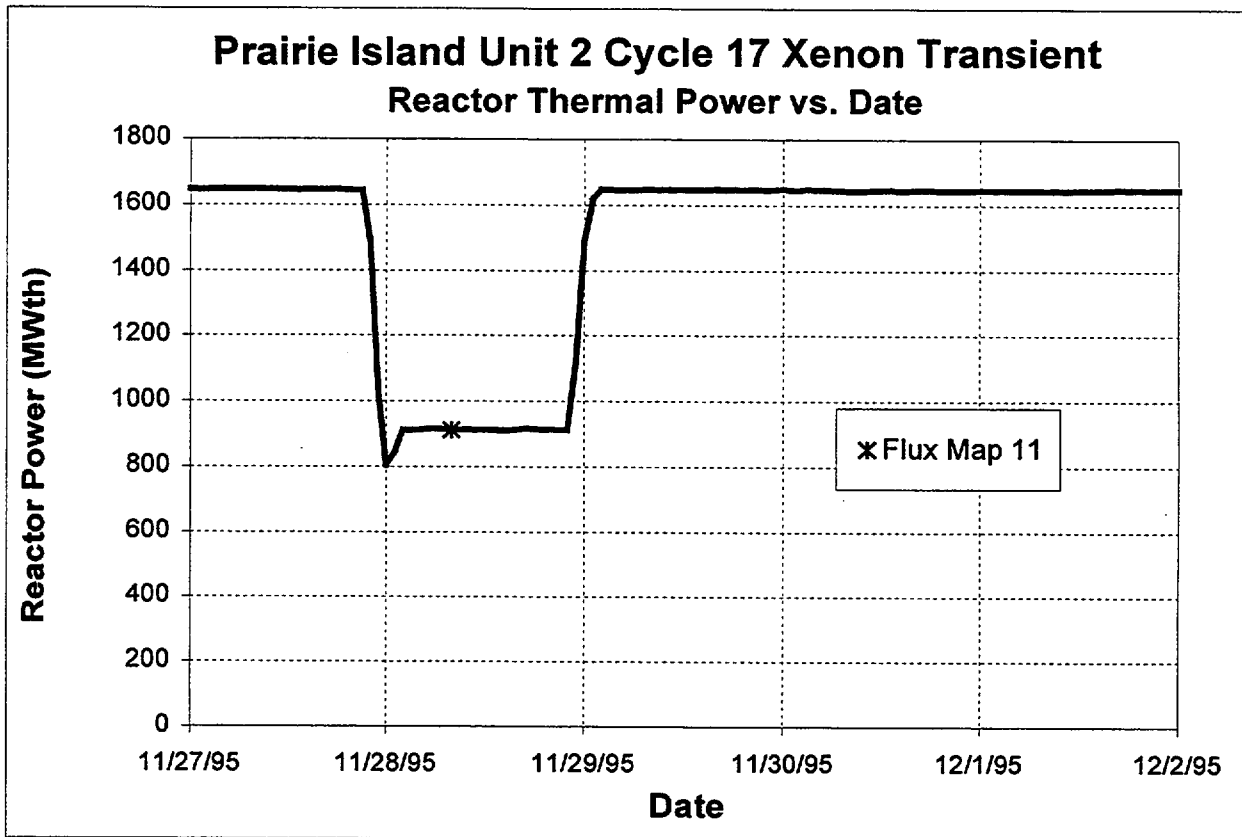


FIGURE 3.6.2

# PI Unit 2 Cycle 17 Measured versus Calculated Integrated Detector Response Differences

**Map 217-11, 5.896 GWd/MTU  
55% Power, D Bank at 184 steps, Transient Xenon Map**

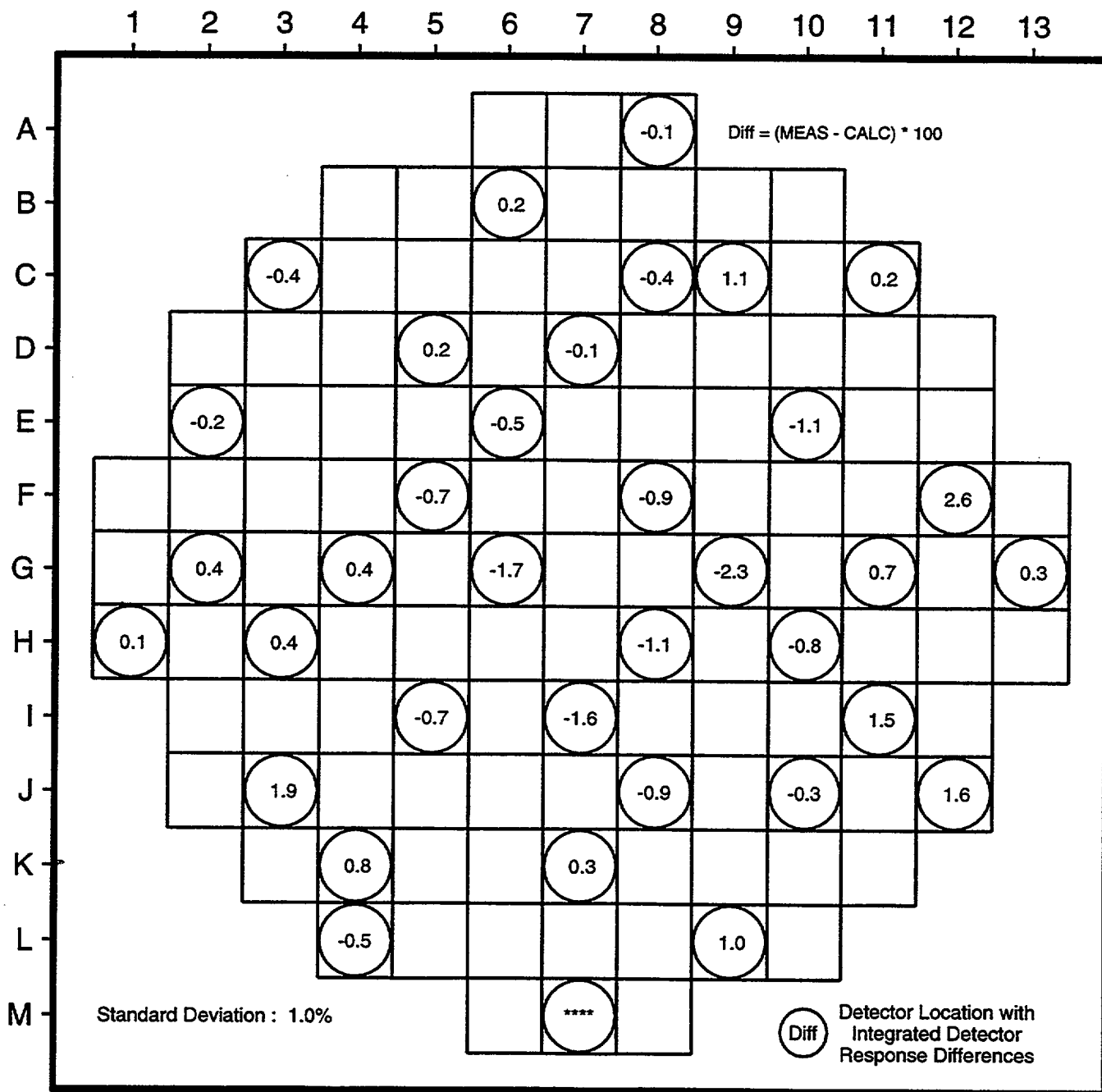


FIGURE 3.6.3

# PI Unit 2 Cycle 17 Measured versus Calculated Detector Response

Map 217-11, 5.896 GWd/MTU  
55% Power, D Bank at 184 Steps, Transient Xenon Map

THIMBLE G-4  
Fresh 4.95 w/o U235, 16 pin 8 w/o Gd

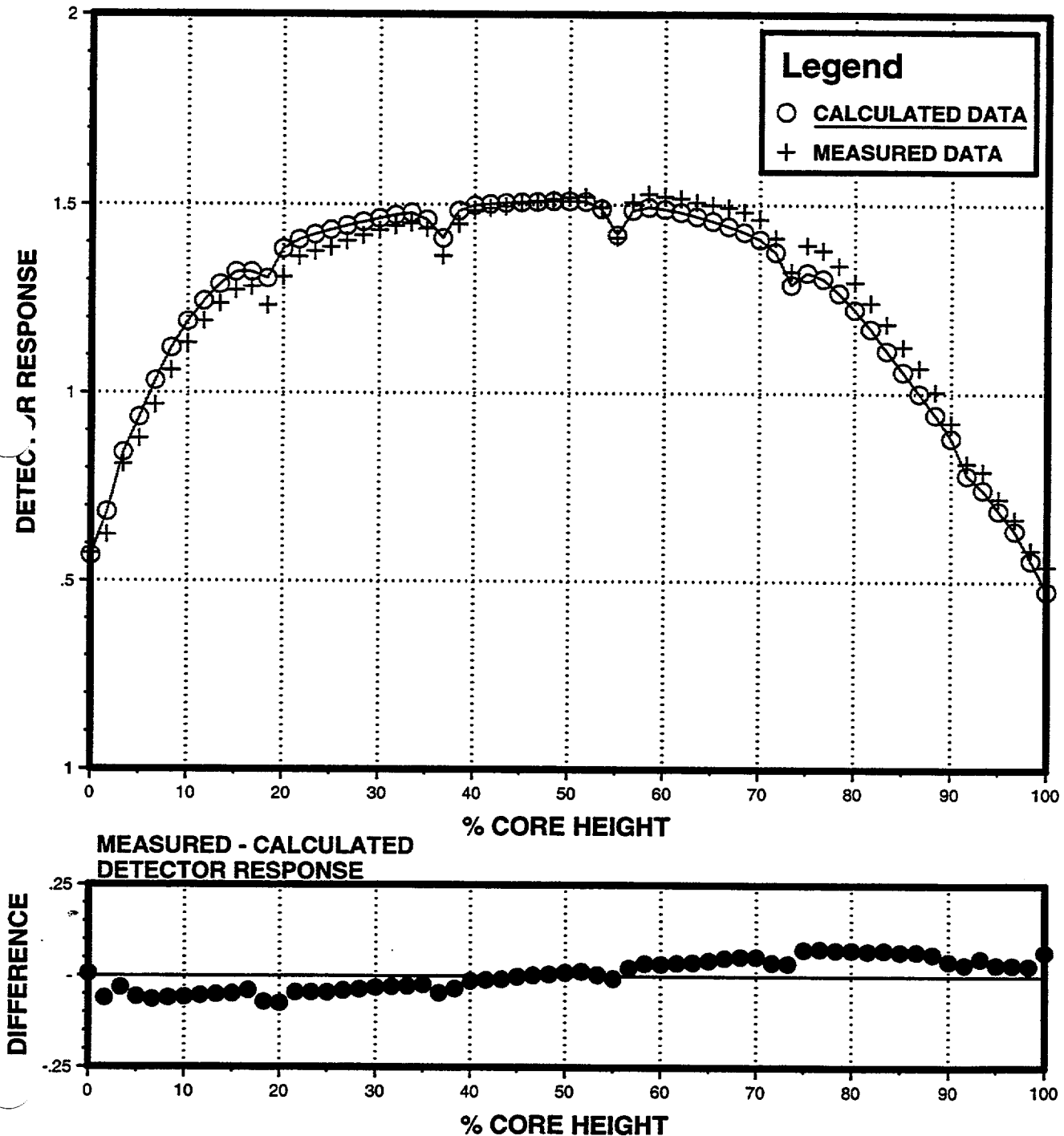


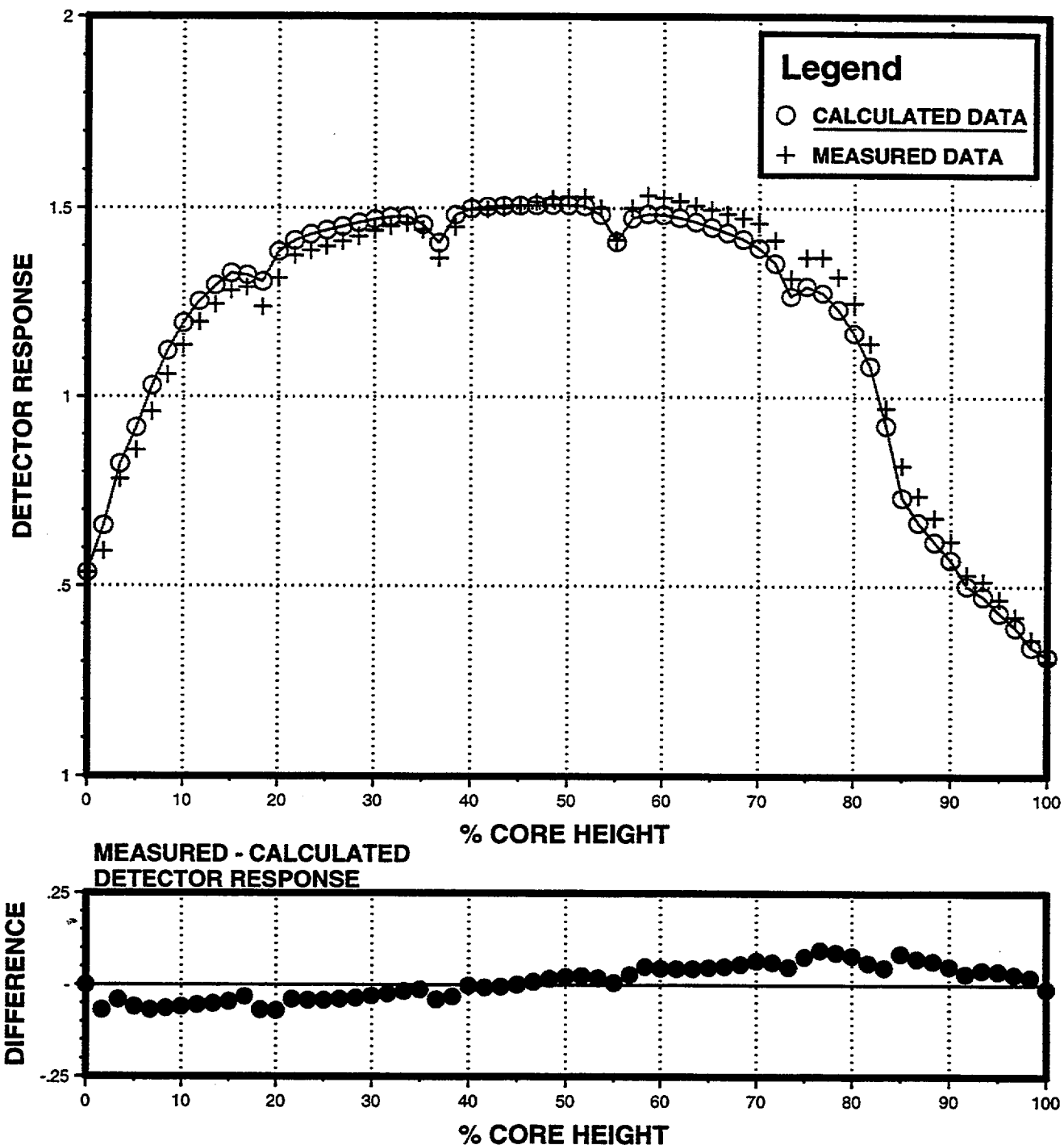
FIGURE 3.6.4

# PI Unit 2 Cycle 17 Measured versus Calculated Detector Response

Map 217-11, 5.896 GWd/MTU  
55% Power, D Bank at 184 Steps, Transient Xenon Map

THIMBLE G-11

Once Burned 4.95 w/o U235, 8 pin 6 w/o Gd, D Bank Rodded Location



### 3.7 Reliability Factor for Delayed Neutron Parameters

This section deals with determining the reliability factor for values which can be calculated but not measured. In these cases, an argument may be made for the general magnitude of the reliability factor without making direct comparisons between measured and predicted values. This section has not changed from reference 1 with the exception that the importance factor that was applied in reference 1 to the flux weighted core average  $\beta_{\text{eff}}$  is now explicitly accounted for in the SIMULATE-3 calculation for the adjoint-flux weighted core average  $\beta_{\text{eff}}$ . In addition, references to the uncertainty for ECELL are removed since this code set is no longer used.

The importance of the reliability of the calculated values of the delayed neutron parameters is primarily associated with the core  $\beta_{\text{eff}}$ . The uncertainties in the calculation of  $\beta_{\text{eff}}$  are composed of several components, the most important of which are listed below:

- a.) Experimental values of  $\beta$  and  $\lambda$  by nuclide
- b.) Calculation of the spatial nuclide inventory
- c.) Calculation of core average  $\beta_{\text{eff}}$  as an adjoint-flux weighted average over the spatial nuclide inventory

The experimental determination of the  $\beta$ 's and  $\lambda$ 's are assumed to be accurate to within 1%. The most important nuclide concentrations with respect to the core  $\beta$  are  $U^{238}$ ,  $U^{235}$  and  $Pu^{239}$ . Table and 3.4.2 of reference 1 indicates that the uncertainty in the calculation of these parameters is about -0.3% for CASMO. Therefore, components a) and b) above are combined as 1.3% for CASMO.

The uncertainty in the calculation of a core average  $\beta$  depends on the relative adjoint-flux weighting of the individual assemblies in the core. For demonstration purposes, consider a three region core, each with a different average burnup and average  $\beta$ , where about a third of the core has seen two previous cycles, a third only one previous cycle and a third is the feed fuel. Typical regional  $\beta$ 's are given below:

Region 1 (third cycle fuel)	$\beta = 0.005$
Region 2 (second cycle fuel)	$\beta = 0.006$
Region 3 (feed fuel)	$\beta = 0.007$

The effect of errors in the calculated flux distribution can be evaluated in terms of the effect on the core average  $\beta$ . As a base case, flux weighting factors are all set to 1.0. In this case, the core average  $\beta = 0.006$ . Using a maximum error in the regional flux weighting of 7.0%, the worst error in the calculation of the core average  $\beta$  is obtained by increasing the weight of the Region 1 fuel and decreasing the weight of the Region 3 fuel. It should be noted that the average relative weighting factor is unity. The revised  $\beta$  is calculated as follows:

$$\beta(1) \times 1.07 = 0.00535$$

$$\beta(2) \times 1.0 = 0.00600$$

$$\beta(3) \times 0.93 = 0.00651$$

$$\beta = 0.00595, \text{ which yields a } -0.8\% \text{ error for component c.) above}$$

The sum of the errors for these three factors for CASMO is as follows:

$$1.3\%(a+b) + 0.8\%(c) = 1.8\%$$

For conservatism, the reliability factor for delayed neutron parameters is set at 4% which is consistent with reference 1.

### 3.8 Effective Neutron Lifetime

An argument similar to the delayed neutron parameter argument is applied to the determination of the effective neutron lifetime ( $\ell^*$ ) uncertainty. As was the case for section 3.7, this section has not been changed from reference 1 with the exception of the removal of references to the ECELL uncertainties. The uncertainty components which go into the calculation of  $\ell^*$  are as follows:

- a.) Experimental values of microscopic cross sections
- b.) Calculation of the spatial nuclide inventory
- c.) Calculation of core average effective neutron lifetime,  $\ell^*$ , as an adjoint-flux weighted average over the spatial nuclide inventory which includes the effects of leakage

Uncertainties for components a.) and b.) are assumed to be the same as described for the calculation of  $\beta_{\text{eff}}$ , that is, 1% uncertainty in the experimental determination of nuclear cross section and -0.3% uncertainty in the determination of the spatial nuclide inventory for CASMO. The core average neutron lifetime depends on adjoint flux weighting of local absorption lifetimes,  $\ell^*$ . If a conservative estimate of the error in regional power sharing (7%) is used in determining the impact on the core average lifetime,  $\ell^*$ , the error in lifetime is on the order of 1.0%. Combining all of these uncertainties linearly results in a total uncertainty of 2.3% for CASMO. Therefore, for conservatism, a 4% reliability factor will be applied to the neutron lifetime calculation when applied to safety related calculations.



## 4.0 MODEL APPLICATIONS TO REACTOR OPERATIONS

This section describes the methods used in applying the reliability factors and biases to reactor operations. It is not the intent of this section to define the procedures used. However, some aspects of these procedures are presented in order to clarify the approach taken in applying the model reliability factors and biases.

### 4.1 Power Distributions

Two categories are considered for application of calculated power distributions to reactor operations, predictive and monitoring. In the case of the predictive calculation, a best estimate of a future core state is desired and therefore only the power distribution ( $F_Q$  and  $F_{\Delta H}$ ) biases in Table 3.0.1 are applied to the predicted distributions.

In the case of the monitoring application, the intent is to supply design input data to the flux map code. NSP intends to continue using the Exxon DETECTOR code, or a functionally similar code, for this purpose. Based on the excellent agreement between measured and calculated reaction rates documented in section 3.5, it is apparent that the results of the DETECTOR program with SIMULATE-3 based DETECTOR constants will be better than the results with Exxon PDQ based DETECTOR constants. Therefore, the current technical specification measurement uncertainties remain conservative and will continue to be used.

### 4.2 Isotopic Inventory

The calculation of the isotopic inventory for Prairie Island is based upon the CASMO-4/SIMULATE-3 model. This is the same model that is used to calculate the flux map design input. Therefore, the accuracy of the burnup distribution can be verified by the agreement of the measured and calculated reaction rates which is discussed in section 3.5. The accuracy of the isotopics versus local exposure is described in Section 3.4 and reference 4. Thus, there will be no change to the process used to calculate burnup and the isotopic inventory other than to supply isotopic ratios from the CASMO-4/SIMULATE-3 model rather than CASMO/PDQ/DP5 model.

### 4.3 Rod Swap Methodology

Reference 5 is an NSP Topical report that describes the methodology for determining control rod reactivity worth using the Rod Swap technique. NSP intends to continue using the methodology described in reference 5 to predict control rod reactivity worth for Prairie Island. The intent is to use the CASMO-4/SIMULATE-3 model to predict control rod worth by the rod swap technique, in place of the CASMO/PDQ/DP5 model discussed in reference 1. Table 4.3.1 documents comparisons of measured and calculated rod worths determined by both the boration/dilution and rod swap techniques for the six

benchmark cycles modeled for this topical report. All comparisons fall well within the  $\pm 10\%$  acceptance criteria for the reference bank and the total rod worth, and within the  $\pm 15\%$  acceptance criteria for the rod swap measured banks. These acceptance criteria are defined in section 3.2 of reference 5. This demonstrates that the CASMO-4/SIMULATE-3 model is acceptable for predicting control rod reactivity worth using the Rod Swap technique according to the methods described in reference 5.

#### 4.4 Transient Power Distribution Methodology

Reference 6 is an NSP Topical report that describes the transient power distribution methodology used to determine  $V(z)$  factors for application to Prairie Island  $F_Q^N$  measurements. The  $V(z)$  factors are applied to equilibrium  $F_Q^N$  measurements to bound the  $F_Q^N$  values that could be measured at non-equilibrium conditions. NSP intends to continue using the methodology described in reference 6 to calculate  $V(z)$  factors for application to Prairie Island  $F_Q^N$  measurements. The intent is to use the CASMO-4/SIMULATE-3 model to calculate  $V(z)$  factors, in place of the CASMO/PDQ/DP5 model discussed in reference 1. Section 3.5 of this Topical report demonstrates that the CASMO-4/SIMULATE-3 model is suitable for predicting equilibrium  $F_Q^N$  values. Section 3.6 demonstrates that the CASMO-4/SIMULATE-3 model is suitable for modeling the non-equilibrium behavior of the core. Taken together, this modeling ability demonstrates that the CASMO-4/SIMULATE-3 model is acceptable for calculating  $V(z)$  factors to be applied to equilibrium  $F_Q^N$  measurements to bound potential non-equilibrium  $F_Q^N$  measurements according to the methods described in reference 6.

TABLE 4.3.1

Measured versus Calculated Control Rod Bank Worths

CASMO-4/SIMULATE-3 Model

Prairie Island		Control Rod Bank <sup>1</sup>	Control Rod Bank Worth (pcm)		% Difference <sup>2</sup>
Unit	Cycle		Measured	Calculated	
1	17	A	1296	1238	4.8
		B	412	436	-5.4
		C	886	847	4.6
		D	804	807	-0.3
		SA	786	708	11.0
		SB	786	708	11.1
		Total	4971	4742	4.8
1	18	A	1063	1091	-2.6
		B	603	654	-7.8
		C	903	908	-0.5
		D	785	799	-1.9
		SA	649	631	2.9
		SB	649	633	2.5
		Total	4652	4717	-1.4
1	19	A	1023	1019	0.4
		B	554	568	-2.6
		C	931	921	1.1
		D	665	665	-0.1
		SA	728	721	0.9
		SB	722	722	0.0
		Total	4621	4616	0.1

<sup>1</sup> Reference bank (A bank for all benchmark cycles) rod worths were determined using the boration/dilution technique. All others were determined using the rod swap technique.

<sup>2</sup> % Difference =  $\frac{(M - C)}{C} * 100\%$  (Note: This formula is consistent with reference 6)

TABLE 4.3.1 (continued)

Measured versus Calculated Control Rod Bank WorthsCASMO-4/SIMULATE-3 Model

Prairie Island		Control Rod Bank <sup>1</sup>	Control Rod Bank Worth (pcm)		% Difference <sup>2</sup>
Unit	Cycle		Measured	Calculated	
2	16	A	1125	1107	1.6
		B	495	543	-8.9
		C	833	833	-0.1
		D	604	586	3.0
		SA	744	711	4.7
		SB	756	733	3.2
		Total	4556	4513	1.0
2	17	A	1103	1078	2.3
		B	486	484	0.3
		C	812	807	0.6
		D	795	768	3.5
		SA	606	575	5.4
		SB	606	572	5.9
		Total	4407	4285	2.8
2	18	A	1141	1156	-1.3
		B	548	571	-4.0
		C	876	882	-0.7
		D	802	837	-4.3
		SA	742	748	-0.9
		SB	742	749	-1.0
		Total	4849	4943	-1.9

<sup>1</sup> Reference bank (A bank for all benchmark cycles) rod worths were determined using the boration/dilution technique. All others were determined using the rod swap technique.

<sup>2</sup> % Difference =  $\frac{(M - C)}{C} * 100\%$  (Note: This formula is consistent with reference 6)

## 5.0 MODEL APPLICATIONS TO SAFETY EVALUATION CALCULATIONS

This section describes the methods used in applying the reliability factors and biases to the results of safety related physics calculations. It is not the intent of this section to define the procedures to be used in performing the physics calculations. However, some aspects of these procedures are presented in order to clarify the approach taken in applying the model reliability factors and biases.

In such applications the question is generally whether or not the reload core will meet established safety limits (i.e., peak linear heat rate, minimum DNBR, shutdown margin, etc.) under normal and transient or accident conditions. The question is usually answered by comparing the calculated kinetics, reactivity, and power distribution parameters of the reload core to those used in the analysis of each accident or transient described in a reference safety analysis such as the Final Safety Analysis Report.

For each parameter of interest,  $RF_x$  and  $Bias_x$  are given in Table 3.0.1. The application of  $RF_x$  and  $Bias_x$  for each parameter of interest is shown below.

### 5.1 Nuclear Heat Flux Hot Channel Factor, $F_Q^N$

The nuclear heat flux hot channel factor,  $F_Q^N$ , is defined as the maximum local fuel rod linear power density divided by the average fuel rod linear power density, assuming nominal fuel pellet and rod parameters. Calculations of  $F_Q^N$  are performed directly with the SIMULATE-3 pin power reconstruction module. References 9 and 10 discuss the SIMULATE-3 pin power reconstruction module and the calculation of  $F_Q^N$ . The model reliability factor and bias listed in Table 3.0.1 are then applied as follows:

$$F_Q^N = (F_Q^N(\text{model}) + RF_{F_Q^N} + Bias_{F_Q^N}) * (1 + T)$$

where T is the azimuthal tilt factor.

### 5.2 Nuclear Enthalpy Rise Hot Channel Factor, $F_{\Delta H}$

The nuclear enthalpy rise hot channel factor is defined as the ratio of the integral of linear power along the rod on which the minimum DNBR occurs to the core average integral rod power. Calculations of  $F_{\Delta H}$  are performed directly with the SIMULATE-3 pin power reconstruction module. References 9 and 10 discuss the SIMULATE-3 pin power reconstruction module and the calculation of  $F_{\Delta H}$ . The model reliability factor and bias listed in Table 3.0.1 are then applied as follows:

$$F_{\Delta H} = (F_{\Delta H}(\text{model}) + RF_{F_{\Delta H}} + Bias_{F_{\Delta H}}) * (1 + T)$$

where T is the azimuthal tilt factor.

### 5.3 Control Rod Worth, $\Delta\rho_{\text{Rods}}$

Control rod worths are calculated using the three-dimensional nodal model. Rod worths are determined by varying the rod position while the independent core parameters such as core power and boron are held constant. The model reliability factor and bias listed in Table 3.0.1 are then applied as follows:

$$\Delta\rho_{\text{Rods}} = \Delta\rho_{\text{Rods}}(\text{model}) * (1 + \text{Bias}_{\text{Rods}}) * (1 \pm \text{RF}_{\text{Rods}})$$

The reliability factor is either added or subtracted, whichever is most conservative, for each particular application.

### 5.4 Moderator Coefficient, $\alpha_{\text{M}}$

The moderator coefficient is a measure of the change in core reactivity due to a change in specific coolant parameters such as density, temperature, and pressure. The moderator temperature coefficient is obtained by varying the core average temperature in nodal calculations while holding all other parameters constant. The model reliability factor and bias listed in Table 3.0.1 are applied as follows:

$$\alpha_{\text{M}} = \alpha_{\text{M}}(\text{model}) + \text{Bias}_{\text{M}} \pm \text{RF}_{\text{M}}$$

The reliability factor is either added or subtracted, whichever is most conservative for each particular application.

### 5.5 Fuel Temperature (Doppler) Coefficient, $\alpha_{\text{D}}$

The Doppler coefficient is a measure of the change in neutron multiplication associated with a change in fuel temperature. Reactivity is changed mainly due to Doppler broadening of the  $\text{U}_{238}$  parasitic resonance absorption cross section due to increases in fuel temperature. This effect is calculated by first calculating the power coefficient. This is the change in core reactivity associated with a change in power, and is composed of changes due to moderator and fuel temperature changes. The 3D nodal code is used to calculate power coefficients as a function of power and exposure. The Doppler coefficient is then calculated by removing the moderator temperature coefficient component from the power coefficient. The model reliability factor and bias listed in Table 3.0.1 are then applied as follows:

$$\alpha_{\text{D}} = \alpha_{\text{D}}(\text{model}) * (1 + \text{Bias}_{\text{D}}) * (1 \pm \text{RF}_{\text{D}})$$

The reliability factor is either added or subtracted, whichever is most conservative for each particular application.

## 5.6 Boron Concentration Coefficient, $\alpha_B$

The boron concentration coefficient is a measure of the change in neutron multiplication associated with a change in boron concentration. Calculations of  $\alpha_B$  are performed using the three-dimensional nodal model. The model reliability factor and bias listed in Table 3.0.1 are then applied as follows:

$$\alpha_B = \alpha_B(\text{model}) * (1 + \text{Bias}_B) * (1 \pm \text{RF}_B)$$

The reliability factor is either added or subtracted, whichever is most conservative for each particular application.

## 5.7 Effective Delayed Neutron Fraction, $\beta_{\text{eff}}$

Average delayed neutron fractions are determined with the SIMULATE-3 model calculation of core average  $\beta_{\text{eff}}$  as an adjoint-flux weighted average over the spatial nuclide inventory. The model reliability factor and bias listed in Table 3.0.1 are then applied as follows:

$$\beta_{\text{eff}} = \beta_{\text{eff}}(\text{model}) * (1 + \text{Bias}_\beta) * (1 \pm \text{RF}_\beta)$$

The reliability factor is either added or subtracted, whichever is most conservative for each particular application.

## 5.8 Prompt Neutron Lifetime, $\ell^*$

The prompt neutron lifetime is calculated using the SIMULATE-3 model calculation of core average effective neutron lifetime,  $\ell^*$ , as an adjoint-flux weighted average over the spatial nuclide inventory which includes the effects of leakage. The model reliability factor and bias listed in Table 3.0.1 are then applied as follows:

$$\ell^* = \ell^*(\text{model}) * (1 + \text{Bias}_{\ell^*}) * (1 \pm \text{RF}_{\ell^*})$$

The reliability factor is either added or subtracted, whichever is most conservative for each particular application.

## 5.9 Shutdown Margin, (SDM)

Upon receiving a signal for reactor trip, the control rods fall into the active core. Consistent with NRC General Design Criteria 27, the highest worth control rod is assumed to remain stuck in its full out position. The negative reactivity insertion caused by the rods entering the core is offset in part by positive reactivity insertion due to the so called power defect. The power defect components include reactivity insertions due to decreases in fuel temperature (Doppler defect), decreases in moderator temperature and

flux redistribution. The resulting net negative reactivity inserted is the shutdown margin. Shutdown margin calculations are performed using the 3D nodal model in order to evaluate the negative reactivity resulting from a reactor trip in the safety analyses.

The SDM calculation consists of determining the highest worth stuck rod and shutdown reactivity. Consideration is given to the range of initial power, xenon distributions and control rod initial positions consistent with the power dependent insertion limits. One case is performed at hot full power (HFP) with the desired xenon distribution and control rod positions. A second case is performed at hot zero power (HZP) with the xenon and control rod positions consistent with the first case. The reactivity difference between these two cases gives the power defect. The Doppler defect uncertainty,  $RF_{DD}$ , from Table 3.0.1 is applied to the entire power defect rather than to only the Doppler defect component of the power defect.

Next a third case is run at the N-1 rod condition which consists of all control rods inserted with the exception of the highest worth rod. This case is run at the same power and xenon conditions as case 2. The reactivity difference between the second and third cases gives the control rod worth. The rod worth uncertainty,  $RF_{Rods}$ , from Table 3.0.1 is applied to the control rod worth in a conservative fashion. The following case list tabulates the process:

1. Positive reactivity inserted from the power decrease (Power defect):

Case 1 (HFP, Xenon<sub>1</sub>, Rods<sub>1</sub>),  $k_{eff}$

Case 2 (HZP, Xenon<sub>1</sub>, Rods<sub>1</sub>),  $k_{eff}$

$$\text{Power defect (Doppler, Moderator, Flux Redistribution)} = \Delta\rho_{(Case2-Case1)} * (1 + RF_{DD})$$

2. Negative reactivity inserted from the control rod insertion:

Case 2 (HZP, Xenon<sub>1</sub>, Rods<sub>1</sub>),  $k_{eff}$

Case 3 (HZP, Xenon<sub>1</sub>, Rods<sub>3=N-1</sub>),  $k_{eff}$

$$\text{Control rod worth} = \Delta\rho_{(Case3-Case2)} * (1 - RF_{Rods})$$

3. Shutdown margin =  $\Delta\rho_{(Case3-Case2)} * (1 - RF_{Rods}) + \Delta\rho_{(Case2-Case1)} * (1 + RF_{DD})$

## 5.10 Scram Worth Versus Time, $\Delta\rho_{scram}(t)$

Scram worth is the rod worth inserted into the core as a function of time after rod release. The most reactive rod is assumed to remain fully withdrawn. The 3D nodal model is used to obtain reactivity insertion versus rod position. The rod position is converted into a time dependent function using empirical data relating rod position to time after rod release. This gives reactivity insertion versus time. The model reliability factor and bias



are applied in the same manner as for rod worth, described in Section 5.3, as follows:

$$\Delta\rho_{\text{scram}}(t) = \Delta\rho_{\text{scram}}(t)(\text{model}) * (1 + \text{Bias}_{\text{Rods}}) * (1 \pm \text{RF}_{\text{Rods}})$$

The reliability factor is either added or subtracted, whichever is most conservative, for each particular application.

## 6.0 REFERENCES

1. NSP Topical, "Qualification of Reactor Physics Methods for Application to PI Units", NSPNAD-8101-A, Rev.1, December 1982.
2. M. Edenius, "Benchmarking of CASMO Resonance Integrals for U-238 Against Hellstrand's Measurements. Comparisons between CASMO-3 Versions 4.4 and 4.7", Studsvik of America, Inc., SOA-93/04, March, 1993.
3. Malte Edenius, "CASMO Doppler Coefficients Versus MCNP-3A Monte Carlo Calculations", *Transactions of the American Nuclear Society*, Volume 70, pg. 348, New Orleans, LA, June 1994.
4. Kim Ekberg, "CASMO-4 Benchmark Against Yankee Rowe Isotopic Measurements", *Tagungsbericht Proceedings*, ISSN 0720-9207, Jahrestagung Kerntechnik, May 1997.
5. NSP Topical, "Prairie Island Units 1 and 2 Rod Swap Methodology", NSPNAD-8408-A.
6. NSP Topical, "Prairie Island Units 1 and 2 Transient Power Distribution Methodology", NSPNAD-93003-A.
7. M. Edenius, K. Ekberg, B. H. Forssén, D. Knott, "CASMO-4 A Fuel Assembly Burnup Program User's Manual", Studsvik of America, Inc., and Studsvik Core Analysis AB, SOA-95/1 Rev. 0, September, 1995.
8. D. Knott, B. H. Forssén, M. Edenius, "CASMO-4 A Fuel Assembly Burnup Program Methodology", Studsvik of America, Inc., and Studsvik Core Analysis AB, SOA-95/2 Rev. 0, September, 1995.
9. A. S. DiGiovine, J. D. Rhodes III, K. S. Smith, D. M. Ver Planck, and J. A. Umbarger, "SIMULATE-3 Advanced Three-Dimensional Two-Group Reactor Analysis Code User's Manual", Studsvik of America, Inc., SOA-95/15 Rev. 0, October, 1995.
10. J. T. Cronin, K. S. Smith, D. M. Ver Planck, J. A. Umbarger, and M. Edenius, "SIMULATE-3 Methodology, Advanced Three-Dimensional Two-Group Reactor Analysis Code", Studsvik of America, Inc., SOA-95/18 Rev. 0, October, 1995.
11. D. M. Ver Planck, K. S. Smith, and J. A. Umbarger, "TABLES-3 Library Preparation Code for SIMULATE-3", Studsvik of America, Inc., SOA-95/16 Rev. 0, October, 1995.

12. I. B. Fiero, M. A. Krammen, H. R. Freeburn, et al, "ESCORE-The EPRI Steady-State Core Reload Evaluator Code: General Description", Electric Power Research Institute, EPRI NP-5100-L-A, April, 1991.
13. M. A. Krammen, H. R. Freeburn, et al, "ESCORE-The EPRI Steady-State Core Reload Evaluator Code Volume 1: Theory Manual", Electric Power Research Institute, EPRI NP-4492-CCMP Volume 1, August, 1986.
14. M. A. Krammen, R. B. Fancher, N. T. Yackle, et al, "ESCORE-The EPRI Steady-State Core Reload Evaluator Code Volume 2: User's Manual", Electric Power Research Institute, EPRI NP-4492-CCMP Volume 2, August, 1986.
15. M. A. Krammen, R. B. Fancher, M. W. Kennard, et al, "ESCORE-The EPRI Steady-State Core Reload Evaluator Code Volume 3: Programmer's Manual", Electric Power Research Institute, EPRI NP-4492-CCMP Volume 3, August, 1986.
16. D. B. Owen, "Factors for One-Sided Tolerance Limits and for Variables Sampling Plans", Sandia Corporation, March 1963.
17. M. G. Kendall, A. Stuart, J. K. Ord, "Kendall's Advanced Theory of Statistics", Vol. 1, 5<sup>th</sup> edition, Oxford University Press, N. Y., 1987.

## APPENDIX A Statistical Methods for the Determination and Application of Uncertainties

The purpose of using statistical methods is to determine the value  $X_c$  (calculated) such that there is a 95% probability at the 95% confidence level that  $X_c$  will be conservative with respect to  $X_T$  (true value) when applying the calculational methods to safety related reactor analyses.

The first step is to determine whether or not a distribution is normal. If it is, the methods described in Section A.1 are used. If the distribution cannot be treated as normal, but the distributions are known, then the methods described in Section A.2 are used.

If neither of the above methods apply, then the parameter in question is conservatively bounded.

Note that the statistical methods presented in this Appendix are identical to those that were originally presented in reference 1.

## A.1 Application of Normal Distribution Statistics

### Separation of Measurement and Computational Uncertainties

Comparisons of measured and calculated reactor parameters include the effects of both the measurement and calculational uncertainties. Methods used in this report to isolate the calculational uncertainties are described below in terms of the following definitions:

$X_T$  = true reactor parameter

$X_m$  = measured reactor parameter

$X_c$  = calculated reactor parameter

$e_m = X_m - X_T$  = measurement error

$e_c = X_c - X_T$  = calculation error

$e_{mc} = X_m - X_c$  = observed differences

$$\mu = \frac{\sum_{i=1}^n e_i}{n} = \text{mean error}$$

$$\sigma = \sqrt{\frac{\sum_{i=1}^n (e_i - \mu)^2}{n - 1}} = \text{standard deviation}$$

If  $e_m$  and  $e_c$  are independent, then the following relationships exist. (Note that these relationships apply for non-normal distributions as well):

$$\sigma_c^2 = \sigma_{mc}^2 - \sigma_m^2$$

$$\mu_c = \mu_c - \mu_{mc}$$

Once  $\sigma_c$  and  $\mu_c$  have been calculated from historical data, they can be used to apply conservatism to future calculations of reactor parameters,  $X_c$ , as follows:

$$X_c^{\text{final}} = X_c + \mu_c \pm K_c \sigma_c$$

The factor  $K_c$  is defined to provide a 95% probability at the 95% confidence level that  $X_c$  is conservative with respect to the true value,  $X_T$ . The quantity  $K_c \sigma_c$  is either added or subtracted depending on which is conservative.

## Reliability Factors

It is the objective to define reliability factors which are to be used to increase or decrease calculated results to the point where there is a 95% probability at the 95% confidence level that they are conservative with respect to actual reactor parameters.

For any given application, there is concern only with one side of the component; that is, if the calculated value is too large or too small. Therefore, one-sided tolerance limits based on normal distributions may be used to find a  $K_c$  which will give a 95% probability at the 95% confidence level to the reliability factor defined by:

$$RF = K_c \sigma_c$$

An example of numerical values of  $K_c$  for various sample sizes is provided in Table A.1.

TABLE A.1

Single Sided Tolerance Factors (reference 16)

n	$K_c$
2	26.26
3	7.66
4	5.15
5	4.20
6	3.71
7	3.40
8	3.19
9	3.03
10	2.91
11	2.82
12	2.74
15	2.57
20	2.40
25	2.29
30	2.22
40	2.13
60	2.02
100	1.93
200	1.84
500	1.76
$\infty$	1.645

n = Number of data points used for  $\sigma$

## A.2 Application of Non-Normal Distribution Statistics

If a distribution is determined to be other than normal, the requirement is that there is a 95% confidence level that  $X_c$  will be conservative with respect to the true value,  $X_T$ . (In the following, the notation used is consistent with that defined in Section A.1). It is thus required that a 95% upper confidence limit be determined for the 95<sup>th</sup> percentile of the distribution of errors.

In the calculation, a set of error observations ( $e_i$ ) are determined. The mean ( $\mu_{mc}$ ) and the standard deviation ( $\sigma_{mc}$ ) are calculated using the following formulation:

$$\mu_{mc} = \frac{\sum_{i=1}^n e_i}{n}$$

$$\sigma_{mc} = \sqrt{\frac{\sum_{i=1}^n (e_i - \mu_{mc})^2}{n - 1}}$$

Note that the  $e_i$  above are determined from the following:

$$e_i = e_{mc} = X_m - X_c = \text{observed differences}$$

Generally, the  $e_{mc}$  are taken from several cycles of operation; thus, they represent the true distribution. The  $e_i$  are then transformed to standard measure by the following formula:

$$Z_i = \frac{e_i - \mu_{mc}}{\sigma_{mc}}$$

The resulting variates ( $Z_i$ ) are sorted into ascending order and the  $k^{\text{th}}$  variate is chosen (such that  $k \geq .95n$ ) as an estimate of the 95<sup>th</sup> percentile of the distribution (see reference 17, pp. 50-51). This gives a 95<sup>th</sup> percentile of  $Z$  to be  $Q_{95}$ . This implies that 95% of the errors are likely to be less than  $Q_{95}$ .

It remains to calculate a 95% confidence interval for  $Q_{95}$ . (The formula for this calculation is taken from reference 17, pp. 330-331):

$$\text{Var}Q_{95} = \frac{q(1-q)}{n \cdot f_1^2}$$

where:  $q$  = the quantile (.95)

$n$  = number of independent observations in sample

$f_1$  = ordinate of the density function of the distribution of observed differences at abscissa  $q$



It is necessary to determine if the observations are independent. If they are not independent, it is necessary to reduce the sample size to account for the dependence in the determination of the 95% confidence level.

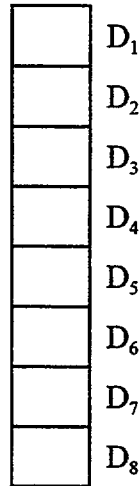


Figure A.2.1 Differences for Nearby Positions

To set notation, let  $\delta_{.95}$  be the population 95<sup>th</sup> percentile for the observed differences, that is:  $P[D_i \leq \delta_{.95}] = .95$ . It is desired to determine a 95% upper confidence limit for  $\delta_{.95}$  when some of the differences are dependent. For differences observed at adjacent positions, the appropriate measure of association for this analysis can be shown to be:

$$C(1) = P[D_1 \leq \delta_{.95} \text{ and } D_2 \leq \delta_{.95}] - (.95)^2$$

The association of differences observed at locations two apart is also considered:

$$C(2) = P[D_1 \leq \delta_{.95} \text{ and } D_3 \leq \delta_{.95}] - (.95)^2$$

and, more generally:

$$C(k) = P[D_1 \leq \delta_{.95} \text{ and } D_{1+k} \leq \delta_{.95}] - (.95)^2$$

for  $k = 1, 2, 3, 4, 5, 6, 7$  locations apart. In this example, there are 8 differences,  $D_i$ , 7 adjacent pairs,  $(D_i, D_{i+1})$ , 6 pairs with indices two apart,  $(D_i, D_{i+2})$ , ..., and 1 pair  $D_1 D_8$ .

Let  $d_{(s)}$  be the sample 95<sup>th</sup> percentile with  $s$  selected to be the smallest integer not less than  $.95n$ . The large sample distribution of  $d_{(s)}$  depends on that of:

$$T(x) = \text{number of differences, } D_i, \text{ that are less than or equal to } x.$$

Even with dependence among the  $D_i$ ,

$$\frac{T(x) - nF(x)}{\text{s.d.}[T(x)]} = \frac{\frac{1}{\sqrt{n}}(T(x) - nF(x))}{\frac{1}{\sqrt{n}}\text{s.d.}[T(x)]}$$

will be approximately standard normal. Here  $F(x) = P[D_i \leq x]$  and  $f(x)$  is the probability density function for the observed differences.

It follows that:

$$P[\sqrt{n}(d_{(s)} - \delta_{.95}) \leq z] = 1 - P\left[T(\delta_{.95} + n^{-1/2}z) \leq s - 1\right]$$

$$\approx 1 - \Phi\left[\frac{-f(\delta_{.95})z}{\frac{1}{\sqrt{n}}\text{s.d.}[T(\delta_{.95})]}\right]$$

where:

$$\left[\frac{1}{\sqrt{n}}\text{s.d.}[T(\delta_{.95})]\right]^2 = \frac{1}{n}\left[n(.95)(.05) + 2\frac{7}{8}nC(1) + 2\frac{6}{8}nC(2) + \dots + \frac{2}{8}nC(7)\right]$$

$$= (.95)(.05) + \frac{14}{8}C(1) + \frac{12}{8}C(2) + \frac{10}{8}C(3) + \dots + \frac{2}{8}C(7)$$

Under independence,  $0 = C(1) = C(2) = \dots = C(7)$  and this expression reduces to its customary value  $(.95)(.05)$ . If the differences are dependent, the variance of  $d_{(s)}$  is:

$$\frac{(.95)(.05)}{nf^2(\delta_{.95})} \left[1 + \sum_{k=1}^7 \frac{2(8-k)C(k)}{8(.95)(.05)}\right]$$

In order to apply this result,  $C(1)$  is estimated by:

$$\hat{C}(1) = \frac{\text{number of adjacent pairs, } (D_i, D_{i+1}), \text{ where both are } \leq d_{(s)} - (.95)^2}{\text{total number of adjacent pairs}}$$

The estimate of  $C(2)$  is:

$$\hat{C}(2) = \frac{\text{number of pairs, } (D_i, D_{i+2}), \text{ where both are } \leq d_{(s)} - (.95)^2}{\text{total number of pairs, } (D_i, D_{i+2})}$$

and,

$$\hat{C}(k) = \frac{\text{number of pairs, } (D_i, D_{i+k}), \text{ where both are } \leq d_{(s)}}{\text{total number of pairs, } (D_i, D_{i+k})} \cdot (.95)^2$$

for  $k = 3, 4, 5, 6, 7$ . The value of  $f^2(\delta_{.95})$  can be estimated as previously suggested. Then, the large sample upper 95% confidence limit for  $\delta_{.95}$ , adjusted for dependence among differences by location, is given by:

$$d_{(s)} + \frac{1.645}{\sqrt{n}} \left[ \frac{(.95)(.05)}{f^2(\delta_{.95})} \left( 1 + \sum_{k=1}^7 \frac{2(8-k)\hat{C}(k)}{8(.95)(.05)} \right) \right]^{1/2}$$

One interpretation of this confidence limit, or the variance expression, is that the total sample size,  $n$ , is effectively reduced by the dependence. The effective sample size is estimated to be:

$$\frac{n}{1 + \sum_{k=1}^7 \frac{2(8-k)\hat{C}(k)}{8(.95)(.05)}}$$

If only two terms are used, the effective sample size is estimated to be:

$$n \left[ \frac{(.95)(.05)}{(.95)(.05) + \frac{14}{8}\hat{C}(1) + \frac{12}{8}\hat{C}(2)} \right]$$

It is necessary to obtain an estimate of  $f_1(.95)$  on a short interval of the cumulative distribution function of  $z$  in the region of the 95<sup>th</sup> percentile. The slope of the cumulative distribution function is an estimate of the ordinate of the density function since the density function is simply the derivative of the cumulative distribution function. Thus:

$$\sigma_{Q_{.95}}^2 = \text{Var}Q_{.95}$$

This value then allows an estimate of the 95% confidence limit on  $Q_{.95}$ . Even though nothing is known about the distribution of  $Q_{.95}$ , the distribution can be shown to be normal using the following derivation:

$$P[D_1 \leq \delta_{.95} \text{ and } D_2 \leq \delta_{.95}]$$

where  $\delta_{.95}$  is the 95<sup>th</sup> percentile of the distribution of differences. If the differences,  $D_1$  and  $D_2$ , are independent:

$$P[D_1 \leq \delta_{.95} \text{ and } D_2 \leq \delta_{.95}] = P[D_1 \leq \delta_{.95}]P[D_2 \leq \delta_{.95}] \\ = (.95)(.95) = (.95)^2$$

The difference,

$$P[D_1 \leq \delta_{.95} \text{ and } D_2 \leq \delta_{.95}] - (.95)^2$$

is a measure of association (dependence) from position to adjacent position. Note that if:

$$I(D_1 \leq \delta_{.95}) = \begin{cases} 1 & \text{if } D_1 \leq \delta_{.95} \\ 0 & \text{if } D_1 > \delta_{.95} \end{cases} \\ I(D_2 \leq \delta_{.95}) = \begin{cases} 1 & \text{if } D_2 \leq \delta_{.95} \\ 0 & \text{if } D_2 > \delta_{.95} \end{cases}$$

then the covariance is:

$$C(1) = \text{Cov}[I(D_1 \leq \delta_{.95}), I(D_2 \leq \delta_{.95})] = P[D_1 \leq \delta_{.95} \text{ and } D_2 \leq \delta_{.95}] - (.95)^2$$

The same covariance is assumed for:

$$I(D_2 \leq \delta_{.95}) \text{ and } I(D_3 \leq \delta_{.95}) \dots I(D_7 \leq \delta_{.95}) \text{ and } I(D_8 \leq \delta_{.95})$$

There are about  $7n/8$  such pairs among the whole set of  $n$  observed differences.

Let  $d_{(s)}$  be the sample 95<sup>th</sup> percentile where  $s$  is the smallest integer not less than  $n(.95)$ .  
When  $n$  is large:

$$\hat{C}(1) = \frac{\text{number of pairs, } (D_i, D_{i+1}), \text{ where both are } \leq d_{(s)}}{\text{total number of pairs } (D_i, D_{i+1})} - (.95)^2$$

is a good estimate of  $C(1)$ . Similarly, for the approximately  $6n/8$  pairs  $(D_i, D_{i+2})$ :

$$C(2) = \text{Cov}[I(D_1 \leq \delta_{.95}), I(D_3 \leq \delta_{.95})]$$

is estimated by:

$$\hat{C}(2) = \frac{\text{number of pairs, } (D_i, D_{i+2}), \text{ where both are } \leq d_{(s)}}{\text{total number of pairs } (D_i, D_{i+2})} - (.95)^2$$

and:

$$\hat{C}(k) = \frac{\text{number of pairs, } (D_i, D_{i+k}), \text{ where both are } \leq d_{(s)}}{\text{total number of pairs } (D_i, D_{i+k})} - (.95)^2$$

The proof that  $d_{(s)}$  is asymptotically normal may be modified in order to account for the dependence among adjacent differences. It is still true that:

$$(A1) \quad \begin{aligned} P[d_{(s)} \leq x] &= 1 - P[d_{(s)} > x] = 1 - P[s - 1 \text{ or fewer } D_i \leq x] \\ &= 1 - P[T(x) < s] \end{aligned}$$

$$\text{where } T(x) = \sum_{i=1}^n I(D_i \leq x) = \text{number of differences } D_i \leq x$$

Moreover,  $T(x) - nF(x)$ , has a mean of 0 and, for large samples, is approximately normal under a wide range of dependence structures. Consequently, the sums:

$$\sum_{i=1}^8 I(D_i \leq x)$$

are independent of one another and each has the same distribution. Since  $T(x)$  is just the sum of these group sums, the central limit theorem gives:

$$\frac{T(x) - nF(x)}{\text{s.d.}[T(x)]} \text{ as approximately standard normal.}$$

Consequently, from (A1) and the normal approximation:

$$\begin{aligned} P[\sqrt{n}(d_{(s)} - \delta_{.95}) \leq z] &= P[d_{(s)} \leq (\delta_{.95} + n^{-1/2}z)] \\ &= 1 - P[T(\delta_{.95} + n^{-1/2}z) < s] \\ &= 1 - \Phi \left[ \frac{s - nF(\delta_{.95} + n^{-1/2}z)}{\text{s.d.}[T(\delta_{.95} + n^{-1/2}z)]} \right] \end{aligned}$$

Now, note that:

$$\begin{aligned} \frac{1}{\sqrt{n}}(s - nF(\delta_{.95} + n^{-1/2}z)) &= \frac{1}{\sqrt{n}}(s - nF(\delta_{.95}) - n f(\delta_{.95})n^{-1/2}z + 0(1)) \\ (A2) \quad &= \frac{1}{\sqrt{n}}(s - n(.95) - n^{-1/2}z f(\delta_{.95})) + 0(1) \\ &= -z f(\delta_{.95}) + 0(1) \end{aligned}$$

Furthermore,

$$\frac{1}{n} \text{Var} \left[ T(\delta_{.95} + n^{-1/2} z) \right] = \text{Var} \left[ I \left( D_1 \leq \delta_{.95} + n^{-1/2} z \right) \right] + \sum_{k=1}^7 \frac{2(8-k)}{8} \text{Cov} \left[ I \left( D_1 \leq \delta_{.95} + n^{-1/2} z \right), I \left( D_{1+k} \leq \delta_{.95} + n^{-1/2} z \right) \right]$$

which converges to:

$$\begin{aligned} F(\delta_{.95}) - F^2(\delta_{.95}) + \sum_{k=1}^7 \frac{2(8-k)}{8} \{ P[D_1 \leq \delta_{.95}, D_{1+k} \leq \delta_{.95}] - (.95)^2 \} \\ = (.95)(.05) + \sum_{k=1}^7 \frac{2(8-k)}{8} C(k) = \lim_{n \rightarrow \infty} \frac{1}{n} \text{Var} [T(\delta_{.95})] \end{aligned}$$

Therefore, by (A2),

$$P \left[ \sqrt{n} (d_{(s)} - \delta_{.95}) \leq z \right] \approx 1 - \Phi \left[ \frac{-z f(\delta_{.95})}{\frac{1}{\sqrt{n}} \text{s.d.} [T(\delta_{.95})]} \right]$$

or  $\sqrt{n} (d_{(s)} - \delta_{.95})$  is approximately normal with a mean of 0 and a variance of:

$$\frac{1}{n} \left[ \frac{(.95)(.05) + \sum_{k=1}^7 \frac{2(8-k)}{8} C(k)}{f^2(\delta_{.95})} \right]$$

As has been indicated above, the  $C(k)$  may be estimated by  $\hat{C}(k)$  and the large sample normality will still hold. Therefore using Table A.1 to obtain  $K_c$  and noting that:

$$\sigma_{Q_{95}} = \sqrt{\text{Var} Q_{95}}$$

It is 95% certain that  $Q_{95}$  lies in the interval:

$$Q_{95} \leq Q_{95} + K_c \sigma_{Q_{95}}$$

therefore it is safe to say that we are 95% confident that:

$$Q_{95} \leq (Q_{95} + K_c \sigma_{Q_{95}}) \sigma_{mc}$$

## APPENDIX B Computer Code Summary Description

<u>Computer Code</u>	<u>Description</u>
CASMO-4	<p>CASMO-4<sup>7,8</sup> is a multigroup two-dimensional transport theory code for depletion and branch calculations for a single assembly. It calculates the cross sections, nuclide concentrations, pin power distributions and other nuclear data used to calculate input to the SIMULATE-3 program. Some of the characteristics of CASMO-4 are:</p> <ol style="list-style-type: none"><li>1. 40 energy group cross section library.</li><li>2. 7 energy groups are used during the two-dimensional transport calculations.</li><li>3. Gadolinium and other burnable absorbers are depleted microscopically.</li><li>4. The predictor-corrector approach is used for depletion.</li><li>5. Effective resonance cross sections are calculated individually for each pin.</li></ol>
ESCORE	<p>ESCORE<sup>12,13,14,15</sup> is a steady-state fuel performance code capable of modeling the thermal and mechanical response of light water reactor fuel and is used to provide fuel temperature inputs to CASMO-4 and SIMULATE-3.</p>
PRP	<p>PRP is an NSP developed code that compares the predicted incore detector reaction rates from SIMULATE-3 with the measured reaction rates from the plant flux map traces.</p>
SIMULATE-3	<p>SIMULATE-3<sup>9,10</sup> is a two-group 3-dimensional nodal program based on the QPANDA neutronics model. Some of the features of SIMULATE-3 are:</p> <ol style="list-style-type: none"><li>1. Explicit reflector cross-section model.</li><li>2. Pin power reconstruction.</li><li>3. Fourth order expansion of intranodal flux distribution.</li><li>4. No input normalization is necessary from higher order calculations or benchmark results.</li></ol>
SPO	<p>SPO is an NSP developed code that generates statistics, according to the methods of Appendix A, for the measured versus predicted reaction rate comparisons as output by the PRP code.</p>
TABLES-3	<p>TABLES-3<sup>11</sup> processes CASMO-4 output files and generates tables of nuclear data by fuel type for input to SIMULATE-3.</p>